APPLICATION OF SMALL BASELINE SUBSET (SBAS) TIME-SERIES ANALYSIS FOR LANDSLIDE DETECTION IN HAWAI‘I

A THESIS SUBMITTED TO THE GRADUATE DIVISION OF THE UNIVERSITY OF HAWAI‘I AT MĀNOA IN PARTIAL FULFILLMENT OF THE REQUIREMENTS FOR THE DEGREE OF

MASTER OF SCIENCE

IN

CIVIL ENGINEERING

AUGUST 2022

By

Ryan Hendrix

Thesis Committee:

Phillip Ooi, Chairperson
Scott Rowland
Adrian Ricardo Archilla

Keywords: InSAR; remote sensing; small baseline subsets (SBAS); surface displacement; line-of-sight; 2D decomposition; landslides; and rockfalls

COPYRIGHT

Copyright in this work is held by the author. Please ensure that any reproduction or re-use is done in accordance with the relevant national copyright legislation.

DEDICATION

Dedicated to Masa Fujioka who introduced me to geotechnical engineering. You were a true friend and a thoughtful mentor. I will remember you always.

ACKNOWLEGEMENTS

I would like to express my sincere gratitude to my thesis committee chair Dr. Phillip Ooi; my committee members Dr. Adrian Richardo Archilla and Dr. Scott Rowland; Brandon Hee from the Hawaiʻi Department of Transportation; Nick Machairas my colleague and friend; JoDee Taylor my guide; Sue and Sid Inouye and Shyun Ueno for your friendship; my parents Cheryl and Gary Hendrix; and my dear love and the metal of my heart Lil.

ABSTRACT

The occurrence of landslides or rockfalls onto public roadways can result in a wide variety of issues for commuters and government agencies affiliated with the roadway systems. Under the best circumstances, landslide or rockfall debris on a roadway will cause commuter delays and result in minimal costs associated with remedial efforts. Under worst case circumstances, these occurrences can result in property and roadway infrastructure damage, injury, and even loss of life. The Hawaiʻi Department of Transportation (HDOT) is proactively attempting to identify areas near public roadways that may pose potential concern for landslide or rockfall activity. As part of these efforts, they have requested research be conducted involving the use of satellite synthetic aperture radar (SAR) imagery to conduct interferometry (InSAR) for two locations: Hawaiʻi Route 19 between mileposts 10 and 30; and Hawaiʻi Route 360 between mileposts 0 and 35. The Small Baseline Subset (SBAS) InSAR approach was determined to be the best method for the areas of HDOT interest. An extensive search of SAR imagery for the Hawaiian Islands proved that only limited datasets are publicly available for the areas of interest. To provide a proof of concept for implementation of SBAS analysis in the Hawaiian Islands, a case study of the Waiʻōmaʻo landslide located in Pālolo Valley on the Island of Oʻahu was conducted to compare available inclinometer data with SBAS datasets. Two-dimensional decomposition was implemented for opposite orbits of descending and ascending Sentinel-1 datasets. Decomposition was conducted to compare and review with *in situ* Waiʻōmaʻo landslide inclinometer data. Overall, the case study results show that when both ascending and descending datasets are used to derive displacements that are resolved in the direction of movement, InSAR analysis can effectively capture inclinometer trends in areas experiencing relatively small displacements over time (< 30 mm/year) but the accuracy diminished in fast moving slides (≥ 270 mm/year). Following the case study, the SBAS method was then applied to the Hawaiʻi Island and Maui study areas. Application of the InSAR technique was limited by the following: SAR data availability; geographic positioning and radar shadowing; and amount of vegetation in the research areas. The Hawaiʻi Island study area displacements were decomposed in a direction perpendicular to the slope contours to estimate the true displacements. Review of two-dimensional decomposition results was conducted for the potential of landslides and rockfalls in Hawaiʻi Island. Of the areas, minimal displacements were measured. Obtaining SBAS descending and ascending opposite orbits for Maui proved unsuccessful due to radar

shadowing caused by Haleakalā shield volcano. SBAS processing was only successful for the descending orbit for Maui.

TABLE OF CONTENTS

LIST OF TABLES

LIST OF FIGURES

1. INTRODUCTION

Interferometric Synthetic Aperture Radar (InSAR) was first introduced as a method for landslide detection in 1991 when it was used in a landslide case study in the southern French Alps (Massonnet and Feigl, 1998). Since that time, InSAR has grown as a method of remote sensing for landslides and ground surface deformation detection. Small Baseline Subset (SBAS) analysis was first developed by Berardino et al. (2002) as a method for surface deformation monitoring in natural terrain. From the time of development, variations of the SBAS algorithm have been used to detect landslides with SAR imagery around the world. An example of the use of InSAR for landslide detection is the mapping service, InSAR Norway. It was developed in a partnership between the Geological Survey of Norway, Norwegian Water Resource and Energy Directorate, and Norwegian Space center to track ground surface movements for the entire country of Norway.

Rockslides and landslides commonly occur in the Hawaiian Islands. When these events take place in undeveloped areas, they can impact the ecosystem but are not of concern for human health and safety. When they occur along a public thoroughfare, they pose a danger to the public, and can result in loss of lives and cause significant damage to infrastructure. Following rockfall and landslides, repair of the infrastructure can result in traffic congestion and commuting delays, sometimes for several months. As an example, landslides on February 18 and 19, 2019 near the Pali highway tunnels on the island of Oʻahu resulted in public injury and highway closure for approximately nine months following the event (DOT 2019). The estimated total cost for emergency repairs amounted to approximately $22 million, and Phase 1 improvements amounted to approximately $64 million (DOT 2019). The Hawaiʻi Department of Transportation (HDOT) is concerned with landslide and rockfall susceptibility along the Hāmākua coast (Route 19) on the island of Hawaiʻi and along Hāna Highway (Route 360) on the island of Maui.

1.1. *Objectives*

The objectives of this research include:

1. Conduct a literature review on InSAR;
2. Research accessibility to SAR images from all satellites;
3. Download and process SAR images for a site on Oʻahu with inclinometer data and compare horizontal displacements from InSAR with those from inclinometer data;
4. Download and process SAR images for Hāmākua coast (Route 19) on the island of Hawaiʻi and along Hāna Highway (Route 360) on the island of Maui and compute horizontal movements at these locations if possible.

1.2. *Report Organization*

The basic principles associated with radar, SAR, and interferometry are discussed in Chapter 2. SAR satellite systems and dataset availability are outlined in Chapter 3. A literature review that outlines the evolution of the use of SBAS for detection of landslides and ground surface deformation is then presented in Chapter 4. Chapter 5 presents the study locations, topography, rainfall and geology whereas the project methodology and datasets are introduced in Chapter 6. Chapter 7 covers SBAS analysis conducted for a case study of a known landslide occurring within the Pālolo Valley subdivision on Oʻahu. The Pālolo Valley landslide was chosen for the case study because there are inclinometer data available for the location that date to 1999 to serve as ground-truth. SBAS techniques to detect ground surface changes in the study locations on Hawaiʻi and on Maui are presented in Chapter 8. A discussion of results is provided in Chapter 9. A summary and conclusions followed by suggestions for future research are contained in Chapter 10.

2. REVIEW OF THE RADAR PRINCIPLE, SAR AND INSAR, AND SBAS

2.1. *Review of Radar Principles*

Radio Detection and Ranging or 'radar' was developed during World War II as a technology for "air defense and over the-horizon surveillance" (Meyer 2019). Radar is a method of using radio waves to locate objects in 3D space. Radar systems can be used in all weather conditions and can be acquired day or night (Meyer 2019). Radar is typically defined as electromagnetic waves with wavelengths between 1 centimeter and 10 meters (Meyer n.d.). Electromagnetic waves of this size are not absorbed by the atmosphere in what is known as "an atmospheric window" (NOAA 2022).The concept of "atmospheric opacity" is where the atmosphere blocks electromagnetic waves of certain wavelengths whereas "atmospheric transparency" allows the remaining electromagnetic waves through (Meyer n.d.). Gamma rays, x-rays, and ultraviolet light with short wavelengths (0.01 nm to 100 nm) are all blocked by the atmosphere (Meyer 2019). Long-wavelength radio waves (10 m to 1 km) are also blocked by the atmosphere (Meyer 2019). Conversely, wavelengths in the infrared spectrum (100 μm to 1 cm) are absorbed by atmospheric gases (Meyer 2019). Also, both visible light (400 nm to 700 nm) and radio waves used in SAR exist in the atmospheric window (Meyer 2019).

At the most basic, the radar principle is the transmission and reception of an electromagnetic pulse. When a transmitter emits an electromagnetic pulse to an object over a range (R), the object scatters the radar pulse and some of the signal returns to the radar system where it is acquired by a receiver. The travel time from transmission to reception is given by the following equation (1)

$$t = 2 \cdot \frac{R}{C} \qquad (1)$$

where t is travel time, R is the range, and C is the speed of light.

The distance or range, R, between the radar system and a target can be measured (Meyer 2019). Radar systems also measure the amount of backscatter energy received from each radar pulse (Meyer 2019). Backscatter energy is essentially the amount of radar signal returned to the system from each pulse.

Radar wavelengths used for satellite remote sensing are shown in table 1 below.

Table 1 Radar wavelengths use in SAR remote sensing (Meyer 2019)

Band	Frequency (GHz)	Wavelength (cm)	Application
X	8-12	2.4-3.8	Urban monitoring
C	4-8	3.8-7.5	Global mapping and change detection
S	2-4	7.5-15	Not currently applied in SAR remote sensing of earth
L	1-2	15-30	Geophysical, biomass and vegetation mapping
P	0.3-1	30-100	Not currently applied in SAR remote sensing of earth

Other radar bands (Ka, K, and Ku) have applications in airport surveillance and satellite altimetry but are generally not used in SAR (Meyer 2019).

Radar systems abord satellites acquire images as the satellite travels along a heading. The radar pulses are transmitted and received from “side-looking” systems that acquire images from an off-nadir incidence angle along a radar line-of-sight also known as the range direction. The radar signal scatters off the ground surface and some of it returns to the receiver. The area of radar signal illumination on the ground is known as the footprint. Figure 1 shows the general geometry of the system.

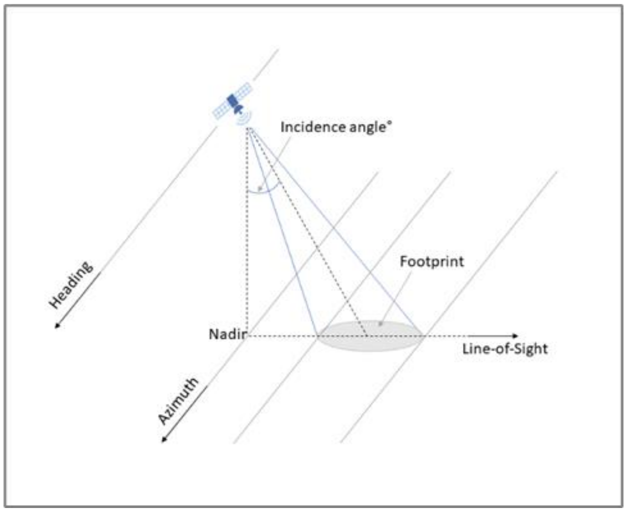

Figure 1 Incidence angle of radar image acquisition (after Meyer n.d.).

Figure 2 shows how the Sentinel-1 radar system captures images of an area from an ascending look direction of approximately 79° and a descending look direction of approximately 280°.

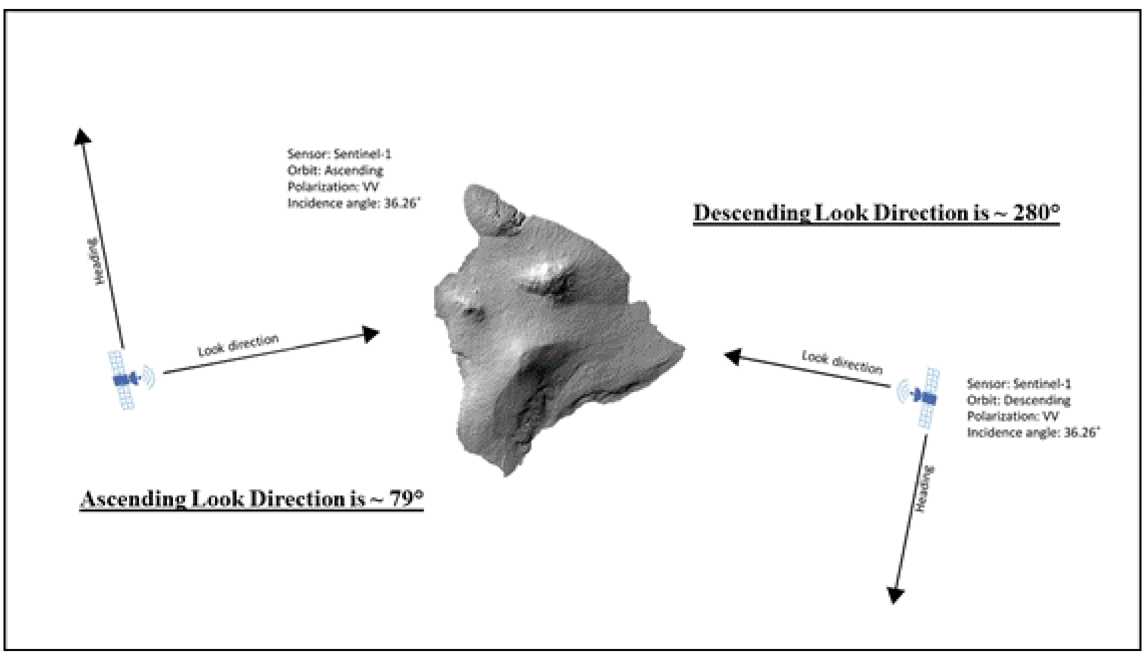

Figure 2 Ascending and descending LOS of Sentinel-1 radar acquisition

2.2. *Synthetic Aperture Radar*

As shown in Figure 2, SAR systems capture radar images using side-looking radar transmitters/receivers (Meyer 2019). The satellites travel along a heading at some distance above the ground. The point on the ground directly below the system's track is known as nadir (Meyer 2019). The along-track direction of the satellite is the azimuth (Meyer 2019). The radar system transmits pulses of pulse length (τp) that scatter off the earth's surface over an area referred to as the footprint (Meyer 2019). The size (S) of the antenna footprint is defined by the radar wavelength (λ), the antenna length (L), and the range (R) between the system and the ground in Equation 2. Note that pulses are transmitted radar signals and scatters are received radar signals. Both the transmitted pulse and receiving scatter are of a known radar wavelength (λ).

$$S \approx \frac{\lambda}{L} \cdot R \qquad (2)$$

In equation 2, S is a one-dimensional measurement. To obtain an antenna footprint that is two-dimensional, the signals received must be grouped by their arrival time in both the range and azimuth directions (Meyer 2019). Signal returns arrive at different times depending on whether the return is from the near or far ends of the footprint, known as near-range and far-range, respectively (Meyer 2019). "Objects at different ranges can be distinguished if their range separation is larger than half the transmitted pulse length" (Meyer 2019).

Originally, radar systems were developed as airplane-mounted systems or "side looking aerial systems" (SLAR). They capture radar imagery with acceptable azimuth and range resolutions acquired using a moderately sized (1 to 2 meter) radar antenna. This is because the systems could be flown relatively close to the ground (< 3000 meters). The range resolution for SLAR systems is defined by Equation 3.

$$\rho_R = \frac{C \cdot \tau_p}{2} \qquad (3)$$

where C is the speed of light and τ_p = pulse length (Meyer 2019). The ground range resolution for radar images (ρ_G) is defined by Equation 4.

$$\rho_G = \frac{\rho_R}{\sin(\theta_i)} \qquad (4)$$

where θ_i is the local incidence angle and ρ_R is the range resolution shown in Equation 3 (Meyer 2019). Calculating the ground range resolution is important because it allows remote sensing practitioners the ability to discern objects within a single radar image on the ground (Meyer 2019).

The azimuth resolution is defined by Equation 5.

$$\rho_{Az} = S_{Az} \approx \frac{\lambda}{L_{AZ}} \cdot R \qquad (5)$$

where S_{AZ} is the length in the azimuth direction, L_{AZ} is the side length of the antenna, and λ is the radar wavelength (Meyer 2019). The azimuth resolution that could be achieved with SLAR systems was acceptable because the systems could be flown relatively close to the ground. For space-borne systems, the azimuth resolution linearly degrades as the distance from the ground increases (Meyer 2019). To overcome this problem, satellite systems would need significantly large antennas to create a larger aperture. The antenna would need to be 100s of meters long, which is impractical. The problem with azimuth resolution was solved by Carl Wiley in 1952 (Meyer 2019). Wiley determined that a single point on the ground can be observed in multiple radar images acquired along its track. By viewing a point on the ground in multiple images, a longer antenna aperture can be synthesized, hence the term Synthetic Aperture Radar. Note that aperture synthesis is conducted in post processing, not during image acquisition.

2.3. *Interferometric Synthetic Aperture Radar (InSAR)*

Interferometric synthetic aperture radar (InSAR) is accomplished by measuring the phase difference between two SAR images from the same area at every pixel (Meyer n.d.). The SAR images are co-registered with each other. The phase concept is presented below.

During radar transmission, a radar signal will travel X-number of full wavelengths and a partial wavelength before reaching the earth's surface (Figure 3).

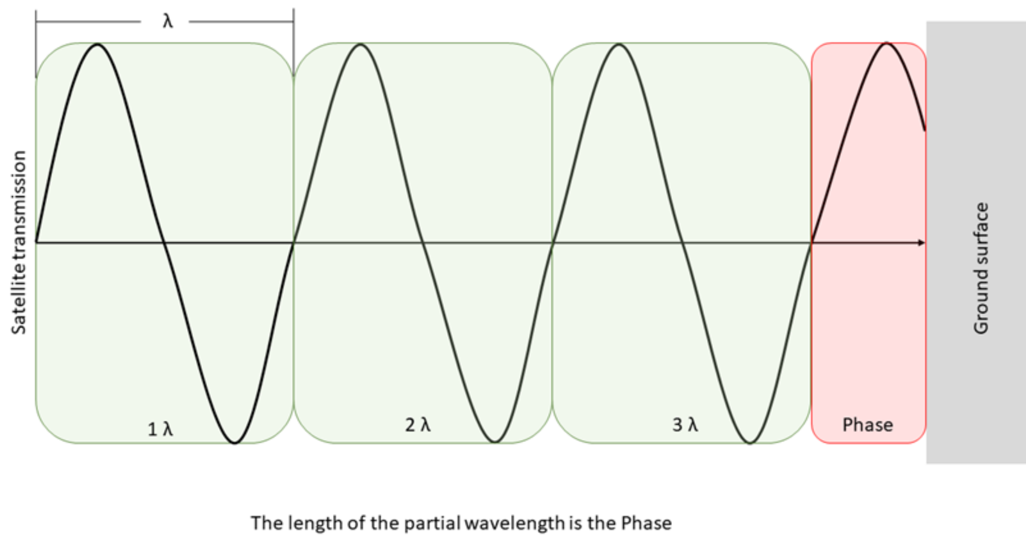

Figure 3 Illustration of radar phase (after Meyer n.d.)

The length of the partial wavelength is known as the phase. However, in reality, the phase consists of a deterministic component ($\Psi(R)$), which is the portion of the signal that is wanted, but also a scatter component (Ψ_{scatt}) as shown in Equation 6. The deterministic component is the true portion of the phase whereas the scatter component is the error resulting from combining the phase measurements of different random scatters that are received by the pixel of interest. Ψ_{scatt} will make up a different portion of the phase signal for each pixel in a SAR image (Meyer n.d.).

$$\Psi = \Psi(R) + \Psi_{scatt} \qquad (6)$$

Figure 4 shows the geometric elements considered for interferometry. Images 1 and 2 are collected by back-scattered energy collected at antennas 1 and 2, which are separated in space by a distance (B). For any pixel, there is a range R from the ground in Image 1 and a range R + ΔR from the ground in Image 2. θ is the incidence angle of Image 1. h is the elevation of the ground surface above the reference surface, which is usually mean sea level (msl). The calculation for the phase (φ) measurement determined in an interferogram is presented below in (Equations 7 to 9)

$$\Psi_1 = -\Psi(R) + \Psi_{scatt1} \qquad (7)$$

$$\Psi_2 = -\Psi(R + \Delta R) + \Psi_{scatt2} \qquad (8)$$

$$\Phi = \Psi_1 - \Psi_2 \qquad (9)$$

If images 1 and 2 are acquired at or near the same time by two SAR systems traveling along parallel tracks (tandem systems), the topographic height can be determined from the SAR phase as shown in Equation 10 (Meyer n.d.).

$$\emptyset_{topo} = \frac{4\pi}{\lambda} \cdot \frac{B_{\perp}}{R\sin\theta} h \qquad (10)$$

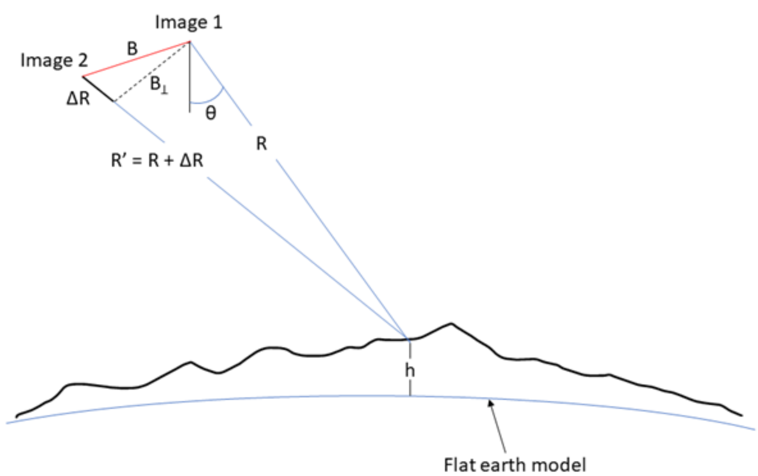

Figure 4 Geometry of InSAR (after Meyer n.d.)

Equation 10 is the basis for deriving Digital Elevation Models (DEMs) from SAR imagery.

Figure 5 illustrates the concept of differential InSAR (D-InSAR) for measuring the displacement that has occurred between two SAR image acquisition dates. ΔR is the measurement of displacement in the direction of the satellite line-of-sight and incidence angle, otherwise known as the look direction (Meyer n.d.). Calculations for determining displacement from D-InSAR are presented in (Equations 11 and 12).

$$\emptyset = \emptyset_{\text{topo}}(\text{Z}; \text{B}) + \emptyset_{\text{def}} \qquad (11)$$

$$\emptyset_{\text{def}} = \frac{4\pi}{\lambda} \cdot \Delta\text{R}_{\text{def}} \qquad (12)$$

where Z = h ± amount of ground deformation

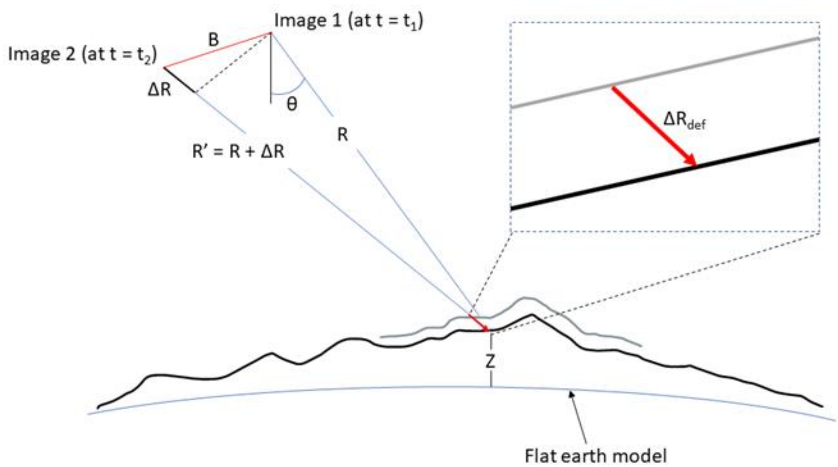

Figure 5 Measuring displacement with D-InSAR (after Meyer n.d.)

Interferograms will generally have coherent pixels and non-coherent pixels. Where "coherence is the complex correlation between two complex SAR images and consists of a phase and a magnetude component" (Hamid et. al., 2021). The magnetude is a value between 0 and 1. Interferogram pixels with a coherence of 0 have no coherence and represent pixels with high phase noise. Interferogram pixels with a coherence of 1 have perfect coherence and represent pixels with no phase noise. When evaluating measurements from an interferogram, it is important to consider the coherence for the area of measurement. The coherence serves as an indication of the amount of phase noise within an image.

2.4. *Small Baseline Subsets (SBAS)*

This section provides a general overview of the Small Baseline Subset (SBAS) method, which is a method that uses distributed targets to measure surface deformation over time. The method uses several radar scatterers that contribute to the signal within a single pixel of a radar image (Meyer n.d.). Each pixel represents a certain ground size area dependent on the radar system. In the SBAS process, distributed targets are used to provide high point density per pixel within an image (Meyer n.d.). See figure 6. This also results in high noise levels as opposed to other methods such as the Point Target method. The distributed target method is useful for large areas and applicable for conducting analysis of natural terrain such as detecting slow moving landslides (Meyer n.d.). Figure 6 illustrates multiple distributed point scatterers within a single radar image pixel. For Sentinel-1, each pixel represents a 5 meter by 20 meter area on the ground. The backscattered energy from all scatterers in the 5 meter by 20 meter area make up the overall signal in that pixel.

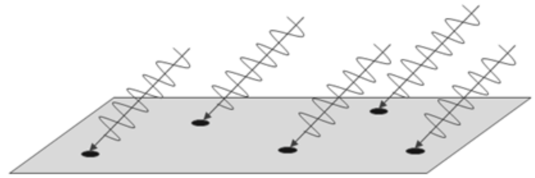

Figure 6 Distributed targets for SBAS (after Meyer n.d.).

The SBAS method was developed to study ground surface change over time. Traditional differential interferometry or D-InSAR uses only two images to measure the change in ground surface between two different times. The traditional D-InSAR method is most sucessful in collecting measurements for an event that has already occured. An example of the use of D-InSAR would be measurments collected before and after an earthquake to determine the amount of coseismic displacement. The time of the event must be known to facilitate image selection to capture the measurements. Time-series analyses can be conducted to study events that occur over an extended period. In fact, time-series analysis involves the processing of multiple images and the more images processed, the greater the precision in the measurement of ground deformation (Meyer n.d.).

SBAS requires organization of an interferometric stack, which is a collection of SAR images acquired from the same area over time. The interferometric stack consists of images of the same area and from the same direction of satellite heading (either all descending or all ascending). At least 20 to 30 images are required for successful implementation of the algorithm. The images are georeferenced and “stacked” chronologically. Several points within the interferometric stack are then selected in areas that are known to be stable in each image. These “tie points” are generally selected in locations of rock outcrops or manmade structures that are known to have not changed location during the time covered by the images. Theoretically, the tie points should have a total phase difference of zero. The interferometric stack allows for more precise isolation of the "displacement-related phase component (φ_{def}) from the observed interferometric phase (φ)" (Meyer n.d.). The observed interferometric phase φ is composed of displacement (φ_{def}), atmosphere (φ_{atmo}), topography (φ_{topo}), and noise (φ_{noise}) components (Meyer n.d.). Isolation of φ_{def} is possible because the phase components have "temporal, spatial, and baseline dependencies" (Meyer n.d.). Equation 13 represents the components that make up the observed φ

$$\Phi = \varphi_{def} + \varphi_{topo} + \varphi_{atmo} + \varphi_{noise} \qquad (13)$$

To isolate the deformation phase component, it is important to understand the characteristics of each portion of the signal. Φ_{topo} is proportional to the spatial baseline. Φ_{atmo} is random in time but smooth in space, i.e., it occurs at consistent elevations above the ground surface. Φ_{noise} is random in both time and space. (Meyer n.d.). Portions of the observed interferometric phase signal matching the above characteristics are deleted, leaving only the displacement portion (φ_{def}) that is typically smooth in time. Isolation of the displacement portion is accomplished by creation of a design matrix that filters the observed interferometric phase.

Each pixel within an interferometric stack will have an observed unwrapped phase vector. Assume that a site has N SAR images (time steps) and assume that combining pairs of these N SAR images result in M number of interferograms. Therefore, the observed interferometric phase will be M-dimensional as demonstrated in Equation 14.

$$\varphi = [\varphi_{1,2}, \ldots, \varphi_{M-1,M}] \qquad (14)$$

An N-dimensional vector is needed to determine the phase at each time step as demonstrated in Equation 15.

$$\Psi = [\Psi_1, \ldots, \Psi_N] \qquad (15)$$

The phase (Ψ) is "proportional to the path length at each time step and consists of surface position/displacement as well as topography, atmosphere, and noise components. The N-dimensional vector is achieved by inverting a design matrix A and multiplying by the observed unwrapped phase vector (φ) as presented in equations 16 and 17.

$$\varphi = A\Psi \qquad (16)$$

$$\Psi = A^{-1}\varphi \qquad (17)$$

where A is a design matrix that reveals the phase contribution to each interferogram (Meyer 2021). This concept is represented below in Figure 7.

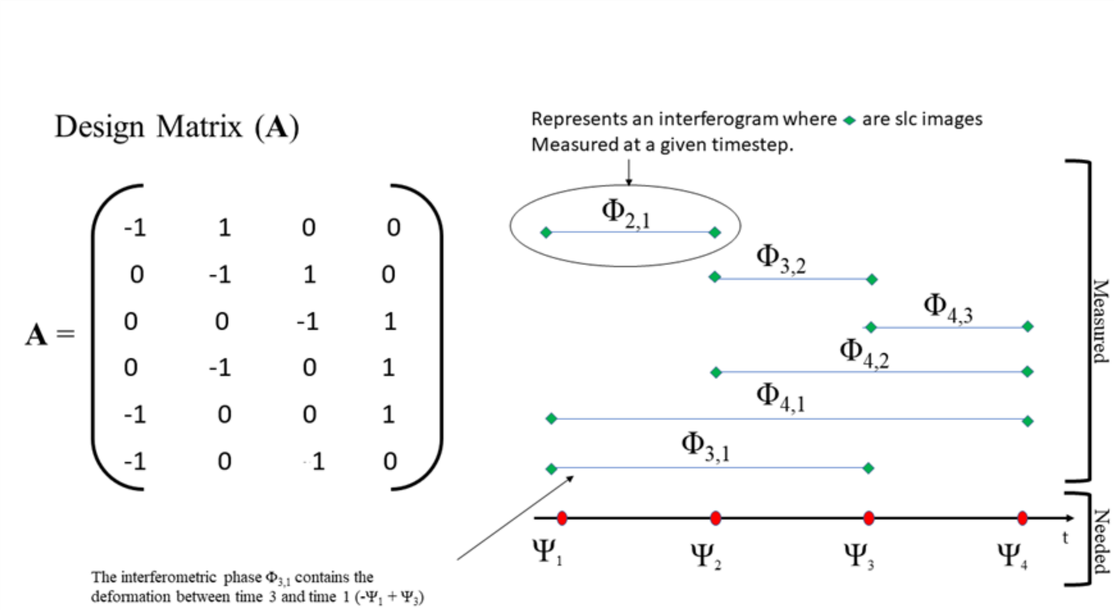

Figure 7 Example design matrix for the SBAS algorithm (after Meyer 2021).

In the example above, each row of the design matrix (A) represents an interferometric pair of SAR images. The example consists of four (4) time steps, represented by each column in a row. The values in the first row represent an interferogram where the SAR image from timestep 1 is subtracted from the SAR image from timestep 2. In the second row, the SAR image from timestep 2 is subtracted from the SAR image from timestep 3, etc. (Meyer 2021).

Filtering of topography, atmosphere, and noise from the observed unwrapped phase vector is accomplished through the process of inversion of the design matrix A. This process implements the singular value decomposition (SVD) method to obtain a least squares solution. For this method to be applied correctly, the displacements measured must occur at a rate that is smooth in time, i.e.; at a generally consistent rate. This requirement partially explains why the SBAS method is not applicable for rapid landslide movements and catastrophic landslide failures. For areas that experience catastrophic failure, there will be a total loss of coherence, resulting in the deletion of the pixel within the area of failure.

3. SENSORS AND AVAILABLE DATASETS WITH INSAR APPLICATIONS

The SAR missions shown in Table 2 represent past, present, and future missions that can be used for InSAR. Extensive effort to acquire SAR images from each satellite was attempted for this report, but several missions do not have data available to the public. Table 2 presents the name of the satellite, lifetime of the SAR sensor, wavelength of radar, any known dataset issues, spatial resolution of the data (m per pixel), and accessibility to the images. Additionally, columns four (4) through six (6) provide an indication of the number of images available for each sensor in the report study areas. As an example, no images from Seasat are available for any of the report study areas, whereas abundant images are available for the report study areas for Sentinel-1.

Many of the satellite datasets are either commercial or have limited availability. Much of this unavailability is due to sensor deployment for foreign defense purposes. Cost quotes for commercial datasets were requested from several Distributed Active Archive Centers (DAACs), but proved uneconomical for this study (> $2,000.00 per image). Requests for Radarsat-1 imagery were granted by the Canadian Space Agency and several hundred raw SAR images were acquired for the project sites; however, significant data gaps were present in the Radarsat-1 images that prevented image focusing into "single-looks", better known as single-look-complex (SLC) images. The most abundant and publicly available dataset for the project areas was from the Sentinel-1 system. Images were downloaded from the Alaska Satellite Facility's ASF Vertex online DAAC (ASF DAAC 2021). Limited data for ALOS-1 PALSAR-1 were also acquired from ASF Vertex (ASF DAAC 2021). No other notable datasets were acquired for the project sites.

Table 2 SAR sensors and sensor information

Satellite	Lifetime	Wavelength	# of Images O‘ahu	# of Images Hawai‘i	# of Images Maui	Known Dataset Issues	Resolution	Access type
Seasat	1978	L-band λ = 24.6 cm	No images	No images	No images		Az: 25m Rg: 25 m	Public
ERS-1	1991-2001	C-band λ = 5.6 cm	No images	No images	No images		Az: 6-30 m Rg: 26 m	Limited public access
JERS-1	1995-1998	L-band λ = 24.6 cm	No images	Limited images	No images		Az: 18 m Rg: 18 m	Limited public access
ERS-2	1995-2011	C-band λ = 5.6 cm	No images	No images	No images		Az: 6 – 30 m Rg: 26 m	Limited public access
ENVISAT	2002-2012	C-band λ = 5.6 cm	No images	No images	No images		Az: 28 m Rg: 28 m	Limited public access
ALOS-1 PALSAR-1	2006-2011	L-band λ = 24.6 cm	Limited images	Limited images	Limited images		FBS: 10 x10 m FBD: 20 x10 m PLR: 30 x10 m ScanSAR: 100 m	Public
Radarsat-1	1995-2013	C-band λ = 5.6 cm	Large image collection	Largei mage collection	Largei mage collection	Temporal data gaps	Standard: 25 x 28 m Fine: 9 x 9 m Wide1: 35 x 28 m Wide2: 35 x 28 m ScanSAR: 50 x 50 – 100 x 100 m	To 2008: limited 2008-2013: Commercial
TerraSAR-X, TanDEM-X	2007- 2010-	X-band λ = 3.5 cm	Large image collection	Large image collection	Large image collection		Spotlight: 0.2x1.0 - 1.7 x 3.5 m Stripmap: 3x3 m ScanSAR: 18 – 40 m	Limited/commercial
Radarsat-2	2007-	C-band λ = 5.6 cm	Unknown	Unknown	Unknown		Spotlight: ~ 1.5 m Stripmap: ~ 3 x 3 -25 x 25 m ScanSAR: 35 x 35 - 100 x 100 m	Commercial

COSMO-SkyMed	2007-	X-band λ = 3.5 cm	Un-known	Un-known	Un-known		Spotlight: ⩽1 m Stripmap: 3 – 15 m ScanSAR: 30 – 100 m	Limited/commercial
ALOS-2, PALSAR-2	2014-	L-band λ = 24.6 cm	Limited images	Limited images	Limited images		Spotlight: 1 x 3 m Stripmap: 3 – 10 m ScanSAR: 25 – 100 m	Limited/commercial
Sentinel-1	2014-	C-band λ = 5.6 cm	Large image collect-ion	Large image collect-ion	Large image collect-ion		Stripmap: 5 x 5 m; (IW): 5 x 20 m (EW): 20 – 40 m	Public
SAOCOM	2018-	L-band λ = 24.6 cm	Un-known	Un-known	Un-known		Stripmap: 10 x 10 m TopSAR:100 x 100 m	To be determined
PAZ SAR	2018-	X-band λ = 3.5 cm	Un-known	Un-known	Un-known		Spotlight: 0.2 x 1.0 - 1.7 x 3.5 m Stripmap: 3 x 3m ScanSAR: 18 – 40 m	Commercial
RCM	2019-	C-band λ = 5.6 cm	Un-known	Un-known	Un-known		Very high, medium, low-res modes (3-100 m)	To be determined
NISAR	2023-	L-band λ = 24.6 cm	N/A	N/A	N/A		3 – 20 m (mode dependent)	Public
BIOMASS	2022-	P-band λ = 70 cm	N/A	N/A	N/A		⩽ 60 x 50 m	Public
TanDEM-L	2023-	L-band λ = 24.6 cm	N/A	N/A	N/A		12 x 12 m	Public

Figure 8 presents the past and present X-, C-, and L-band sensors that are used for SAR analysis. Future SAR missions are not shown in the figure.

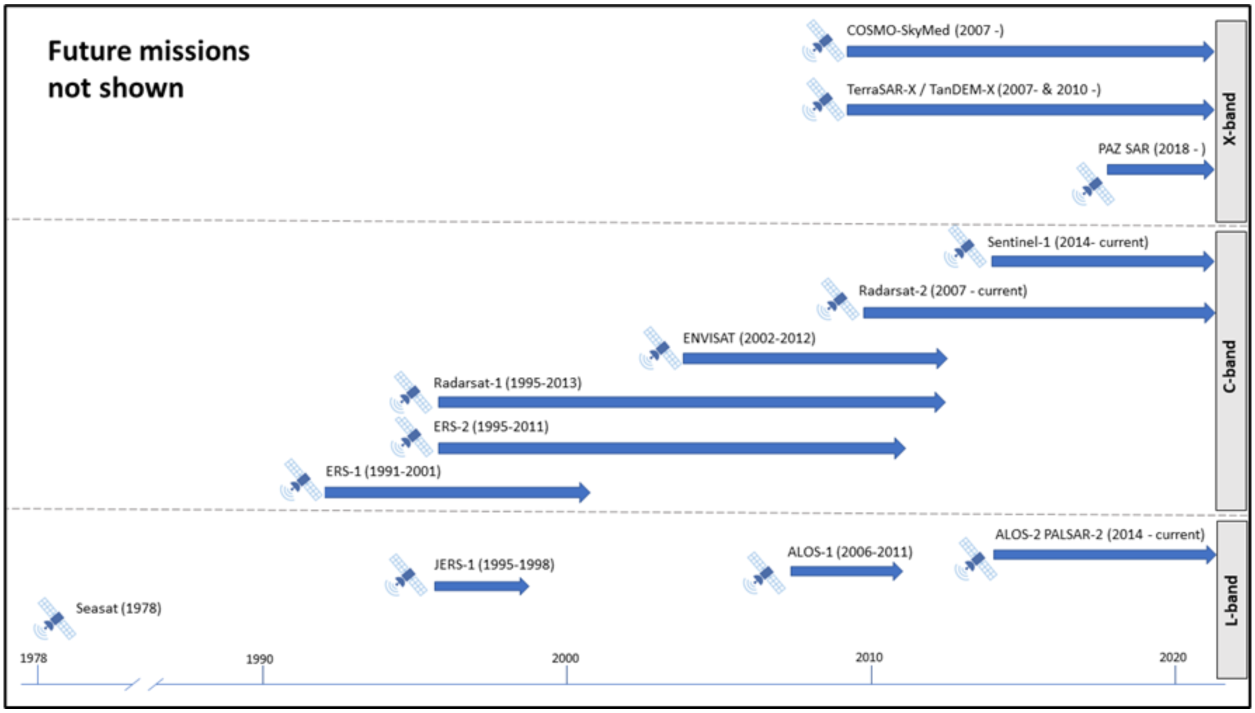

Figure 8 Past and present SAR satellites (after UC Berkeley 2022)

4. LITERATURE REVIEW

The literature review focuses on the general evolution of the SBAS algorithm and sub methods. Development of SBAS occurred over the past 20 years. SBAS was developed to collect displacement measurements over time periods of months to years (over large temporal baselines). D-InSAR methods using only 2 SAR images cannot produce accurate displacement measurements when the images are separated by a significant amount of time (i.e. years) because areas tend to change over time and coherence of images separated by large timeframes is essentially non-existent; this concept is described as temporal decorrelation. The literature review highlights the development and refinement of the SBAS method to allow for precise measurements of ground surface changes.

4.1. *Berardino et. al., 2002*

In 2002, Berardino et. al. (2002), published *A new Algorithm for Surface Deformation Monitoring Based on Small Baseline Differential SAR Interferograms* (Berardino et. al., 2002) that "presents a new differential synthetic aperture radar (SAR) interferometry algorithm for monitoring of temporal evolution of surface deformations" (Berardino. et al., 2002). The authors discussed the issues associated with D-InSAR and introduced the limitations of the "point Target" or Persistent Scatter" method that were known at the time of publication. The authors showed limited effectiveness due to image decorrelation over time (Berardino et. al., 2002). In other words, if two SAR image acquisitions are separated by a significant amount of time, there will be little to no coherence between images. Conducting D-InSAR for image pairs that have little pixel correlation will yield displacements that are not accurate. At the time of publication, the Persistent Scatter (PS) method had been developed and was the most widely accepted solution for collecting displacements over a long timeframe. Berardino et. al. (2002) noted that only "targets that exhibit sufficiently high coherence values" would be processed (Berardino et. al., 2002). Their method based on "small baseline differential SAR interferograms" was presented as a solution to increase point density to conduct analysis in natural terrains. The SBAS algorithm incorporates the design matrix and SVD approach presented in Section 2.4. The authors also presented methods to remove topographic and atmospheric artifacts from the phase signal. To demonstrate the effectiveness of the algorithm, the authors conducted analysis using 44 ERS-1 acquisitions collected between 1992 and 2000. The study site was the active caldera of Campi Flegrei near the City of Naples in Southern Italy that was inflating and deflating. The authors compared the displacements obtained from the algorithm with those from GPS data to show that they had achieved centimeter scale accuracy in displacements (Berardino et. al., 2002).

4.2. *Manzo et. al., 2006*

Manzo et. al. (2006) published their research on a volcanically active island in the Gulf of Napoli, Italy in a paper entitled *Surface deformation analysis in the Ischia Island (Italy) based on spaceborne radar interferometry* where they used SBAS techniques to characterize ground subsidence occurring on the island. Using ERS-1 satellite data between 1992 and 2003, Manzo et. al. (2006) obtained 58 acquisitions each from the ascending and descending tracks resulting in 133 and 148 interferograms for the ascending and descending tracks, respectively. Once SBAS was completed for both descending and ascending orbits, the authors conducted two-dimensional decomposition using the combined datasets "to discriminate the vertical and east–west components of displacements" (Manzo et. al., 2006). To obtain east-west displacement vector components, the authors calculated the descending line-of-sight displacement minus the ascending line-of-sight displacement divided by two and then divided by the sine of the incidence angle of image acquisition for each pixel. The mean incidence angle was 23° (Manzo et. al., 2006). For vertical component calculations, the mathematics are the same except the division is conducted using the cosine of 23° (Manzo et. al., 2006). Validation of the results was conducted by comparing with both GPS and spirit leveling network data. The "maximum value of the root mean square difference" between GPS and decomposition measurements was determined to be approximately 1 mm/yr (Manzo et. al., 2006). This method for 2D decomposition is used in chapters 7 and 8 of this report for analyses conducted for O'ahu and Hawai'i Island.

4.3. ***Tong and Schmidt, 2016***

Tong and Schmidt (2016) published *Active movement of the Cascade landslide complex in Washington from a coherence-based InSAR* time series method in which they used 24 ALOS-1 PALSAR-1 scenes to conduct SBAS analysis along the Columbia River Gorge. The scenes between 2007 and 2011 were used to develop a coherence-based small-baseline subset (SBAS) that improved on the conventional SBAS methodology by incorporating a concept of weighted coherence (Tong and Schmidt, 2016). Instead of deleting interferogram pixels that had low coherence, the authors kept all pixels in the interferograms by including mathematical considerations for phase coherence during the inversion processing step. A weight of the observed phase data was included "based on the coherence for each pixel in each differential interferogram using" a weighting matrix rather than the more traditional design matrix to accurately measure landslide movements of the Red Bluff Landslide that is part of the Cascade Landslide Complex (Tong and Schmidt, 2016). The modified SBAS algorithm used was able to show that the Red Bluff Landslide is seasonally activated with periods of acceleration in winter and spring months (Tong and Schmidt, 2016). The SBAS observations compared favorably with GPS point data from landslide monitoring efforts (Tong and Schmidt, 2016). Additionally, the authors compared SBAS displacement trends with average monthly rainfall data and were able to correlate periods of heavy rainfall with accelerated movements measured in the SBAS time-series displacement plots (Tong and Schmidt, 2016).

4.4. *Fuhrmann and Garthwaite, 2016*

Fuhrmann and Garthwaite (2016) published *Resolving Three-Dimensional Surface Motion with InSAR: Constraints from Multi-Geometry Data Fusion* where they compared Envisat data from 2006 to 2010 with multi-geometry data fusion, which involves use of satellite data in both ascending and descending paths and computing the East and vertical components of movement and then resolving the displacements in the direction of interest. The authors simulated deformation using a Mogi Model to compare the line-of-sight deformation estimates with estimates from multi-geometry data fusion. The authors were motivated by the fact that often InSAR studies were conducted using line-of-sight measurements only, and interpretations of line-of-sight displacement measurements were presented as the true ground displacements. Fuhrmann and Garthwaite (2016) showed that use of line-of-sight measurements to evaluate field deformations without considering both ascending and descending components can lead to significant errors.

The authors also noted that due to the inherent satellite orbital patterns, north-south displacement estimates are generally poorly constrained and are therefore, much more difficult to accurately estimate (Fuhrmann and Garthwaite 2016). Consequently, landslides can be poorly characterized when deformations are occurring primarily in the north-south direction while landslide deformations in an east-west direction can be effectively captured by multi-geometry data fusion.

4.5. *Cigna and Tapete, 2021*

Cigna and Tapete (2021) published their work entitled *Sentinel-1 Big Data Processing with P-SBAS InSAR in the Geohazards Exploitation Platform: An Experiment on Coastal Land Subsidence and Landslides in Italy*. In their publication the authors implemented an advanced time-series analysis (called Parallel Small Baseline Subset or P-SBAS) to detect landslides and to characterize a coastal area known as Capo Colonna located in southern Italy. The researchers implemented P-SBAS for large interferometric stacks of Sentinel-1 datasets composed of ascending and descending images acquired between 2014 and 2020. The ascending and descending datasets consisted of 296 and 283 images, respectively (Cigna and Tapete, 2021). Using the Geohazards Exploitation Platform (GEP), the authors conducted temporally sequenced parallel analysis on both the ascending and descending datasets. They describe their approach as "Multi-temporal InSAR processing" with use of "the parallelized implementation of the SBAS differential InSAR" (Cigna and Tapete, 2021). The authors were able to capture high SBAS point density with a notably high temporal coherence threshold of 0.85 (Cigna and Tapete, 2021). Additional processing of the descending and ascending datasets was conducted through decomposition to determine vertical and east-west deformation field estimations which allowed the authors to characterize the direction and magnitude of movement for localized landslides. Decomposition was possible due to there being high point density as well as overlap of the descending and ascending datasets.

The study is representative of how "big data" processing can be used to enhance the capabilities of SBAS and InSAR analysis. This type of processing currently requires significant investment in digital infrastructure. However, as costs associated with the needed computational hardware are reduced over time, there will likely be more widespread access to large data parallel SBAS processing. With the ability to achieve high SBAS point density with coherence of 0.85 or higher, and by demonstrating accurate characterization of landslide movement, the authors showed that P-SBAS will likely become a go-to processing method for analysis of landslides and for landslide detection.

4.6. *Closing Remarks*

From its development in 2002, SBAS has developed to a point where it can be used to routinely obtain accurate and reliable ground surface measurements. Development of Parallelization P-SBAS allows for an increase in capability of the SBAS approach. Complex decomposition can (in some circumstances) be performed to allow for accurate interpretation of displacement characteristics, but the biggest takeaway is that both ascending and descending datasets are needed to accurately describe the behavior of complex ground surface changes.

5. STUDY LOCATIONS, TOPOGRAPHY, RAINFALL, GEOLOGY, SOILS

SBAS interferometry was conducted for three locations in the Hawaiian archipelago. A case study of Waiʻōmaʻo Landslide on the Island of Oʻahu was developed using Sentinel-1 ascending and descending datasets. Both ascending and descending data sets were able to capture the Oʻahu case study area because the topography was favorable to both lines-of-sight and unaffected by radar shadowing.

Analysis using Sentinel-1 descending and ascending data was also conducted for the area of interest on the islands of Hawaiʻi; however, radar shadow was a notable issue for the Hawaiʻi Island ascending dataset as a result of the Mauna Kea volcano blocking radar reception from the study area. Only a small portion of the study area was captured by the Hawaiʻi Island ascending dataset. Additionally, SBAS analysis using ALOS-1 PALSAR-1 descending data was conducted for Hawaiʻi Island.

For the Island of Maui, only descending data were used for the study location due to radar shadows caused by the Haleakalā volcano. Figure 9 shows the study locations for Oʻahu, Hawaiʻi Island, and Maui.

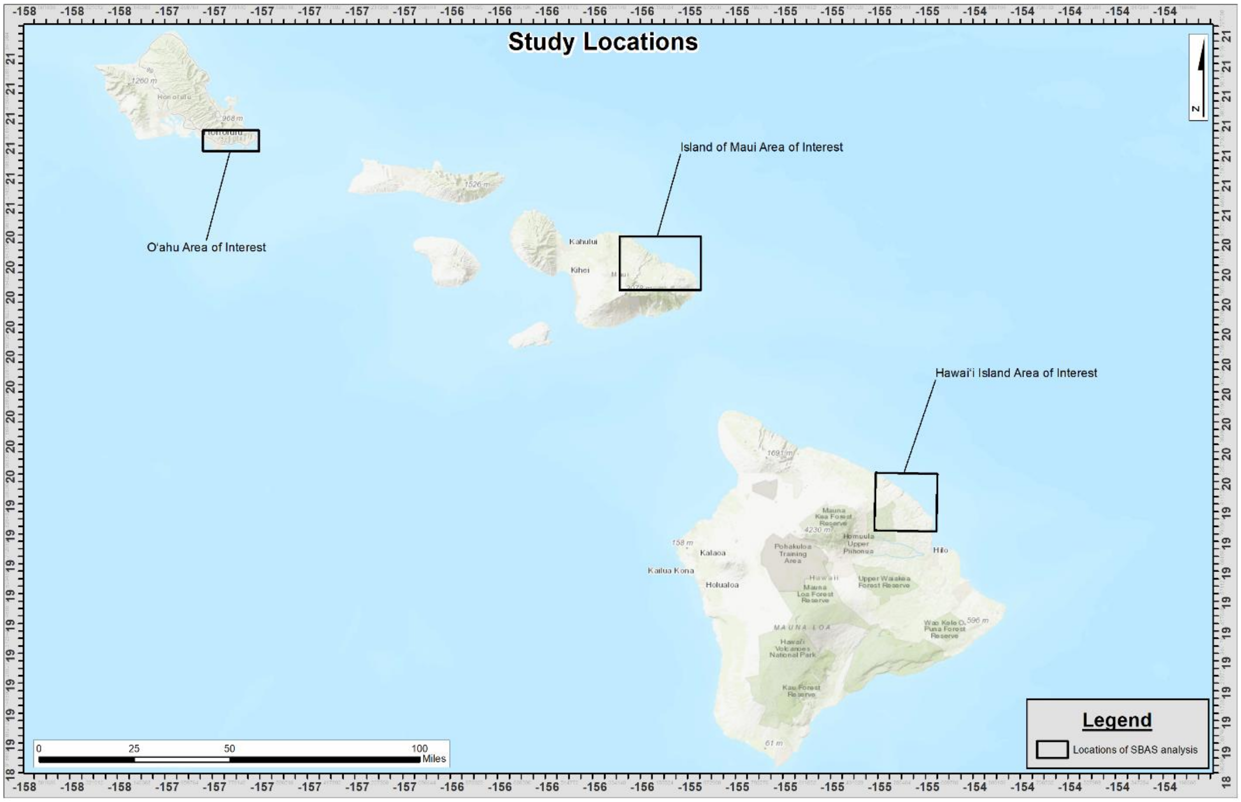

Figure 9 Study locations for O'ahu, Hawai'i Island, and Maui (after ESRI 2014)

5.1. *O'ahu (Case Study)*

5.1.1. O'ahu Study Location

The Wai'ōma'o landslide is located in Pālolo Valley on the eroded south flank of the Ko'olau volcano, which makes up approximately 2/3 of O'ahu. Historical and current studies have been conducted on portions of the landslide, which has been active for more than 60 years. The valley subdivision was constructed in 1952 and problems associated with landsliding were initially noted in 1954 (Peck, 1959). Figure 10 shows the general vicinity of the Wai'ōma'o landslide.

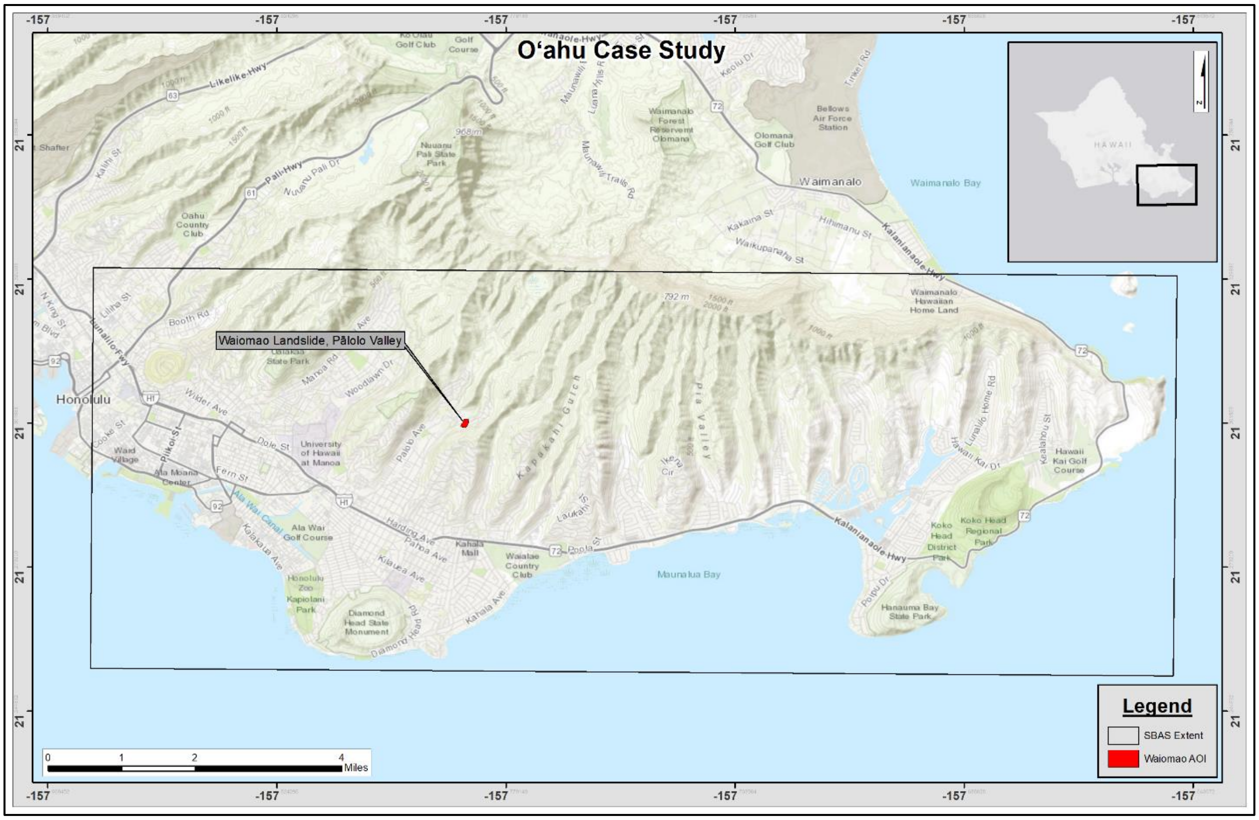

Figure 10 Vicinity Map for O‘ahu case study (after ESRI 2014)

There are several areas of movement within the general slide area. The areas of current activity are indicated in Figure 11 as “Area A”, “Area B”, “Wai‘ōma‘o Landslide”, and “Area C”. The area labeled “Wai‘ōma‘o Landslide” has been the subject of several studies. The “Wai‘ōma‘o Landslide” area is also included in publicly available geotechnical monitoring reports that have been prepared since 1999. The Wai‘ōma‘o Landslide term will be used in this report to remain consistent with how the area is labeled in past studies and the current monitoring reports.

Area A is near the lower intersection of Wai‘ōma‘o Road and Kuahea Street. Landslide activity there has resulted in demolition of several residential structures and sections of the Kuahea Place roadway and Kuahea Street. Google Earth imagery shows that demolition activities in the area started sometime in late 2018 (Google Earth 2018). Demolition and mitigation efforts for the area are currently underway between Kuahea Place and Waiʻōmaʻo Road. Site visits conducted in May 2022 revealed damage to Waiʻōmaʻo Road and existing residential structures in the general vicinity surrounding the area of demolition, with ground displacements possibly extending beyond the boundaries of mitigation efforts.

Area B is located to the north and downslope from Area A. The area is bound between Waiʻōmaʻo Road and Waiʻōmaʻo Stream. There are several residential structures in Area B that were constructed in the later part of 2013 (Google Earth 2013). Google Earth imagery from early 2013 show earthwork activities and installation of several retaining structures on the downslope portion of each residential structure (Google Earth 2013). It is unknown if the retaining structures include deep foundation elements.

Waiʻōmaʻo Landslide adjoins the Northeast boundary of Area B. Waiʻōmaʻo Road runs through the center of the slide and the upslope portion of the slide includes portions of Kuahea Street. The northeast boundary of the slide runs parallel to Lamaku Place and the downslope toe of the slide lies just above Kipona Place. Google Earth imagery show that the Waiʻōmaʻo landslide has been mostly undeveloped since image acquisition began in 2004 (Google Earth 2004).

Area C adjoins the Northeast portion of Waiʻōmaʻo Landslide. There are several residential structures within the area. Lamaku Place runs through the center of the area. Historical aerial images and a site visit (conducted in May 2022) do not indicate that demolition activities have occurred or are underway.

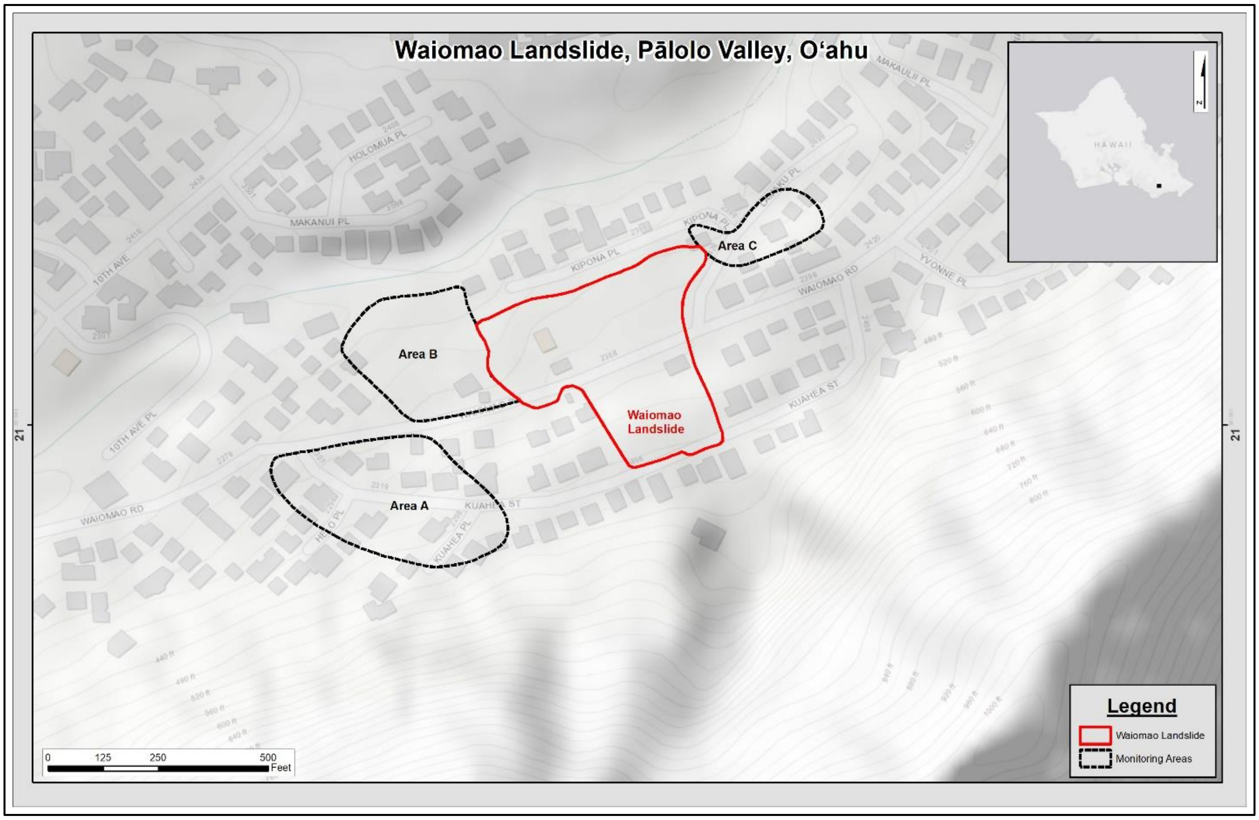

Figure 11 Areas of recent and historical landslide activity (after ESRI 2014)

5.1.2. Topography of the O‘ahu study area

The Wai`oma`o slide is located within the United States Geological Survey‘s 2017, 7.5-minute Topographic Map of the Honolulu Quadrangle (USGS 2017). The scale of the map is 1:24,000. Contours within the map are provided every 40 feet. Figure 12 shows selected elevation contours associated with the O‘ahu study area.

The contour lines shown in Figure 12 are from the 40 ft contours for Oahu Island GIS shapefile. The shapefile is available through the Hawaii Statewide GIS program at the online Geospatial data portal and is based on the 30-meter USGS Digital Elevation Model (DEM) (C&C of Honolulu 2021). Contours shown in Figure 12 are provided for visual representation. Detailed review of topography for the site was conducted using the 7.5-minute Topographic Map of the Honolulu Quadrangle (USGS 2017).

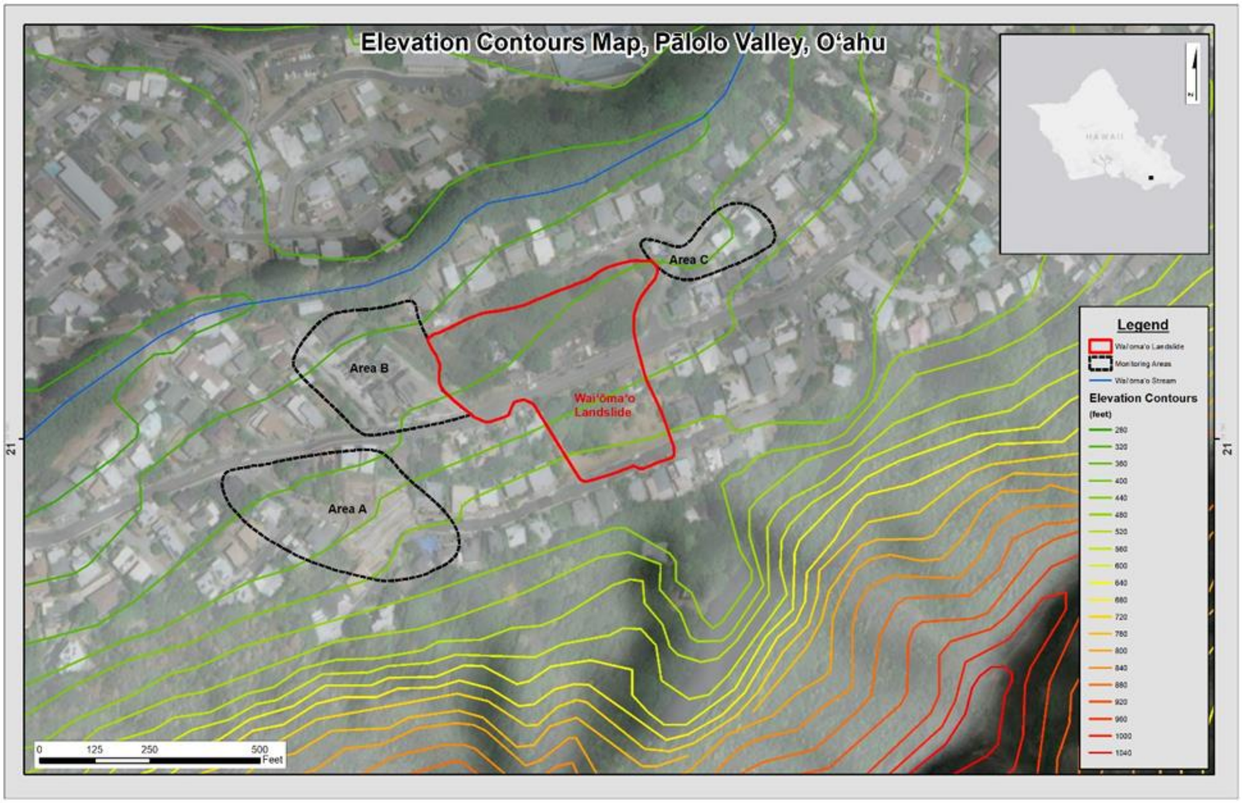

Figure 12 Pālolo Valley Elevation Contours (after C&C of Honolulu 2021

The general topography of the southeast valley wall, which includes the case study areas, generally slopes from 1,000 feet at the southeast ridge crest above Kuahea Place, to less than 300 feet at the stream bed of Wai‘ōma‘o Stream near 10th Avenue Place (USGS 2017).

The topography within Area A, generally slopes down from the southeast to northwest from approximately 480 feet above mean sea level (MSL) on the upslope portion above Kuahea Place, to approximately 340 feet on the downslope portion near Wai‘ōma‘o Road (USGS 2017). The topography within Area B slopes down from south to north from approximately 360 feet on the upslope portion along Waiʻōmaʻo Road to approximately 310 feet on the downslope portion near Waiʻōmaʻo Stream (USGS 2017). The topography of Waiʻōmaʻo Landslide generally slopes downward to the North-northwest from Kuahea Street at approximately 440 feet to approximately 325 feet near the Northwest corner of Kipona Place (USGS 2017). Topography within Area C slopes down from east to west from approximately 400 feet to 350 feet near Kipona Place (USGS 2017).

5.1.3. Annual rainfall of Oʻahu study area

Data for average annual rainfall of the Oʻahu study area are derived from the Rainfall Atlas of Hawaiʻi (http://rainfall.geography.hawaii.edu/interactivemap.html), a project of the Geography Department at the University of Hawaiʻi at Mānoa. The average annual rainfall for the area is approximately 65 inches per year (Giambelluca et al., 2013). Figure 13 shows selected isohyets for the Oʻahu study area.

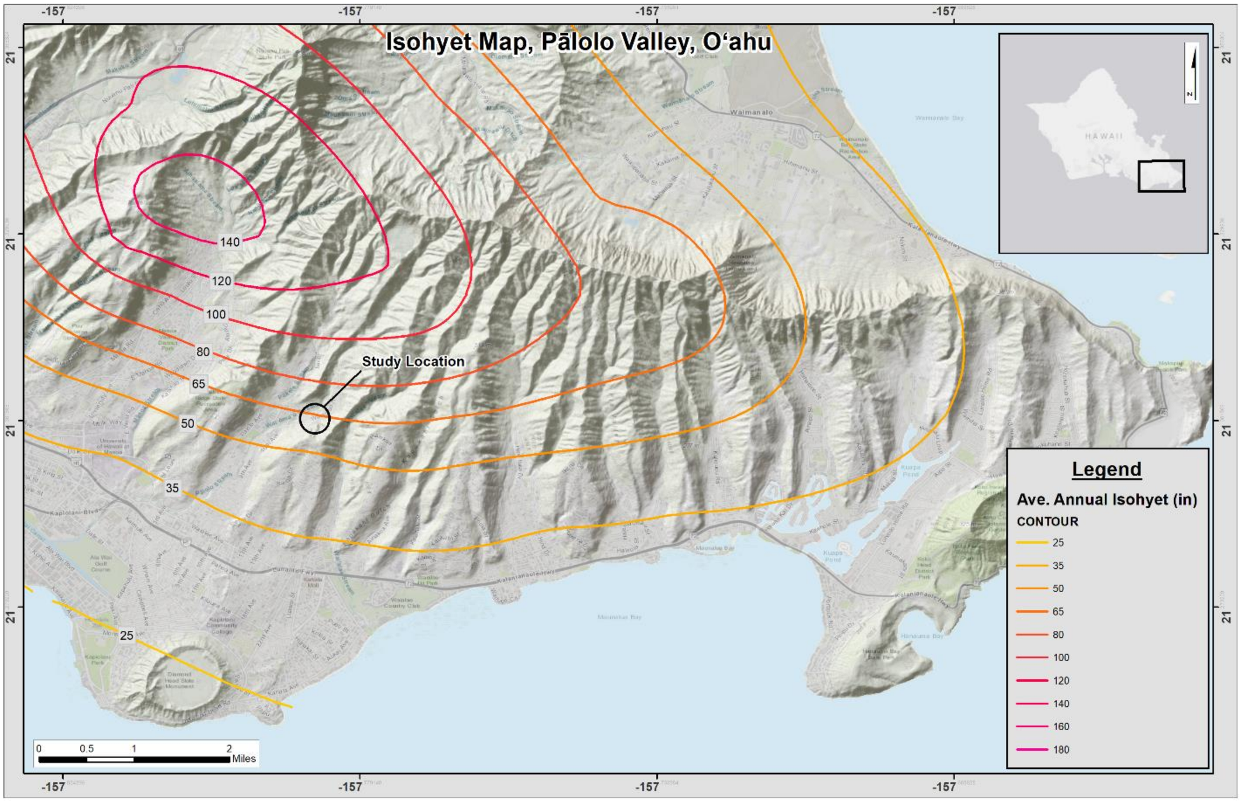

Figure 13 Isohyets Map, O‘ahu Southshore (after Giambelluca et al., 2013)

5.1.4. Geology of O‘ahu study area

The geologic units within the O‘ahu study area from the Geologic map of the State of Hawai‘i (Sherrod et al., 2021) comprise of Ko‘olau Basalt (QTkl) and Older Alluvium (QTko; Figure 14). A younger Alluvium unit (Qa) occurs immediately downslope, and along the NW boundary of Area B. The geologic units for the O‘ahu Study Area are shown in Figure 14 below.

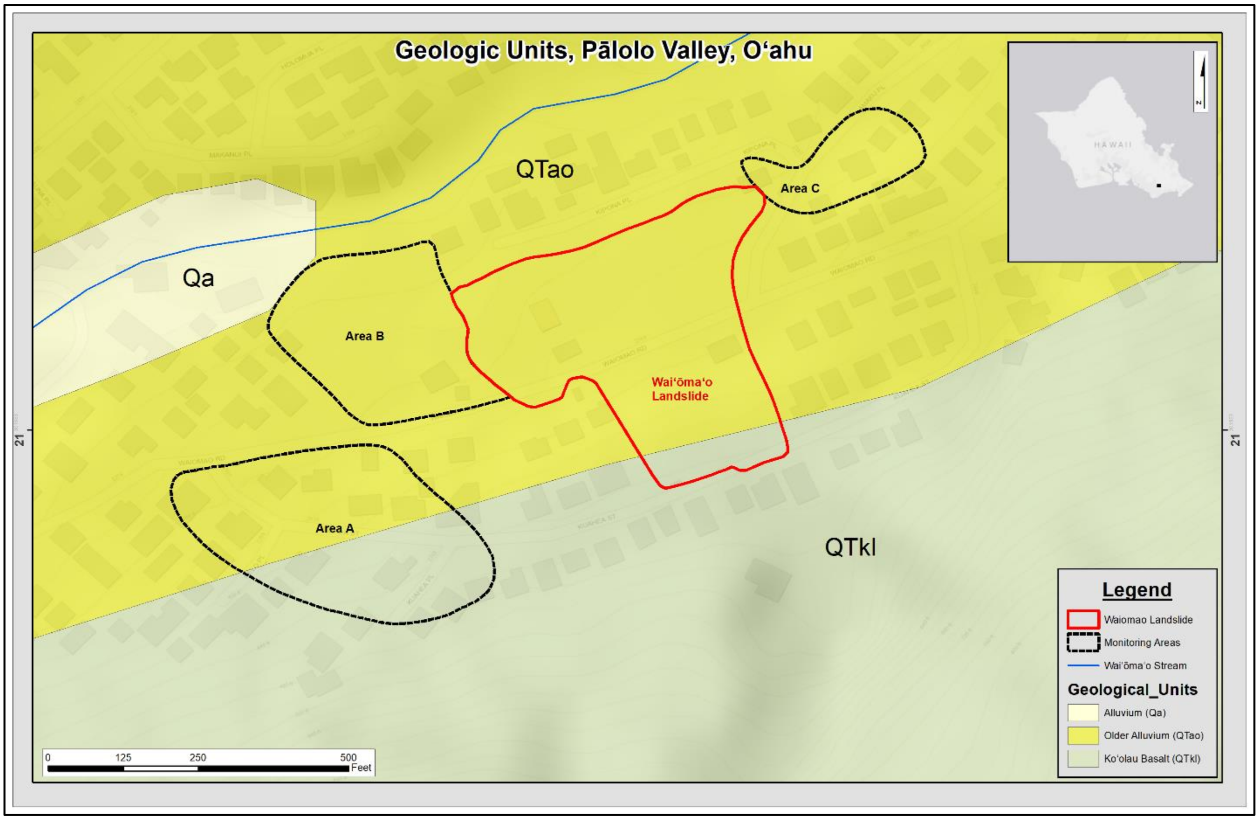

Figure 14 Geologic Units of O‘ahu Study Area (after C&C of Honolulu 2021)

The Ko‘olau Basalt (Pleistocene and Pliocene) is dated to between 1.8 and 3.0 million years (Ma) in age (Sherrod et al., 2021). The Ko‘olau Basalt is aphyric to pophyritic basalt and consists of both ‘a‘ā and Pāhoehoe lava flows (Sherrod et al., 2021).

The Older Alluvium (geologic symbol: QTao) consists of sedimentary deposits that are generally interpreted to be of the Pleistocene age. The unit primarily consists of consolidated sand and gravel (Sherrod et al., 2021).

The Alluvium (geologic symbol: Qa) consists of sedimentary deposits that are generally interpreted to be of Holocene and Pleistocene age. The unit primarily consists of “unconsolidated silts, sand, and gravel along streams and valley bottoms" (Sherrod et al., 2021).

5.1.5. Tabulated soils of the area of the O‘ahu case study

Table 3 provides a list of the 7 soils associated with the O‘ahu study area. The table is based on the Web Soils Survey produced by the National Cooperative Soil Survey (NCSS) and operated by the United States Department of Agriculture (USDA) Natural Resources Conservation Service (NRCS) (Web Soils Survey 2019). The table includes information for the mapped unit symbol, the map unit name, the number of acres of each soil type and the corresponding percent of the overall area of interest. Only soils within 0.25 miles of the site are shown in the table.

Table 3 Soils of the O‘ahu case study

Island of Oahu, Hawaii			
Map Unit Symbol	**Map Unit Name**	**Acres in AOI**	**Percent of AOI**
KaC	Kaena clay, 6 to 12 percent slopes	1.8	3.5%
KlaB	Kawaihapai stony clay loam, 2 to 6 percent slopes, MLRA 158	4.6	9.1%
LoD	Lolekaa silty clay, 15 to 25 percent slopes	9.8	19.5%
LoF	Lolekaa silty clay, 40 to 70 percent slopes	2.5	5.0%
LPE	Lualualei extremely cobbly clay, 3 to 35 percent slopes, MLRA 166	12.8	25.4%
LuA	Lualualei clay, 0 to 2 percent slopes, MLRA 163	0.5	1.0%
rRK	Rock land	18.3	36.5%
Total Area of Interest		50.3	100.0

5.2. *Hawai‘i Island*

The study area on Hawai’i Island is along Highway 19 between Mileposts 10 and 30. The highway generally runs parallel to the coastline along the north and northeast (i.e., windward) flanks of the Mauna Kea shield volcano. The areas of interest are along the upslope and downslope of the highway. This area has varying amounts of development, ranging from heavily vegetated natural terrain to agricultural lands to residential neighborhoods. The highway crosses numerous stream valleys. Figure 15 shows the location of the study area.

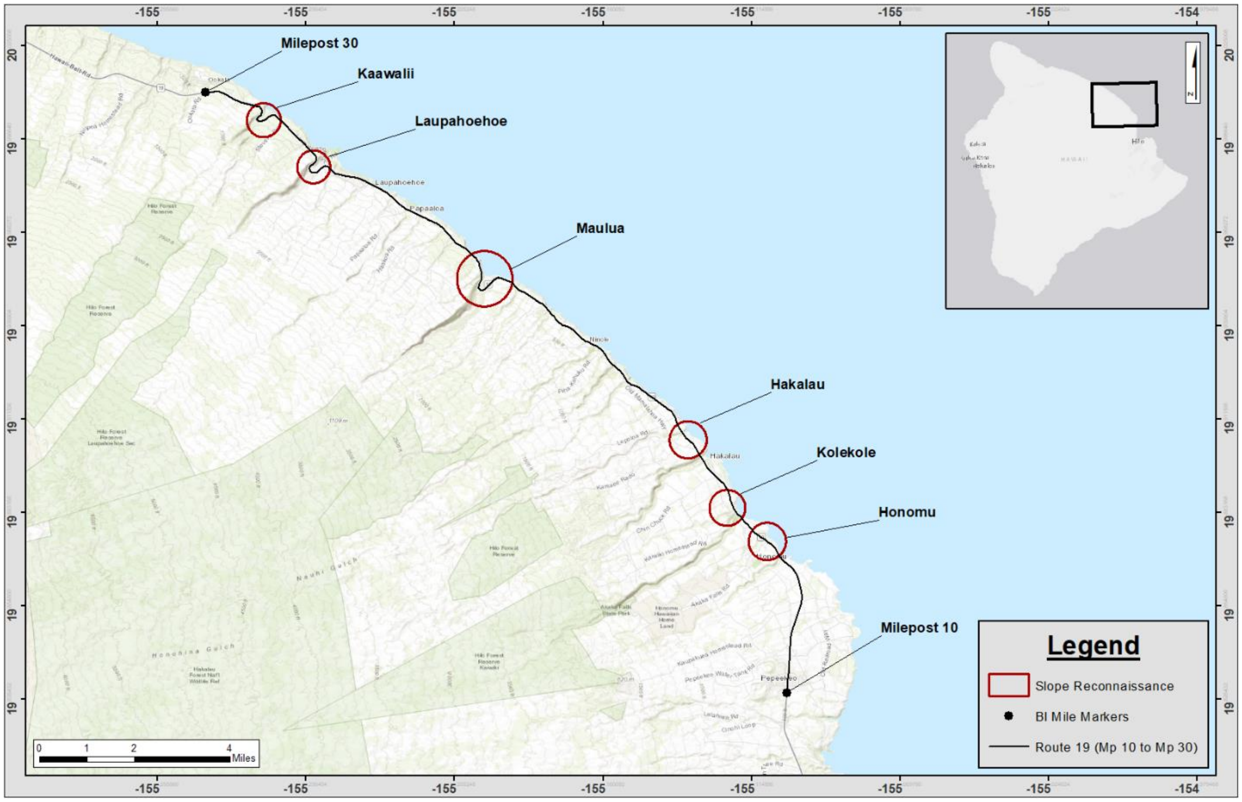

Figure 15 Map showing Hawai'i Island study location (after ESRI 2014)

There are several locations along the route that are known to have issues associated with landslides and rockfall (red circles in Figure 15). From Northwest to Southeast, they include Ka'awali'i, Laupāhoehoe, Maulua, Hakalau, Kolekole, and Honomū.

5.2.1. Topography of the Hawai'i Island Study Area

The Hawai'i Island study area topography is mapped in the United States Geological Survey's 2017, 7.5-minute Topographic Map of the Pāpa'aloa Quadrangle, Hawai'i (USGS 2017). The scale of the map is 1:24,000. Contours within the map are provided every 100 feet. Figure 15 shows elevation contours in the study area.

The contour lines in Figure 16 are from the 100 ft contours for Hawaii Island GIS shapefile, available through the Hawaii Statewide GIS program at the online Geospatial data portal and is based on the 30-meter USGS Digital Elevation Model (DEM) (C&C of Honolulu 2021). Detailed review of topography for the site was conducted using Figure 16. Note that contours greater than 1000 ft are shown for every thousand ft rather than 100 ft for the sake of brevity. Contours above 1,000 ft are generally beyond the interest of the Hawaiʻi Island study area.

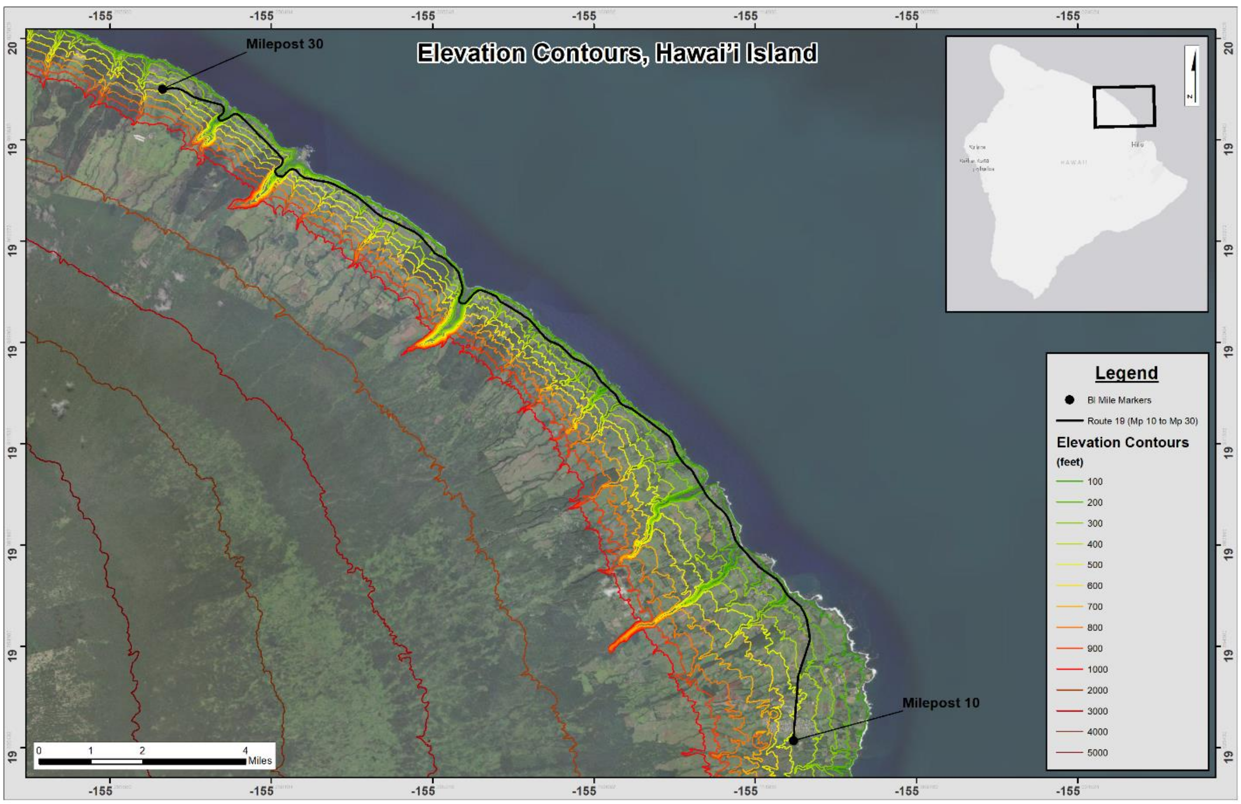

Figure 16 Hawaiʻi Island study area topography (after C&C of Honolulu 2021).

The highway elevations vary from approximately 150 feet to approximately 300 feet. The topography on either side of the highway varies significantly along the route. Slopes can be moderate to flat in agricultural and residential areas. Sections that pass through natural stream valleys can have slopes that approach 1H : 3V (1 horizontal to 3 vertical) (USGS 2017) and sections that are located in cuts can have much steeper slopes.

5.2.2. Annual rainfall of the Hawai‘i Island study area

The average annual rainfall for Route 19 on Hawai‘i Island in the Rainfall Atlas of Hawai‘i shows annual rainfall isohyet contours ranging from 100 inches per year to 160 inches per year (Giambelluca et al., 2013). Figure 17 shows the isohyets in the Hawai‘i Island study area.

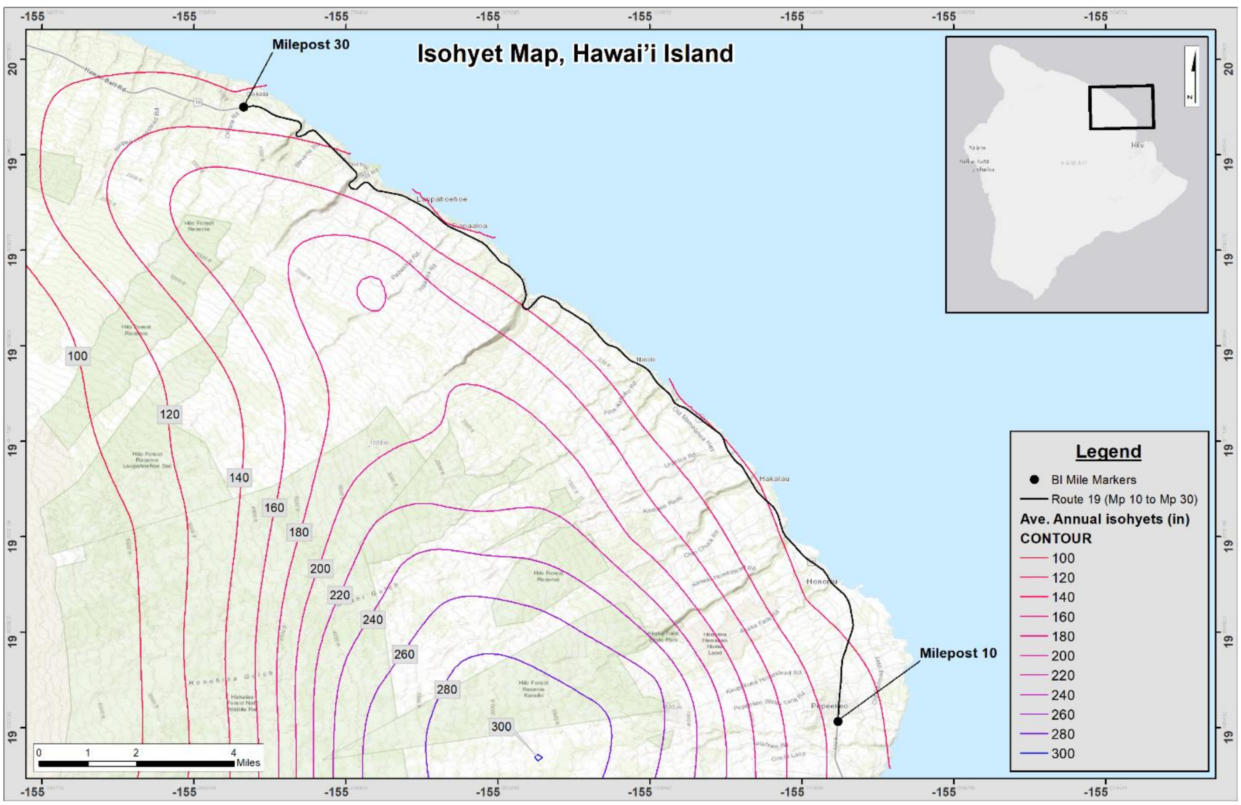

Figure 17 Isohyets Map, Hawai‘i Island (after Giambelluca et al., 2013)

5.2.3. Geology of the Hawai‘i Island study area

The geology along Route 19 is mapped in the Geologic map of the State of Hawai‘i as Hāmākua Volcanics and Laupāhoehoe Volcanics (Sherrod et al., 2021). Both volcanic units consist of geologic members that are from the Mauna Kea Shield Volcano. Figure 18 shows the geologic units associated with the Hawai‘i Island study area.

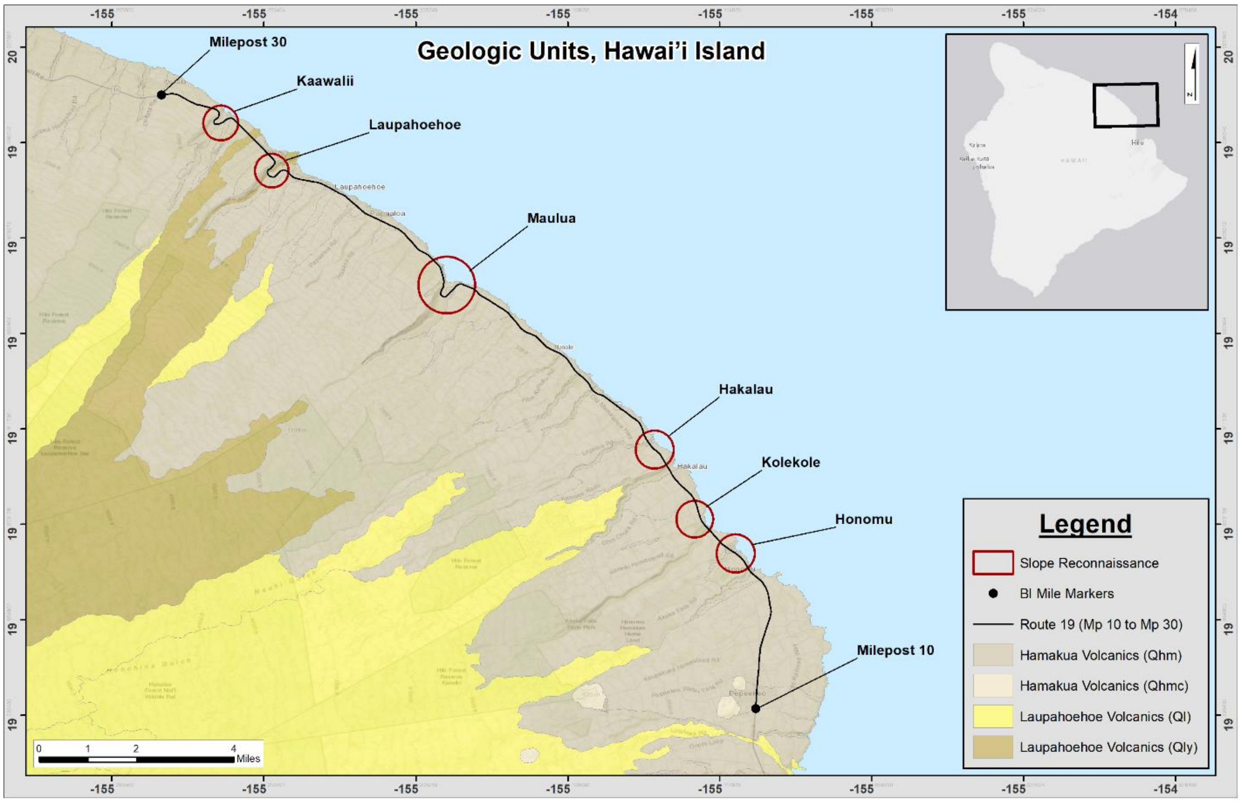

Figure 18 Geologic Units of Hawai‘i Island Study Area (after C&C of Honolulu 2021)

The Hāmākua Volcanics (Pleistocene) are between 64,000 and 300,000 years old. The Hāmākua Volcanics consists of basalt scoria cone vent deposits, ‘a‘ā and pāhoehoe lava flows, and the Waihū and Pōhakuloa Glacial Member that are primarily glacial till deposits (Sherrod et al., 2021).

Between 11,000 and 64,000 years, the Laupāhoehoe Volcanics (Holocene and Pleistocene) are divided into three volcanic members consisting of the “Younger volcanic rocks member”, the “Older volcanic rocks member”, and the “Mākanaka Glacial Member” (Sherrod et al., 2021). The younger volcanic rocks member consists of scoria cones (geologic symbol: Qlcy), lava flows (geologic symbol: Qly) consisting of ‘a‘ā and blocky ‘a‘ā with localized Pāhoehoe flows, and tephra-fall deposits (geologic symbol: Qlay) consisting of lapilli and ash (Sherrod et al., 2021). The older volcanic rocks member consists of tephra-fall deposits (geologic symbol: Qla) consisting of lapilli and ash; scoria cones (geologic symbol: Qlc), and lava flows distinguished as Benmoreite lava flows (geologic symbol: Qlb) (Sherrod et al., 2021). The Mākanaka Glacial Member consists of glacial till (geologic symbol: Qlmt) and glacial outwash (geologic symbol: Qlmo) (Sherrod et al., 2021).

5.2.4. Tabulated soils of the Hawai‘i Island study area

Table 4 lists the soils in the Hawai‘i Island study area. The table is based on the Web Soils Survey produced by the National Cooperative Soil Survey (NCSS) operated by the United States Department of Agriculture (USDA) Natural Resources Conservation Service (NRCS) (Web Soils Survey 2019). The table includes the mapped unit symbol, the map unit name, the number of acres of each soil type and the corresponding percent of the total area of interest. Only soils within 0.25 miles of the highway are shown in Table 4. There are 9 soil units mapped within this area of Route 19. A figure of the soil units is not provided in this report.

Table 4 Soils of the Hawaiʻi Island study area

Island of Hawaii Area, Hawaii			
Map Unit Symbol	**Map Unit Name**	**Acres in AOI**	**Percent of AOI**
901	Hilo hydrous silty clay loam, 0 to 10 percent slopes	1,400.5	19.9%
902	Hilo hydrous silty clay loam, 20 to 35 percent slopes	8.3	0.1%
903	Hilo hydrous silty clay loam, 10 to 20 percent slopes	1,778.8	25.3%
909	Hilo-Rock outcrop complex, 35 to 100 percent slopes	299.2	4.3%
951	Ookala medial silty clay loam, 0 to 10 percent slopes	176.0	2.5%
952	Ookala medial silty clay loam, 10 to 20 percent slopes	1,306.0	18.6%
953	Ookala medial silty clay loam, 20 to 35 percent slopes	136.1	1.9%
954	Ookala-Rock outcrop complex, 35 to 100 percent slopes	445.5	6.3%
967	Olaa cobbly hydrous loam, older substrate, 2 to 20 percent slopes	112.0	1.6%
Total Area of Interest		7,030.5	100

5.3. *Maui*

The Maui study area is along Highway Route 360, which generally runs along the coastline towards the north and east flanks of the Haleakalā shield volcano. It encompasses the areas upslope and downslope of the highway between Mileposts 0 and 35. The area is primarily natural terrain that is heavily vegetated with numerous stream-cut valleys and man-made cuts. Figure 19 shows the location of the study areas.

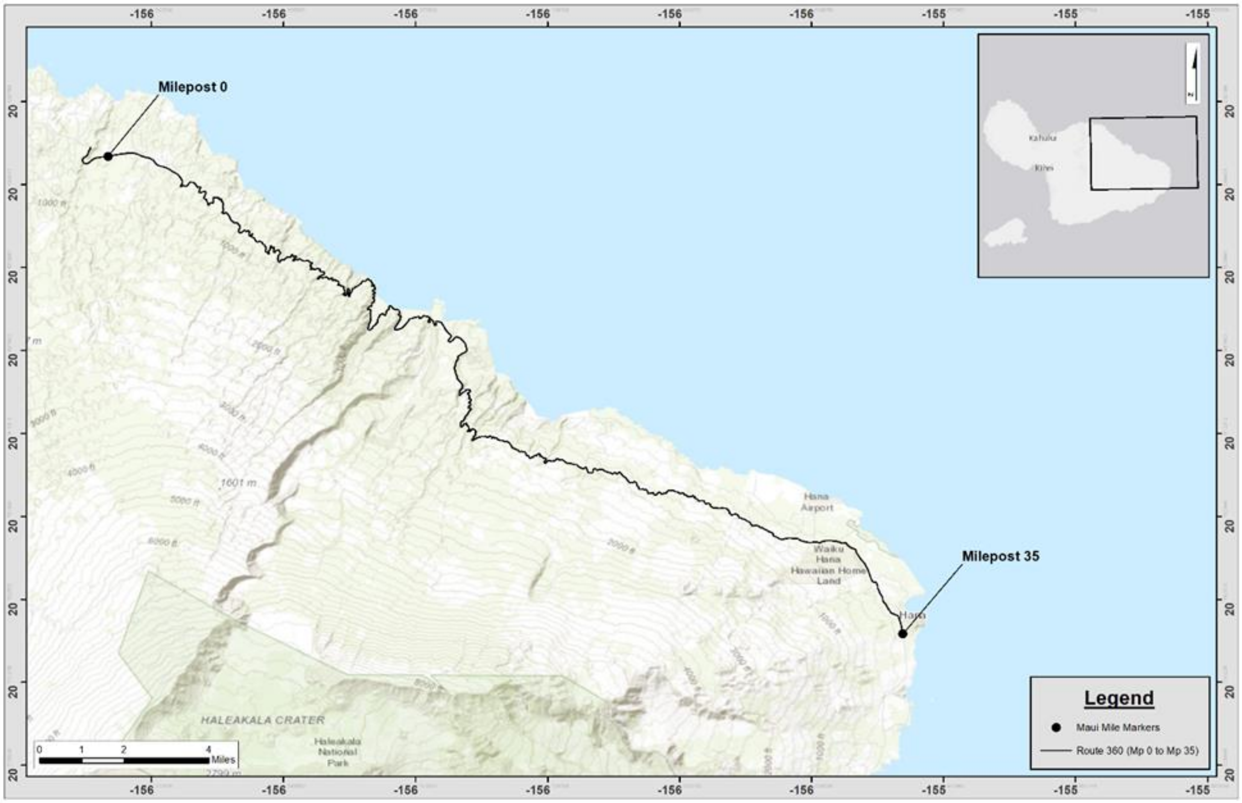

Figure 19 Map showing Maui study location (after ESRI 2014)

5.3.1. Topography of the Island of Maui Study Area

The Island of Maui's Route 360 topography is mapped in the United States Geological Survey's 2017, 7.5-minute Topographic Map of the Nāhiku Quadrangle, Hawaii – Maui County (USGS 2017). The scale of the map is 1:24,000. Contours within the map are provided every 100 feet. Figure 20 shows selected elevation contours associated with the Island of Maui study area.

The contour lines in Figure 20 are from the 100 ft contours for Maui Island GIS shapefile available through the Hawaii Statewide GIS program at the online Geospatial data portal and is based on the 30-meter USGS Digital Elevation Model (DEM) of the Island of Maui (C&C of Honolulu 2021). Note that only selected 100 ft contours greater than 1,000 ft are shown for the sake of brevity.

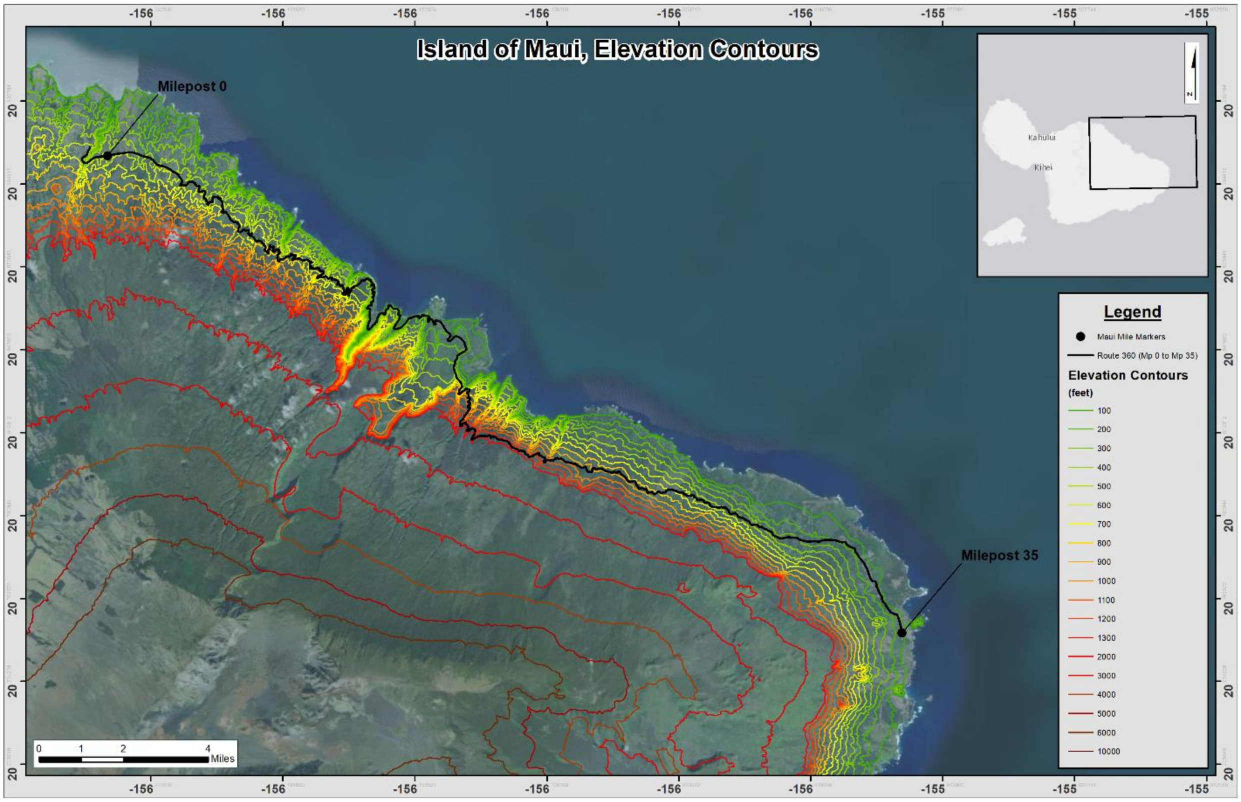

Figure 20 Island of Maui, Elevation Contours (after C&C of Honolulu 2021).

Highway elevations between milepost 0 and 35 vary from approximately 140 feet to nearly 1400 feet. Localized topography on either side of the highway changes significantly along the route. Elevations can be moderate to flat in residential areas, whereas sections that pass through natural stream valleys and man-made cuts can have slopes that are nearly vertical (USGS 2017).

The elevation at the peak of Haleakalā (Pu‘u ‘Ula‘ula) is at elevation 10,023 feet above MSL. The topography slopes towards the North or Northeast until it descends into the Pacific Ocean.

5.3.2. Annual rainfall of the Maui study area

The average annual rainfall for Route 360 on the Island of Maui in the Rainfall Atlas of Hawai‘i shows annual rainfall isohyet contours ranging from 65 inches per year to 220 inches per year (Giambelluca et al., 2013). Figure 21 shows the isohyets in the Maui study area.

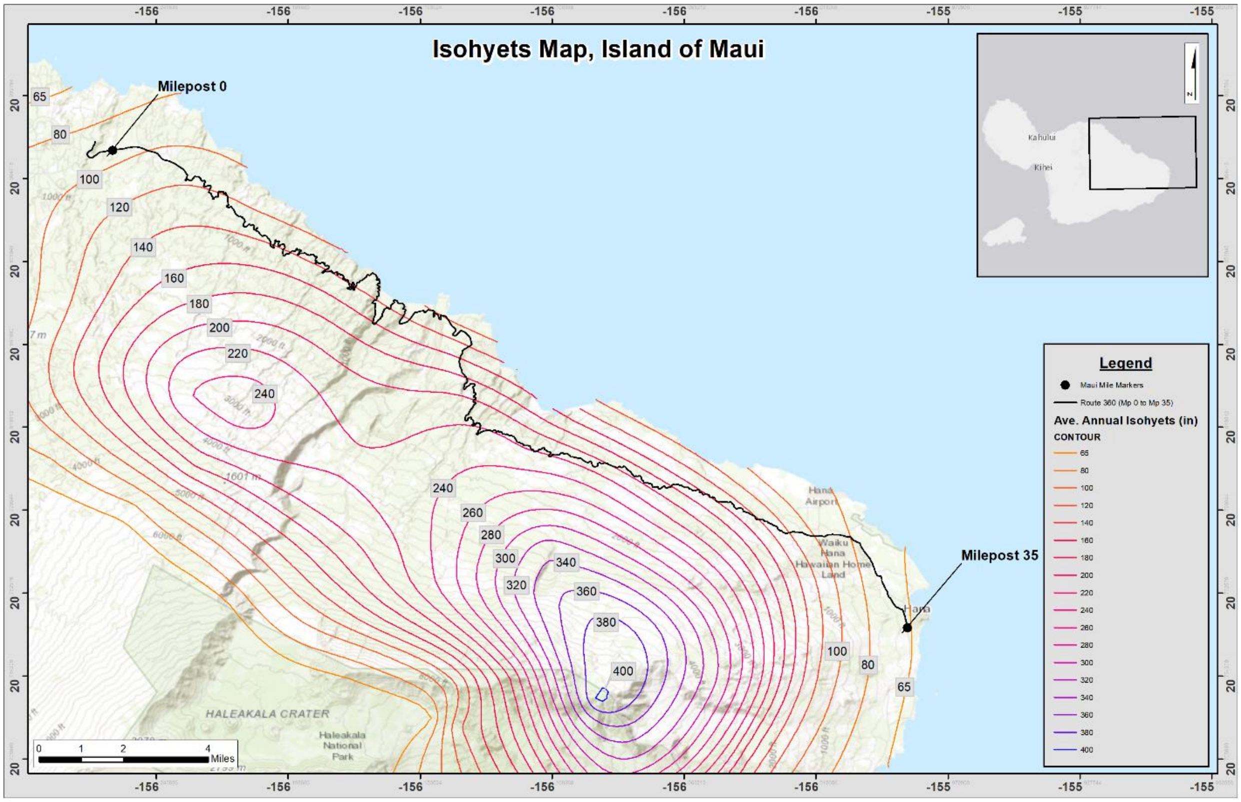

Figure 21 Isohyets Map, Island of Maui (after Giambelluca et al., 2013)

5.3.3. Geology of the Maui study area

The geology along Route 360 is mapped in the Geologic map of the State of Hawaiʻi as Kula Volcanics, Hāna Volcanics, Honomanū Basalt, and Older Alluvium (Sherrod et al., 2021). Figure 22 shows the geologic units in this area of the Island of Maui.

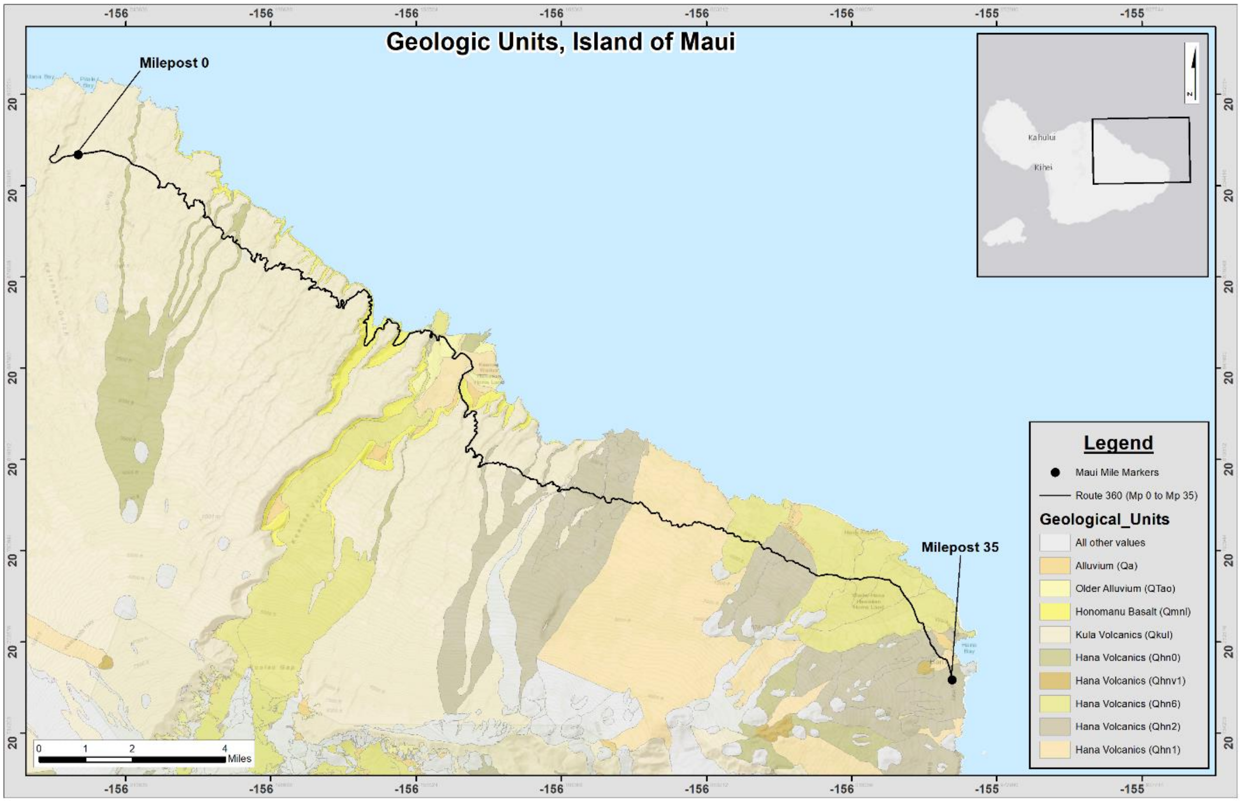

Figure 22 Geologic Units of the Island of Maui Study Area (after C&C of Honolulu 2021)

The Honomanū Basalt (Pleistocene) is between 0.95 and 1.3 million years old (Sherrod et al., 2021) and consists of both ‘a‘ā and Pāhoehoe lava flows.

Older Alluvium (Holocene and Pleistocene with a geologic symbol: (Qtao) are sedimentary deposits that are between 10,000 and 100,000 years old. It consists of the “Conglomerate of Ke‘anae” which is comprised of lithified sand and gravel.

Between 140,000 and 950,000 years old, the Kula Volcanics are divided into the following three members: lava flows, vent deposits, and intrusive rocks. Lava flows (geologic symbol: Qkul) are predominately ‘a‘ā with minor Pāhoehoe (Sherrod et al., 2021). Vent deposits (geologic symbol: Qhuv) consist of scoria and spatter with some spatter ramparts mainly from cinder cones

(Sherrod et al., 2021). Intrusive rocks (geologic symbol: Qhui) generally consist of dikes with similar composition and minerology as the Kula lava flow unit (Sherrod et al., 2021).

Between 13,000 and 30,000 years old, the Hana Volcanics (Holocene and Pleistocene) can be divided into five volcanic members but only three of the members occur in the vicinity of Route 360. They include: lava flows, vent deposits, and tephra deposits. Lava flows (geologic symbol: Qhn) are predominately ‘a‘ā with minor pāhoehoe (Sherrod et al., 2021). Vent deposits (geologic symbol: Qhnv) consist of scoria and spatter mainly from cinder cones (Sherrod et al., 2021). Tephra deposits (geologic symbol: Qhnt) generally consist of fallout tephra comprised of lapilli, ash, and crystals (Sherrod et al., 2021).

5.3.4. Tabulated soils of the Maui study area

Table 5 lists the soils in the Maui study area. The table is based on the Web Soils Survey produced by the National Cooperative Soil Survey (NCSS) operated by the United States Department of Agriculture (USDA) Natural Resources Conservation Service (NRCS) (Web Soils Survey 2019). The table includes the mapped unit symbol, map unit name, number of acres of each soil type and the corresponding percent of the area of interest. Only soils within 0.25 miles of the highway are shown in the table.

Table 5 Soils of the Maui study area

Island of Maui, Hawaii			
Map Unit Symbol	**Map Unit Name**	**Acres in AOI**	**Percent of AOI**
HKLD	Hana very stony silty clay loam, 3 to 25 percent slopes	1,518.1	14.2%
HKMD	Hana extremely stony silty clay loam, 3 to 25 percent slopes	112.8	1.1%
HKNC	Hana silty clay loam, moderately deep variant, 3 to 15 percent slopes	706.1	6.6%
HKOC	Hana extremely stony silty clay loam, moderately deep variant, 3 to 15 percent slopes	189.7	1.8%
HwC	Honolua silty clay, 7 to 15 percent slopes	202.4	1.9%
KBID	Kailua silty clay, 3 to 25 percent slopes	1,652.5	15.5%
MID	Makaalae silty clay, 7 to 25 percent slopes	1.5	0.0%
MYD	Malama extremely stony highly decomposed plant material, 3 to 20 percent slopes, MLRA 159A	1,155.0	10.8%
OPD	Opihikao - Lava flows complex, 0 to 6 percent slopes, MLRA 159A	5.0	0.0%
PfB	Pauwela clay, 3 to 7 percent slopes	41.5	0.4%
PfC	Pauwela clay, 7 to 15 percent slopes	380.3	3.6%
PfD	Pauwela clay, 15 to 25 percent slopes	480.0	4.5%
rHOD	Honomanu silty clay, 5 to 25 percent slopes	728.6	6.8%
rHR	Honomanu-Amalu association	0.7	0.0%
rLW	Lava flows, aa	176.0	1.7%
rRK	Rock land	13.7	0.1%
rRO	Rock outcrop	0.0	0.0%
rRR	Rough broken land	647.6	6.1%
rRT	Rough mountainous land	1,703.4	16.0%
rSM	Stony alluvial land	388.0	3.6%
TR	Typic Endoaquepts mucky silt loam, 1 to 15 percent slopes, MLRA 164	89.9	0.8%
W	Water > 40 acres	15.5	0.1%
Total Area of Interest		10,654.8	100.0

6. PROJECT METHODOLOGY AND DATASETS

6.1. *Programs Used for Analysis*

SBAS processing was conducted using SARscape, a toolbox from Sarmap implemented as a plug-in within the ENVI/IDL environment. Post-processing of SBAS results and figure creation was conducted in ArcMap Desktop and ArcGIS Pro.

6.2. *Datasets and Repositories*

Synthetic aperture radar SLC files and associated files were downloaded from various Distributed Active Archive Centers (DAACs). The Space Shuttle Radar Topography Mission (STRM) 10-meter DEMs were used in processing of datasets for the study locations. The STRM 10-meter DEMs were downloaded through the USGS EROS Archive – Digital Elevation – Shuttle Radar Topography Mission (STRM) (USGS 2018).

Sentinel-1 (Copernicus 2014-2021) and ALOS-PALSAR-1(© JAXA 2006-2011) Single-Look-Complex images were downloaded from the Alaska Satellite Facility's Vertex DAAC. Sentinel-1 orbital auxiliary files were downloaded from Copernicus Sentinels Pre-Operational Products (POD) Data Hub (Copernicus 2014-2021).

Additional searches for Jers-1, ALOS-PALSAR-2, and ALOS/PRISM data were conducted at: ALOS-2 data for scientific research (ALOS Research Announcement Office); the Remote Sensing Technology Center of Japan (RESTEC); PASCO Corporation; and JAXA's G-Portal. Additional attempts to retrieve ALOS/PRISM images from the European Space Agency (ESA) On-line Data Dissemination system were also conducted. Radarsat-1 searches were conducted at the Canadian Space Agency's (CSA) Earth Observation Data Management system and at the (ESA) On-line Data Dissemination system. However, these searches were either unfruitful or the costs were too exorbitant (~$2000/image).

6.3. *SBAS Processing Steps*

SBAS processing within SARscape is generally conducted using the following steps: Image download, import, and sample selection; Connection graph generation; Interferometric processing; Refinement and re-flattening; Inversion-First Step; Inversion-Second Step; and Geocoding. The following sections 6.3.1 through 6.3.7, review the processing steps and input parameters.

6.3.1. Image download, import, and sample selection

SLC images were download from the repositories mentioned above. Import/conversion to ENVI formatted files was required prior to conducting SBAS processing. Selection for the sampled areas was made for the study locations within the larger SLC images. Each SLC image was cut to the selected sample areas during the import step to reduce the processing time of datasets. The cut sample areas for Oʻahu, Hawaiʻi Island and Maui are approximately 63, 161 and 197 square miles, respectively, not including water surfaces. The SBAS processing time for each study location is dependent on the size of sample area and the number of SLC images.

6.3.2. Connection graphs

Connection graphs were generated to determine the SLC Master and Slave pair combinations to allow the generation of differential interferograms. The pairs are shown through connections displayed in time-position and time-baseline plots. For N number of SLC images, the theoretical maximum number of differential interferograms generated, where each SLC is connected to every other SLC image, would be (N*(N-1))/2. Examples of a time-position and a time-baseline plots are provided in Figures 23 and 24, respectively. The examples shown are for illustration purposes and are not representative of any of the datasets used for analysis. The connection graph examples were generated from 20 images collected between January and May of 2021. Each green diamond in the plots represents a single SLC image. The yellow diamond shown on the left side of the time-position and time-baseline plots represents the Super-Master image.

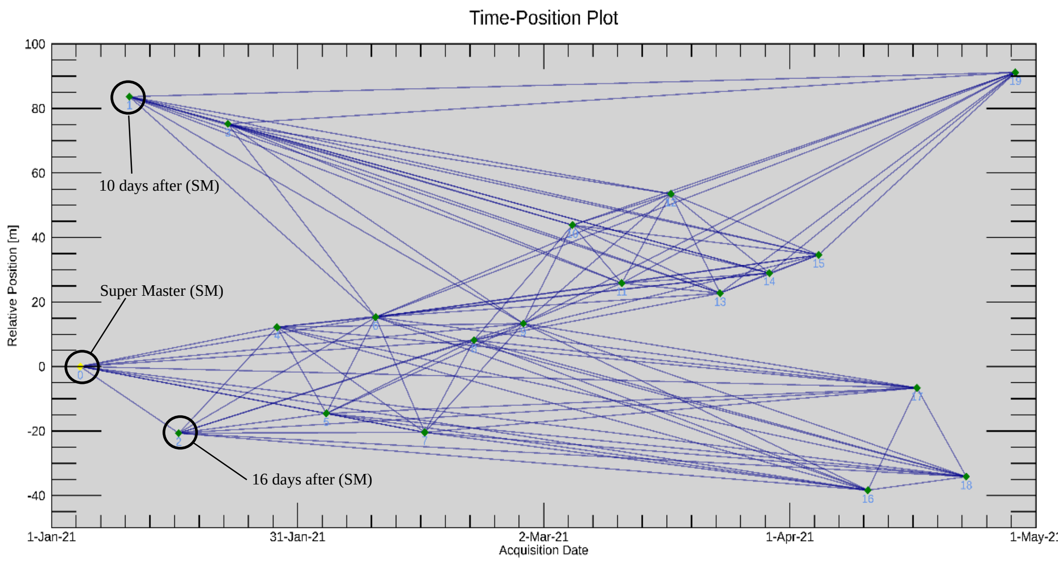

Figure 23 Example time-position plot for connection graph

In the above time-position plot, the x-axis represents time. The y-axis represents the relative position of the satellite in space during the acquisition of individual images. The position of each subordinate SLC image (green diamonds) is relative to the position of the Super-master SLC image (yellow diamond). Note that the Super-Master image is set at the value of 0 on the y-axis. In the above plot, the image acquired 10 days after the Super-master image was taken from a position that was approximately 82 meters from the position of the Super-master. The image acquired 16 days after the Super-Master image was taken from a position approximately 20 meters away.

The lines between each of the diamonds represent a single differential interferogram formed between the two SLC images. For the example, each image was set to have 10 connections with other images. The number of connections can be increased or reduced based on the number of images available in the dataset. In Figure 23, the Super-master image happens to be the oldest image in the dataset, however, this is not a requirement. The super-master image is automatically selected by the algorithm to allow an arrangement with connections that minimizes the temporal and spatial differences between all image pairs. The operator of the program should choose the number of interferogram pairs per image in a manner that balances having enough connections and having the smallest possible temporal differences.

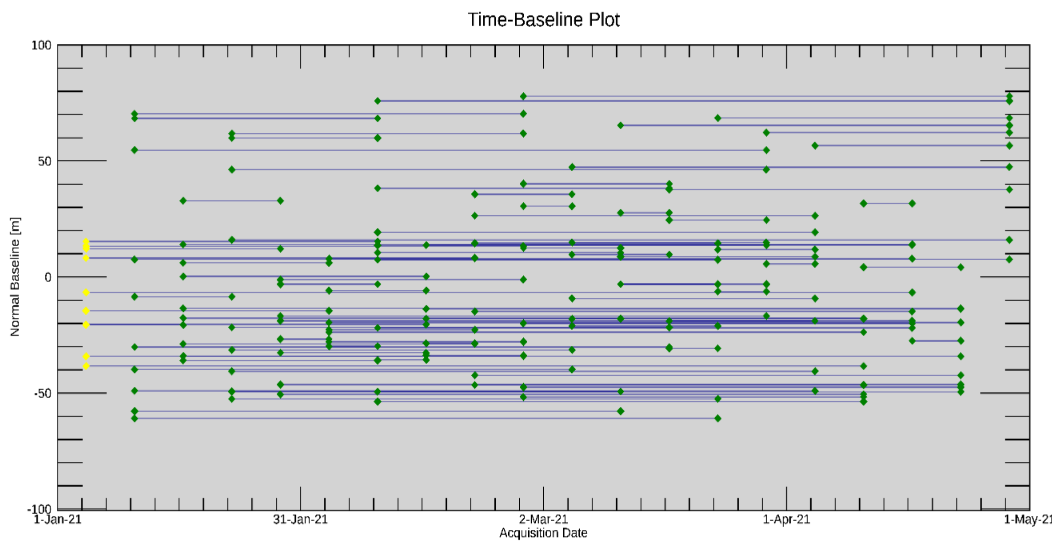

Figure 24 Example time-baseline plot for connection graph

In an example Time-baseline plot (Figure 24), the x-axis represents time. Each green diamond represents a slave SLC image and the yellow diamonds represent a single image known as the Super-master image. The Super-master is an image selected by the SBAS algorithm that all other images (slave images) are referenced to. The y-axis is an adjusted distance of the satellite's position in space from the position of acquisition of the Super Master. The adjusted distance is representative of the distance in space between interferometric pairs relative to the position in space of the Super-master image during acquisition. For example, if the relative position of image

A to the Super-master image was 80 meters and the relative position of image B was 85 meters, the image pair on the Time-baseline plot would be placed at +5 meters on the y-axis. The distance between the two images on the x-axis represents the difference in time between the image acquisitions. The blue lines tie images as interferometric pairs.

6.3.3. Interferometric processing

During interferometric processing, wrapped and unwrapped interferometric stacks (collections of interferograms) are created based on the connections established in the connection graph step. Interferometric processing in SARscape requires three sub-steps: Co-registration, differential interferogram generation, and 2D phase unwrapping (SARMAP 2021).

For co-registration, each of the SLC images is co-registered with a digital elevation model (DEM) that is either previously generated within the program or acquired from available repositories. The co-registration sub-step re-samples the SLC images so that they have the same spatial resolution as the DEM (SARMAP 2021). The spatial resolution of the DEM affects the precision of the SBAS results; therefore, it is advantageous to have access to the highest resolution DEMs available. As mentioned in the dataset and repositories section above, (SRTM) 10-meter DEMs were used for SBAS processing.

The differential interferogram generation sub-step is implemented using the standard DinSAR approach (SARMAP 2021). During this sub-step, each wrapped and unwrapped interferogram is generated based on the previously processed co-registered SLC images.

Standard 2D first phase unwrapping is conducted in the last interferometric processing sub-step to establish initial filtering for the datasets. For phase unwrapping, the user must set several parameters that will affect the interferometric processing results. These include: the number of range and azimuth looks to be considered; the grid size for suggested looks; the unwrapping method type; the unwrapping decomposition level; the unwrapping coherence threshold; and the filtering method.

During SAR image acquisition, a point on the ground will be captured by the satellite receiver several times from different positions in space. The receiver “looks” at a point from the different positions in space in both the range direction and azimuth direction. The range and azimuth concepts are presented in Sections 2.1 and 2.2 of this report. Selection of range and azimuth looks greater than values of 1 is necessary in order to reduce the signal to noise ratio of the interferograms and also to achieve higher coherence of each interferogram (SARMAP 2021). The number of range and azimuth looks chosen will be based on the spatial size of the area for analysis, the number of interferograms to be processed, and the amount of time available for processing. Smaller datasets will allow the user to choose higher range and azimuth looks to be considered.

The grid size for suggested looks is selected based on the horizontal resolution of the SLC datasets and based on the spatial resolution of the DEM used for co-registration. With Sentinel-1, datasets having a spatial resolution of 20 meters by 5 meters and the 10-meter (STRM) DEM, the grid size for suggested looks was set to 15 meters for the datasets.

The unwrapping method types available consist of: Regional growing method; minimum cost flow method (square grid); or the Delaunay Minimum Cost Flow Method (triangular grid) (SARMAP 2021). The type of unwrapping method selected should be based on the type of information the user is trying to achieve and with consideration of the topography of the region of analysis. The Delaunay Minimum Cost Flow Method was used for this report because it is generally used for landslide detection and for areas with high topographic variation.

The unwrapping decomposition level determines the number of under sampling levels to be applied to interferograms prior to unwrapping (SARMAP 2021). For this report, the unwrapping decomposition level was set to 1 for faster processing time.

An initial coherence threshold is set during the interferometric processing step. Coherence thresholds are selected at varying stages of SBAS processing; however, for this analysis a single coherence value of 0.1 was used. Pixels with a coherence value less than that selected for a particular processing step will be ignored for the remainder of processing (SARMAP 2021). The coherence threshold is typically not set to be greater than 0.4 to 0.5 because setting the value higher would result in a significant reduction of SBAS datapoints. Individual interferogram pixels generally do not have coherence greater than 0.4 or 0.5 for vegetated areas. If there is a lot of vegetation and/or topographic variation of the analysis areas, the coherence threshold is generally set to a lower value. The coherence threshold for the interferometric processing step in each dataset was set to 0.1.

For the unwrapping filtering method, the following choices are available: Boxcar window; Goldstein; Adaptive window; or Adaptive non-local InSAR (SARMAP 2021). For this study, the Goldstein method was selected because it is generally considered to be the preferred filtering method for landslide detection due to the ability of the method to generally preserved fringe edges (Feng et.al., 2016)

After interferometric processing is complete, it is necessary to examine the individual interferograms in the interferometric stack to determine if poor interferometric pairs are present. Examination of interferometric pairs should consider the following: uncoherent pairs; inaccurate orbits phase ramps; atmospheric artifacts; and residual topographic effects (SARMAP 2021). Phase ramps, atmospheric artifacts, and residual topographic effects can be identified in the interferograms. Non-coherent pairs can be identified by examination of gray-scale coherence images generated in parallel with the interferograms (Figure 25A). Figure 25 provides an example of the interferometric images to be examined to determine if unwanted interferometric pairs are present.

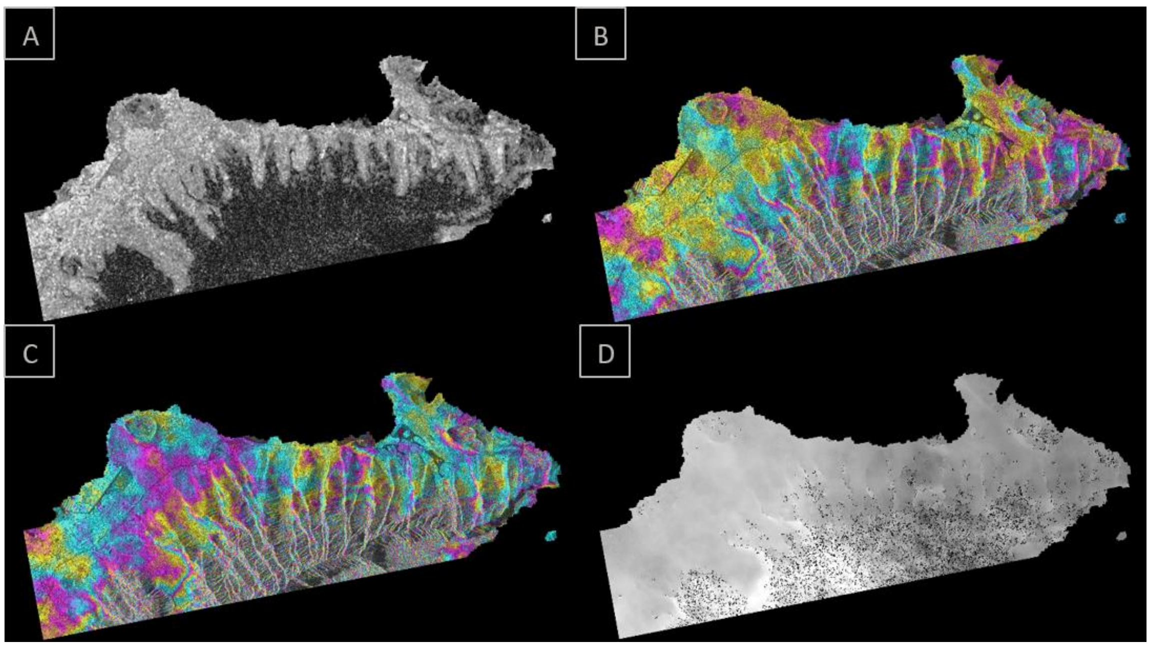

Figure 25 Interferometry images: A) Coherence image; B) Wrapped interferogram; C) Unwrapped interferogram; D) Unwrapped phase image.

If noisy interferograms are identified during examination, the pairs are deleted and the connection graph is edited to re-determine the connections. An example of a noisy/undesirable interferogram is provided below on the right side of Figure 26. The accompanying coherence image is shown on the left side of Figure 26, note the low coherence (dark) pixels in the left image.

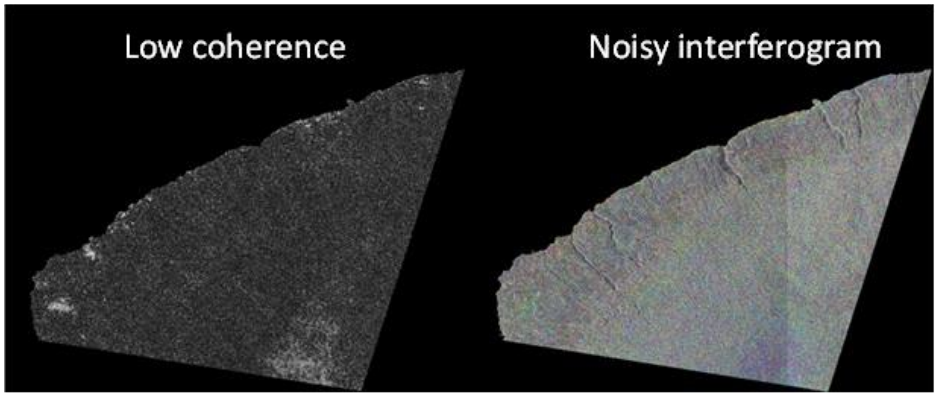

Figure 26 Low coherence (left), noisy interferogram (right)

6.3.4. Refinement and re-flattening

The refinement and re-flattening step is performed in order to estimate the phase offsets and phase ramps remaining after the interferometric processing is complete (SARMAP 2021). Refinement and re-flattening create an unwrapped interferometric stack from the previously wrapped stack and then creates a wrapped interferometric stack from the previously unwrapped stack. The changes from wrapped-to-unwrapped and unwrapped-to-wrapped allow for phase offset and phase ramp identification. After the remaining phase offsets and phase ramps are identified they are deleted. The step requires selection of Ground-Control-Points (GCPs) from areas known to have minimal change in each interferogram. GCPs are used in additional processing steps as tie-points or common anchor points for interferometric pairs in the dataset interferometric stack (SARMAP 2021). 20-30 GCPs are typically selected for SARscape processing (SARMAP 2021). Figure 27 is an example of GCPs selected in areas of high coherence for the O‘ahu dataset. The unwrapped phase image is used for selection of GCPs. Coloring of the images was set with a rainbow ramp that allowed for easy identification of coherent areas that are shown as green in the figure. GCPs are symbolized with black plus signs.

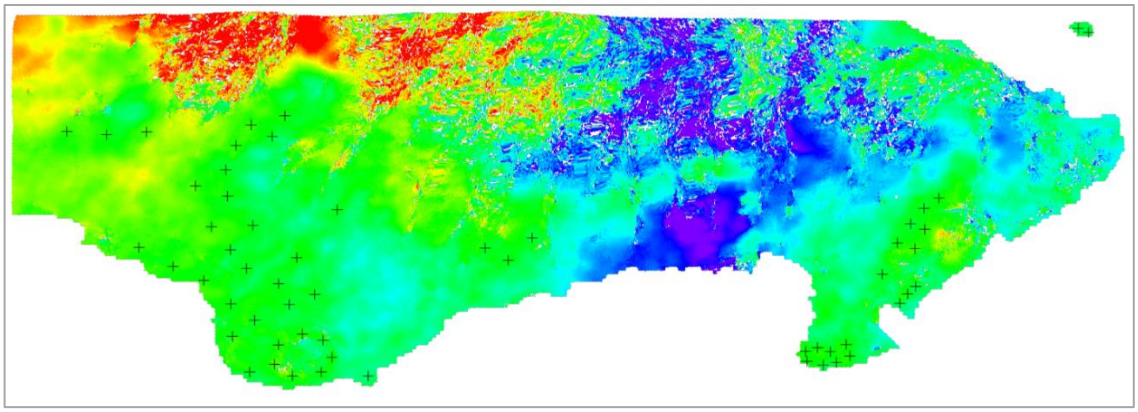

Figure 27 Example of selected ground control points for the O'ahu study area

6.3.5. Inversion: First Step

The Inversion-First Step is conducted to determine the parameters of the best fit trend of deformation. The best fit trend is based on the measured characteristics or "behavior" of the study area (SARMAP 2021). These characteristics include the topography and amount of displacement likely occurring in the area. In the first Inversion, estimates of the residual topography and displacement velocity are made by means of matrix inversion based on the Single Value Decomposition (SVD) approach (SARMAP 2021). Both residual topography and displacement velocity are estimated from the unwrapped interferometric stack created during the refinement and re-flattening. The estimates for residual topography and displacement velocity are then subtracted from the wrapped interferometric stack. This subtraction produces a temporally wrapped stack. The temporally wrapped stack is unwrapped to produce a temporally unwrapped stack. The initial estimate of displacement velocity is then added to the temporally unwrapped stack to produce a second unwrapped stack that is then re-flattened for additional processing.

During the Inversion-First Step, several parameters must be selected. These include: the product coherence threshold; the displacement model type; whether or not to estimate the residual height; the spatial wavelet size in meters; whether or not to allow for disconnected blocks; the minimum number of valid interferograms for processing; whether or not to stop before unwrapping; the unwrapping method type; the unwrapping decomposition level; and the unwrapping coherence threshold.

Coherence thresholds are set twice during the Inversion-Frist Step. The coherence threshold for the final product must be considered during the Inversion-First step to guide the remainder of SBAS processing (SARMAP 2021).

The following choices are available for selection of the displacement model type: no displacement; linear; quadradic; cubic; or linear periodic. Selection of no displacement is chosen when considering stable areas for generation of DEMs. When the linear process is selected, the displacement velocity in millimeters per year (mm/yr) is calculated. If quadradic is selected, both the displacement acceleration and velocity are calculated. Acceleration is calculated in millimeters per year squared (mm/yr^2) and displacement in millimeters per year (mm/yr). The cubic model type calculates the displacement acceleration variation (mm/yr^3), the acceleration (mm/yr^2), and the velocity (mm/yr). The linear periodic model type calculates the periodic delay (days), the periodic modulation in millimeters (mm), and the velocity (mm/yr) (SARMAP 2021). The processing time increases with increasing complexity of model type from no displacement to linear periodic.

Choosing to estimate the residual height should be selected when generating precise DEMs. Estimating residual heights also requires that “no displacement” for “model type” also be selected. Estimating the residual height was not included in the processing steps for this report.

Selection of the Spatial Wavelet Size in meters is conducted to remove the low pass distortion below the value chosen. The process is also conducted to preserve spatial details by conducting wavelet decomposition (SARMAP 2021). Selection of the spatial wavelet size requires the user to consider the elevation of the study area.

Choosing whether to allow disconnected blocks or not is required when there may be data gaps within the entire temporal baseline of the study. For example, Sentinel-1 data for Hawai‘i and North America often have no data available from late-2016 to mid-2018. The user should consider whether or not data available from 2014 to late 2016 holds value to the information for an SBAS study. If disconnected blocks are not allowed, the 2014 to late 2016 data will be deleted from the connection graph. If disconnected blocks are allowed, the 2014 to late 2016 data will be included in the dataset as a separate connection graph from data available after mid-2018.

Selection of the minimum percent of valid interferograms is conducted as part of the quality assurance for SBAS analysis. The selection sets a minimum threshold for accepted SBAS inversion equations that are valid (SARMAP 2021). Having greater than 6o percent valid interferograms is typical for analysis with robust datasets. A minimum of 60 percent valid interferograms was selected for Sentinel-1 data. A minimum of 45 percent valid interferograms was selected for the Hawai‘i Island ALOS-1, PALSAR-1 data.

Selection of the unwrapping method types is required for unwrapping conducted in the Inversion-First Step. It is typical to select the same method as was used during Interferometric Processing. The available methods are: Regional growing method; minimum cost flow method (square grid); or the Delaunay Minimum Cost Flow Method (triangular grid) (SARMAP 2021). The Delaunay Minimum Cost Flow Method was used for processing of the datasets. Note that selection of the unwrapping method is also conducted during the Inversion-Second Step.

Selection of unwrapping decomposition level determines the number of under sampling levels to be applied to interferograms prior to unwrapping (SARMAP 2021). During the Inversion-First

Step, it is possible to increase the level of decomposition to allow for improved quality of results of the second wrapped interferograms (SARMAP 2021). Increasing the decomposition level is possible because there is less risk for aliasing of the dataset due to the amount of processing conducted in previous steps. The interferograms contain less noise because inversion of the dataset has filtered out the topographic portion of the phase measurements.

A coherence threshold for the second unwrapped interferograms is set during the Inversion-First Step. The threshold set during interferometric processing will filter out individual pixels in interferograms by setting the pixel values to NaN for the remainder of processing (SARMAP 2021).

At the completion of the Inversion-First Step, the dataset (interferometric stack) should no longer contain any static topography as part of the phase measurements.

6.3.6. Inversion: Second Step

The purpose of the Inversion-Second Step is to remove the measurements associated with atmospheric phase delay, atmospheric phase interference, and random noise. The Inversion-Second Step uses matrix inversion based on the Single Value Decomposition (SVD) approach (SARMAP 2021). The SVD approach is used to review the initial displacement estimates determined in the Inversion-First Step on a date-by-date basis. The displacements are reviewed using SVD to filter out the atmospheric phase delay from the displacement estimates (SARMAP 2021). After filtering for atmospheric phase delay, the filtered estimate of displacement is temporarily removed from the interferometric stack to preserve the displacement estimates during the next step that involves high-pass and low-pass filtering (SARMAP 2021). While the displacement estimates are temporarily removed, additional filtering is conducted with atmospheric phase screens consisting of spatial high-pass filters and temporal low-pass filters. The spatial and temporal filters are applied to the interferometric stack to create layers that are proportional to the atmospheric and noise artifacts (SARMAP 2021).

During the Inversion-Second Step, the user must set several parameters. These include: the product coherence threshold; whether to interpolate disconnected blocks; the minimum number of valid interferograms; the minimum number of valid acquisitions; the atmosphere low pass size; the atmosphere high pass size; and the refinement residual polynomial degree.

Once again, the product coherence threshold is required. The same value of product coherence threshold set during the Inversion-First Step should be selected.

Allowing for interpolation of disconnected blocks is used for interpolating solutions for portions of the time-series that have temporal gaps where displacement measurements do not exist (SARMAP 2021). This option was selected for the ascending O‘ahu dataset, the ascending Hawai‘i Island dataset, and the descending dataset for the Island of Maui. The option was not selected for the descending O‘ahu and Hawai‘i Island datasets.

Selection of the minimum percent of valid interferograms sets a minimum threshold for accepted SBAS inversion equations that are valid. Selection of greater than 60 percent valid interferograms is typical for analysis with robust datasets (SARMAP 2021). For analysis in this report, 60 percent was used for Sentinel-1 datasets and 45 percent was used for ALOS data. The minimum percent of valid interferograms for the ALOS data had to be reduced to 45 percent due to the limitations of the dataset. Less than 50% of the ALOS interferograms were valid due to the limited number of available images and temporal gaps between each image. Had the value been kept at 60 percent, the ALOS data processing would have failed.

Selection of the minimum percent of valid acquisitions sets a minimum threshold for accepted SBAS inversion equations that are valid over a certain coherence threshold. Selection of greater than 80 percent valid interferograms is typical. A minimum of 80 percent was set for analysis in this report.

Entering a “window size” in meters is required when applying the atmospheric low pass spatial distribution filter (SARMAP 2021). The window size should be generally proportional to the anticipated atmospheric interference. For the report analysis, the window size was set to the recommended value of 1600 m for low pass spatial distribution (SARMAP 2021).

A “window size” in days is required when applying the atmospheric high pass temporal distribution filter (SARMAP 2021). For the datasets, the window size for the high pass temporal distribution filter was set to 365 days for each of the interferometric stacks.

For the study areas, only the phase offset was required to be corrected for the refinement residual polynomial degree.

Following the Inversion-Second Step, the datasets should no longer contain atmospheric phase delay, interference, or random noise. Because residual topography is removed during the previous Inversion-First Step. The datasets should consist solely of time-displacement values.

6.3.7. Geocoding

After the Inversion steps are complete, the results are geocoded in both shape (vector) files and raster file formats (SARMAP 2021). For this report, shape files were primarily used for analysis of the study site datasets to generate time-series plots in SARscape and plots resulting from shapefile attribute tables reviewed in ArcGIS. Raster files were primarily used for review of time-series animations to observe dataset behavior.

6.4. *O‘ahu Parameters and Datasets*

Sentinel-1 SBAS analysis was conducted for the O‘ahu study area using both descending and ascending datasets. Attempts to conduct SBAS analysis for the O‘ahu study area using descending and ascending ALOS-1 and PALSAR-1 data were not successful due to there being too few scenes available and significant temporal gaps between acquisition dates.

6.4.1. O‘ahu (Sentinel-1, Descending)

The descending dataset consists of 194 images acquired between November 28, 2015, and December 14, 2021. 99 images were acquired with the Sentinel-1A satellite and 95 dataset images were acquired with the Sentinel-1B satellite. The ascending data were collected from the right-looking sensor/receiver at an approximate off-nadir incidence angle of 36.26˚. Only images from Path Number 160 and Frame Number 520 were used for descending analysis. The approximate look-angle of the satellite (clockwise from North) was estimated to be 280˚. Only Co-polarized (VV) images were selected for analysis.

Connection graph parameters were set to guide Time-Position and Time-Baseline connections. The minimum normal baseline was set at 0% and maximum normal baseline was set to 5%. The minimum temporal baseline was set to 0 days and the maximum temporal baseline was set to 120 days. The redundancy criteria were chosen based on the minimum temporal baseline with the degree of redundancy set as Low. The minimum connections per acquisition were limited to 10. Disconnected blocks were permitted for the analysis due to a data gap between acquisitions from October 23, 2016, to November 6, 2018.

With the above criteria for the connection graph, 953 unique interferogram pairs were identified by the algorithm for analysis. The mean normal baseline was 48.84%, maximum absolute normal baseline was 220.35%, and the minimum absolute baseline was 0.16%. The mean absolute temporal baseline was approximately 21.77 days. The maximum temporal baseline was 120 days, and the minimum was 6 days. The 34th image, acquired on March 30, 2019, was selected as the super master SLC image.

6.4.2. O‘ahu (Sentinel-1, Ascending)

The ascending dataset consisted of 177 images acquired between October 28, 2018, and December 11, 2021. 88 dataset images were acquired with the Sentinel-1A satellite and 89 dataset images were acquired with the Sentinel-1B satellite. The ascending data were collected from off-nadir incidence angle of 36.26˚. Only images from Path Number 22 and Frame Number 64 were used for ascending analysis. The approximate look-angle of the satellite (clockwise from North) was estimated to be 79˚. Only Co-polarized (VV) images were selected for analysis.

Connection graph parameters were set to guide Time-Position and Time-Baseline connections. The minimum and maximum normal baselines were set as 0% and 5%, respectively. The minimum and maximum temporal baselines were set to 0 and 120 days, respectively. The degree of redundancy criteria was chosen based on the minimum temporal baseline as Low. The minimum connections per acquisition were limited to 10. Disconnected blocks were not permitted for the analysis.

With the above criteria for the connection graph, 892 unique interferogram pairs were identified by the algorithm for analysis. The mean normal baseline was 50.57%, maximum absolute normal baseline was 219.59%, and the minimum absolute baseline was 0.88%. The mean absolute temporal baseline was approximately 20 days. The maximum temporal baseline was 66 days, and the minimum was 6 days. The 113th image, acquired on November 22, 2020, was selected as the super master SLC image.

6.5. *Hawai‘i Island Parameters and Datasets*

Sentinel-1 SBAS analysis was conducted for the Hawai‘i Island study area using both descending and ascending datasets. ALOS-1 and PALSAR-1 SBAS analyses using descending data were successfully conducted, however, attempts to conduct analyses using ascending data were not successful. It is likely that failure to conduct analysis on ascending ALOS-1 and PALSAR-1 data is due to the limited number of scenes available because of the radar shadow by Mauna Kea

6.5.1. Hawai‘i Island (Sentinel-1, Descending)

The descending dataset consisted of a total of 194 images acquired between June 6, 2018, and December 15, 2021. 102 dataset images were acquired with the Sentinel-1A satellite and 93 dataset images were acquired with the Sentinel-1B satellite. The ascending data were collected from an off-nadir incidence angle of 36.26˚. Only images from Path Number 87 and Frame Number 524 were used for descending analysis. The approximate look-angle of the satellite (clockwise from North) was 280˚. Only Co-polarized (VV) images were selected for analysis.

Connection graph parameters were set to guide Time-Position and Time-Baseline connections. The minimum normal baseline was set to 0% and maximum normal baseline was set to 5%. The minimum temporal baseline was set to 0 days, the maximum temporal baseline was set to 120 days. The redundancy criteria were chosen based on the minimum temporal baseline with degree of redundancy as Low. The minimum connections per acquisition were limited to 10. Disconnected blocks were not permitted for the analysis.

With the above criteria for the connection graph, 974 unique interferogram pairs were identified by the algorithm for analysis. The mean normal baseline was 49.43%, maximum absolute normal baseline was 176.66%, and the minimum absolute baseline was 0.72%. The mean absolute temporal baseline was approximately 21.32 days. The maximum temporal baseline was 120 days, and the minimum was 6 days. The 53rd image, acquired on March 31, 2019, was selected as the super master SLC image.

6.5.2. Hawai‘i Island (Sentinel-1, Ascending)

The ascending dataset consisted of a total of 185 images acquired between May 20, 2018, and December 12, 2021. 90 dataset images were acquired with the Sentinel-1A satellite and 95 dataset images were acquired with the Sentinel-1B satellite. The ascending data were collected from the right-looking sensor/receiver at an approximate off-nadir incidence angle of 36.26˚. Only images from Path Number 124 and Frame Number 60 were used for ascending analysis. The approximate look-angle of the satellite (clockwise from North) was estimated to be 79˚. Only Co-polarized (VV) images were selected for analysis.

Connection graph parameters were set to guide Time-Position and Time-Baseline connections. The minimum normal baseline was set to 0% and maximum normal baseline was set to 5%. The minimum temporal baseline was set to 0 days, the maximum temporal baseline was set to 120 days. The redundancy criteria were chosen based on the minimum temporal baseline with degree of redundancy as Low. The minimum connections per acquisition were limited to 10. Disconnected blocks were not permitted for the analysis.

919 unique interferogram pairs were identified by the algorithm for analysis. The mean normal baseline was 46.83%, maximum absolute normal baseline was 168.45%, and the minimum absolute baseline was 0.37%. The mean absolute temporal baseline was approximately 19.65 days. The maximum temporal baseline was 84 days, and minimum 6 days. The 42nd image, acquired on August 01, 2019, was selected as the super master SLC image.

6.5.3. Hawai‘i Island (ALOS-1, PALSAR-1, Descending)

The descending dataset consisted of a total of 13 images acquired between May 28, 2006, and March 11, 2011. All images were acquired with the ALOS-PALSAR satellite. The descending data was collected from the right-looking sensor/receiver at an approximate off-nadir incidence angle of 34.3˚. Only images from Path Number 601 and Frame Number 3220 were used for descending analysis. The approximate look-angle of the satellite (clockwise from North) was estimated to be 280˚. Only Co-polarized (HH) images were selected for analysis.

Connection graph parameters were set to guide Time-Position and Time-Baseline connections. The minimum normal baseline was set as 0% and maximum normal baseline was set to 45%. The minimum temporal baseline was set to 0 days, the maximum temporal baseline was set to 1000 days. The redundancy criteria were chosen based on the maximum temporal baseline with degree of redundancy as high. The minimum connections per acquisition were limited to 5. Disconnected blocks were not permitted for the analysis.

With the above criteria for the connection graph, 57 unique interferogram pairs were identified by the algorithm. The mean normal baseline was determined to be 1186.95%, maximum absolute normal baseline was 2725.45%, and the minimum absolute baseline was 185.24%. The mean absolute temporal baseline was found to be approximately 482 days. The maximum temporal baseline was determined to be 966 days, and minimum 46 days. The 6th image acquired on July 18, 2008, was selected as the super master SLC image.

6.6. ***Island of Maui Parameters and Datasets***

Sentinel-1 SBAS analysis was conducted for the Island of Maui study area using the descending dataset only. Attempts to conduct analyses on ascending Sentinel-1 data and both ascending and descending ALOS-1, PALSAR-1 data were not successful. It is likely that failure to conduct analysis for Sentinel-1 (ascending) and ALOS-1, PALSAR-1 datasets is due to the radar shadow caused by Haleakalā. Having a limited number of scenes available for the ALOS-1, PALSAR-1 sensor is also likely a significant factor in the failure of ALOS SBAS processing.

6.6.1. Island of Maui (Sentinel-1, Descending)

The descending dataset consisted of 199 images acquired between November 11, 2015, and December 21, 2021. 105 dataset images were acquired with the Sentinel-1A satellite and 94 dataset images with the Sentinel-1B. The descending data was collected from the off-nadir incidence angle of 36.26˚. Only images from Path Number 87 and Frame Number 522 were used for descending analysis. The approximate look-angle of the satellite (clockwise from North) was estimated to be 280˚. Only Co-polarized (VV) images were selected for analysis.

Connection graph parameters were set to guide Time-Position and Time-Baseline connections. The minimum normal baseline was set as 0% and maximum normal baseline was set to 5%. The minimum temporal baseline was set to 0 days, the maximum temporal baseline was set to 120 days. The redundancy criteria were chosen based on the minimum temporal baseline with degree of redundancy as Low. The minimum connections per acquisition were limited to 10. Disconnected blocks were permitted for the analysis due to there being a data gap between acquisitions from October 30, 2016, to November 01, 2018.

With the above criteria for the connection graph, 993 unique interferogram pairs were identified by the algorithm. The mean normal baseline was determined to be 47.22%, maximum absolute normal baseline was 168.49%, and the minimum absolute baseline was 0.39%. The mean absolute temporal baseline was found to be approximately 22.74 days. The maximum temporal baseline was determined to be 120 days, and minimum 6 days. The 30th image acquired on March 31, 2019, was selected as the super master SLC images.

7. SBAS TIME-SERIES ANALYSIS FOR THE Oʻahu CASE STUDY

The Oʻahu datasets include Sentinel-1 descending and ascending SBAS results for the Waiʻōmaʻo Landslide in Pālolo Valley. Attempts to conduct SBAS analysis with ALOS-1 PALSAR-1 SLC images were not successful due to limited sampling for Oʻahu. Sections 7.1.1 and 7.1.2 provide a brief outline of the SBAS processing results for the descending and ascending datasets, respectively. Section 7.2 compares the SBAS results with those from inclinometer data. Inclinometer data are available as a public record through the Honolulu City and County's Department of Design and Construction website.

7.1. *Oʻahu SBAS Sentinel-1 Descending Results*

The Sentinel-1 descending SBAS results are available from November 28, 2015, to December 14, 2021. A data gap exists between October 23, 2016, and November 6, 2018. The SBAS results presented in Figure 28 below consist of a total of 109,885 points collected along the Honolulu area of Oʻahu.

The color symbology represents the velocity in millimeters per year (mm/year) for each point. Velocity measurements represent movement either away from the satellite (negative) or toward the satellite (positive). Values shown in teal represent areas where no velocity was recorded. The Jenks optimization method was used to group ranges of velocity in natural breaks. The extreme negative and positive velocities of the dataset in the velocity key are -41.03 mm/year and +24.91 mm/year, respectively.

The area of the Waiʻōmaʻo Landslide is annotated in Figure 28. The results demonstrate that the urban center of the Oʻahu south shore is well captured by Sentinel-1. However, the mountainous and heavily vegetated areas of the Koʻolau range show significantly less SBAS point coverage that meet the criteria outlined in the SARscape processing steps. The low SBAS point coverage can be attributed to both topography and vegetation. The amount of vegetation is likely the primary contributor to signal loss. The C-band (5.6 cm) Sentinel-1 wavelengths are easily scattered by the heavily vegetated areas of the Koʻolau range and the radar return is significantly less than from the more developed areas. A lower signal return lowers the coherence. Datapoints that do not meet the coherence threshold are deleted by in the SBAS algorithm.

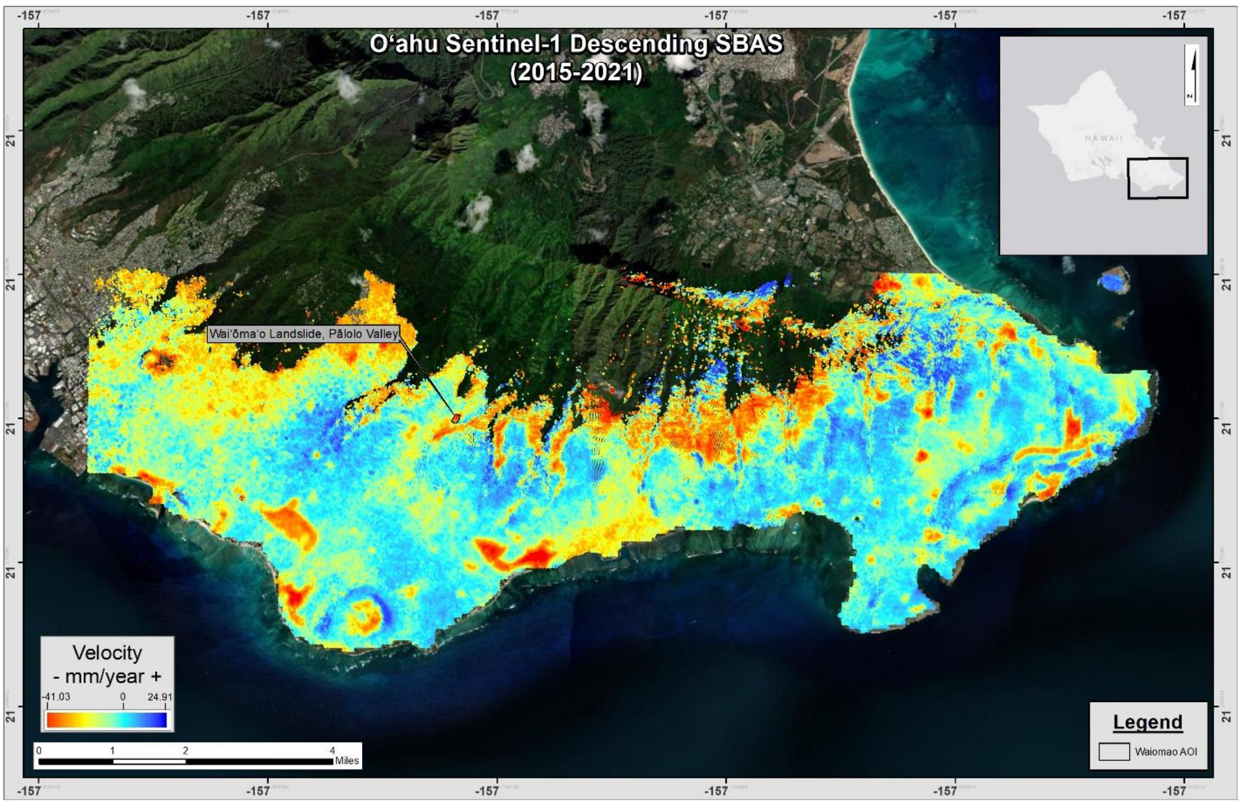

Figure 28 Sentinel-1 descending SBAS results

7.2. *Oʻahu SBAS Sentinel-1 Ascending Results*

The Sentinel-1 ascending SBAS results captured displacement measurements from October 28, 2018, to December 11, 2021. There were no significant data gaps within the time-series displacement measurements of the dataset. The SBAS results presented in Figure 29 consists of a total of 481,603 points collected along the south shore of O‘ahu.

The extreme negative and positive velocities of the dataset are -13.02 mm/year and +3.64 mm/year, respectively. The area of the Wai‘ōma‘o Landslide is annotated in Figure 29.

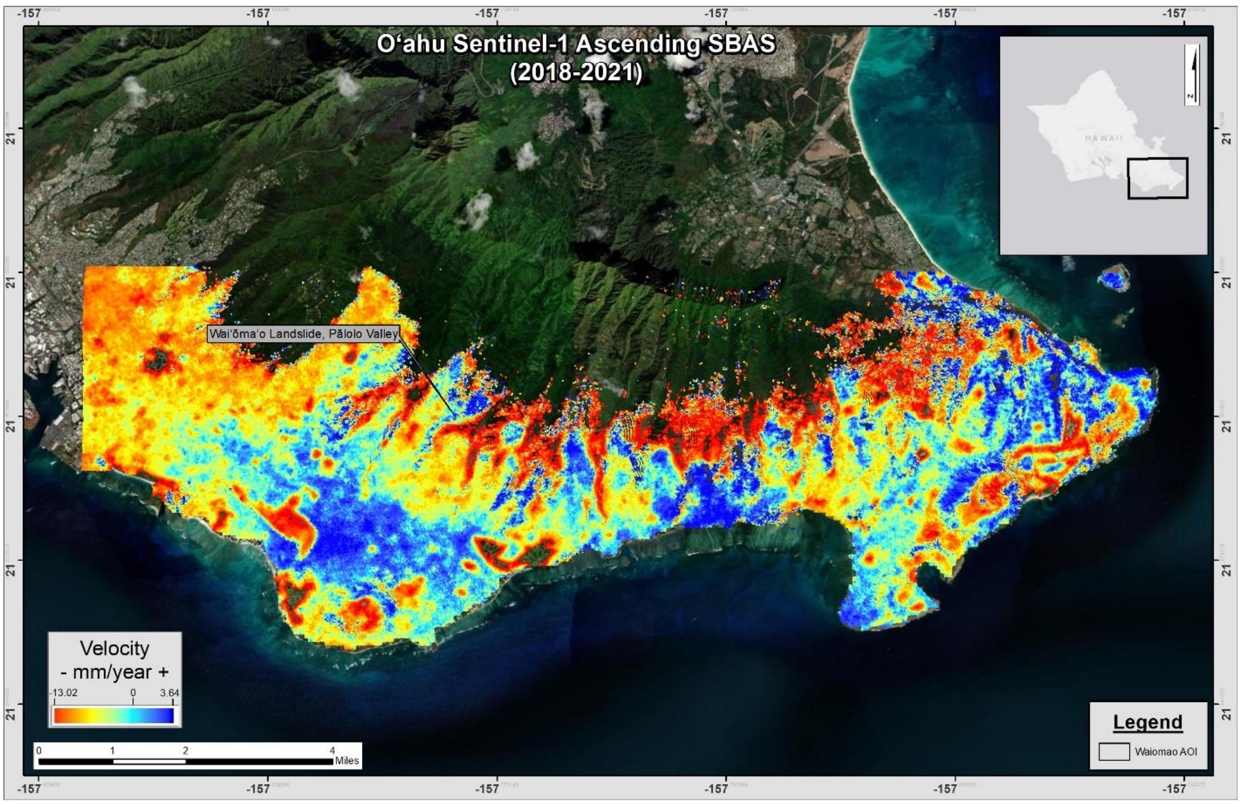

Figure 29 Sentinel-1 ascending SBAS results

7.3. *Review of Available Inclinometer Data with Descending Time-Series Analysis Results*

Problems associated with the Wai‘ōma‘o Landslide in Pālolo Valley were initially noted in 1954 (Peck, 1959). Currently, there are remediation efforts to arrest the land sliding by the City and County of Honolulu at parcels that they acquired. Led by the Department of Design and Construction, the project is known as the *Kuahea Street Area Stabilization Project* (C&C Honolulu

2022). These efforts that are planned or are underway include: drainage systems repair and installation; installation of tieback anchoring systems; installation of a soldier pile wall; regrading and reconstruction of public roadways; and excavation and regrading of landslide debris areas (C&C Honolulu 2022).

Beginning in 1999, the City and County of Honolulu implemented a monitoring program for the area. Monitoring reports from a local geotechnical engineering firm are publicly available through the City's *Docushare database* located on the *Municipal Reference Center* webpage (C&C Honolulu 2022). Monitoring reports have been prepared on a yearly or bi-yearly basis starting in 2000 and there are currently 33 reports available to the public (C&C Honolulu 2022). Several inclinometers have been installed in the neighborhood at different points in time. Inclinometers installed early in the monitoring program consisted of traditional pipe casing inclinometers that require manual field monitoring (Geolabs 2021). Recently, in-situ Shape Acceleration Array (SAA) type inclinometers have been installed in place of the traditional inclinometers that have become non-functional due to extreme deformation of the inclinometer pipe casing (Geolabs 2021). The reports also include monthly average rainfall from in-place rain gauges installed at the city acquired parcels and visual observations of the neighborhood conditions (Geolabs 2021).

This section compares the inclinometer data with the SBAS time-series analysis results of points located nearest to each corresponding inclinometer. The annotated Area A, Area B, "Waiʻōmaʻo Landslide", and Area C in Figure 31 are consistent with the areas noted in the monitoring reports (Geolabs 2021).

To provide a consistent comparison of inclinometer readings with SBAS results, SBAS line-of-site displacements were decomposed into vertical and horizontal (East) vector components by combining the line-of-sight measurements from the descending and ascending datasets to determine the true vertical and east facing horizontal measurements. Figure 30 shows the geometric configuration of the ascending and descending satellites in relation to the point of interest for decomposition.

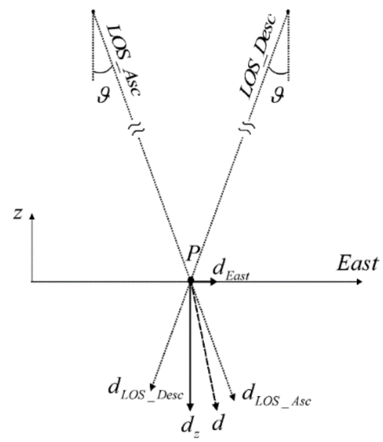

Figure 30 Geometric configuration of satellites for decomposition (Manzo et. al, 2006).

The "true" east component of displacement was obtained using an incidence angle of 36.26° in Equation 18 (Manzo et. al, 2006).

$$d_{East} \approx \frac{d_{LOS\_Desc} - d_{LOS\_Asc}/2}{\sin(\vartheta)} \qquad (18)$$

The vertical component of deformation can be similarly obtained using Equation 19 (Manzo et. al., 2006).

$$d_Z \approx \frac{d_{LOS\_Desc} - d_{LOS\_Asc}/2}{\cos(\vartheta)} \qquad (19)$$

For this report, only the horizontal component is needed for comparison with inclinometer results.

The east component of horizontal displacement was then adjusted to match the direction of movement recorded by the inclinometer by dividing the east component by the cosine of the adjusted angle from LOS. Table 6 provides a list of inclinometers with the corresponding SBAS points and the angle of adjustment between east and the true direction of movement.

Table 6 Inclinomter direction of displacement and adjusted angles for SBAS points

Inclinometer	True direction of displacement (°)	SBAS Point #	Adjusted angle (°) [from line-of-site]
I-20	318	1	132
I-5 and I-5R (SAA)	333	2	117
I-24	299	3	151
I-36 and I-36R (SAA)	314	4	136
I-38 (SAA) and I-38R (SAA)	322	5	128
I-37 (SAA) and I-37R (SAA)	314	6	136
I-35 (SAA), I-35R (SAA), I-35RR (SAA), and I-35RRR (SAA)	314	7	136
I-33	304	8	146
I-33 and I-41 (SAA)	304	9	146
I-34	328	10	122
I-40	323	11	127
I-31	322	12	128
I-30	321	13	129
I-29 (SAA)	318	14	132
I-42 (SAA)	339	15	111
I-39	339	16	111
I-7	298	17	152

A review of the average velocity, coherence, and vertical and horizontal precision is provided for each SBAS point. Generally, SBAS points having acceptable coherence, and precision values that are lower than the displacement measurements can be considered valid.

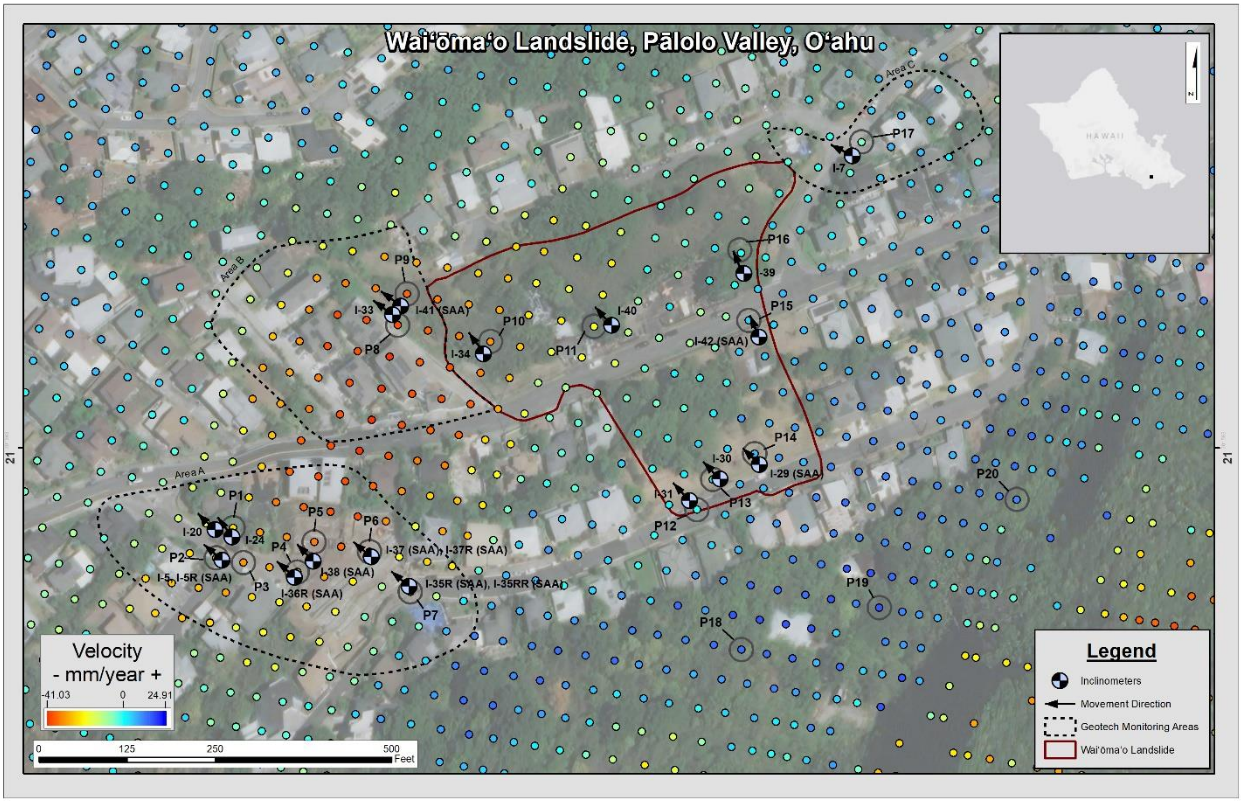

Figure 31 Inclinometer data ploted with SBAS time-series results

7.3.1. Inclinometer I-20 and SBAS measurements for Point 1

Time-series displacement measurements for Point 1 are plotted with the inclinometer readings collected for Inclinometer I-20 in Figure 32. The SBAS dataset consists of points collected from November 6, 2018, to December 14, 2021. The time overlap with inclinometer data is from November 6, 2018, to July 1, 2020, approximately 1 year and 8 months. Geolabs (2021) provided inclinometer data on a yearly basis starting from October 2006. Inclinometer I-20 was installed to a depth of 63 feet (Geolabs 2021). Geolabs (2021) identified a "well-defined basal slip surface" at approximately 19 to 21 feet below ground surface. The rate of movement for I-20 was generally consistent. However, readings collected on June 30, 2020, indicate that movement had accelerated.

SBAS measurements collected for the area of I-20 are consistent with the last two inclinometer readings where there is data overlap.

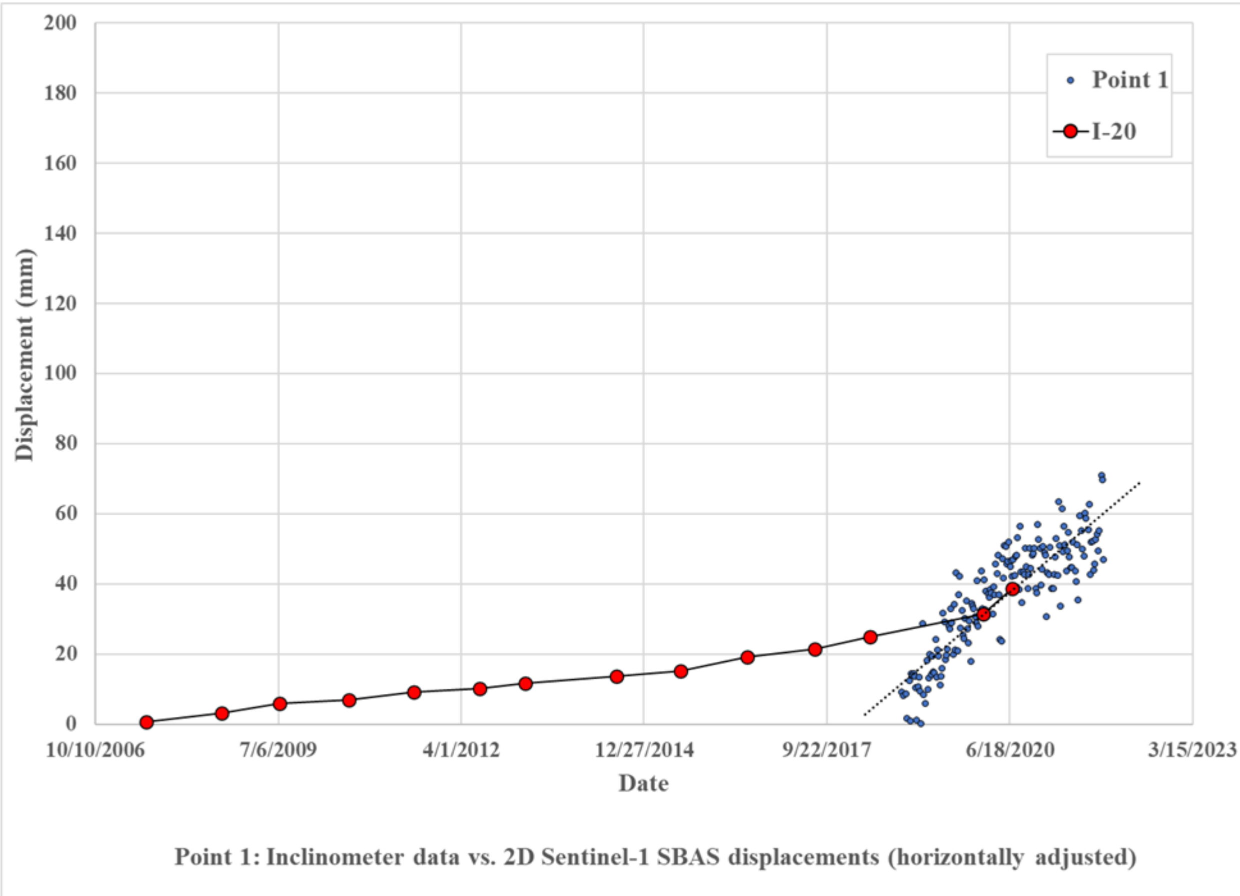

Figure 32 Inclinometer I-20 plotted with Point 1 displacement time-series

7.3.2. Inclinometers I-5 and I-5R (SAA) and SBAS measurements for Point 2

Time-series displacement measurements for Point 2 are plotted with the inclinometer readings collected for inclinometers I-5 and I-5R (SAA) in Figure 33. I-5R (SAA) was installed on June 23, 2019, to replace I-5 (Geolabs 2021). The SBAS dataset consists of points collected from November 6, 2018, to December 14, 2021. Inclinometer readings for I-5 did not overlap with the SBAS dataset but datapoints for I-5R do for approximately 1 year. Geolabs (2021) provided data for

Inclinometer I-5 on a yearly basis starting in late 1999. Inclinometer data collected prior to October 2006 are not shown to maintain consistency of the y-axis in all the inclinometer vs. SBAS displacement plots. Inclinometer I-5 was installed to a depth of 92 feet (Geolabs 2021). It identified a “well-defined basal slip surface” at approximately 13 to 15 feet below ground surface (Geolabs 2021). I-5R (SAA) was installed to 53 feet below ground surface (Geolabs 2021). The slip surface at I-5R is consistent with that at I-5 (Geolabs 2021).

The movement trend in Inclinometer I-5 is generally constant through most of the monitoring period except movements appear to have accelerated in July 2017. The trend of readings collected from I-5R (SAA) is consistent with the later trend of I-5 as well as with the SBAS measurements.

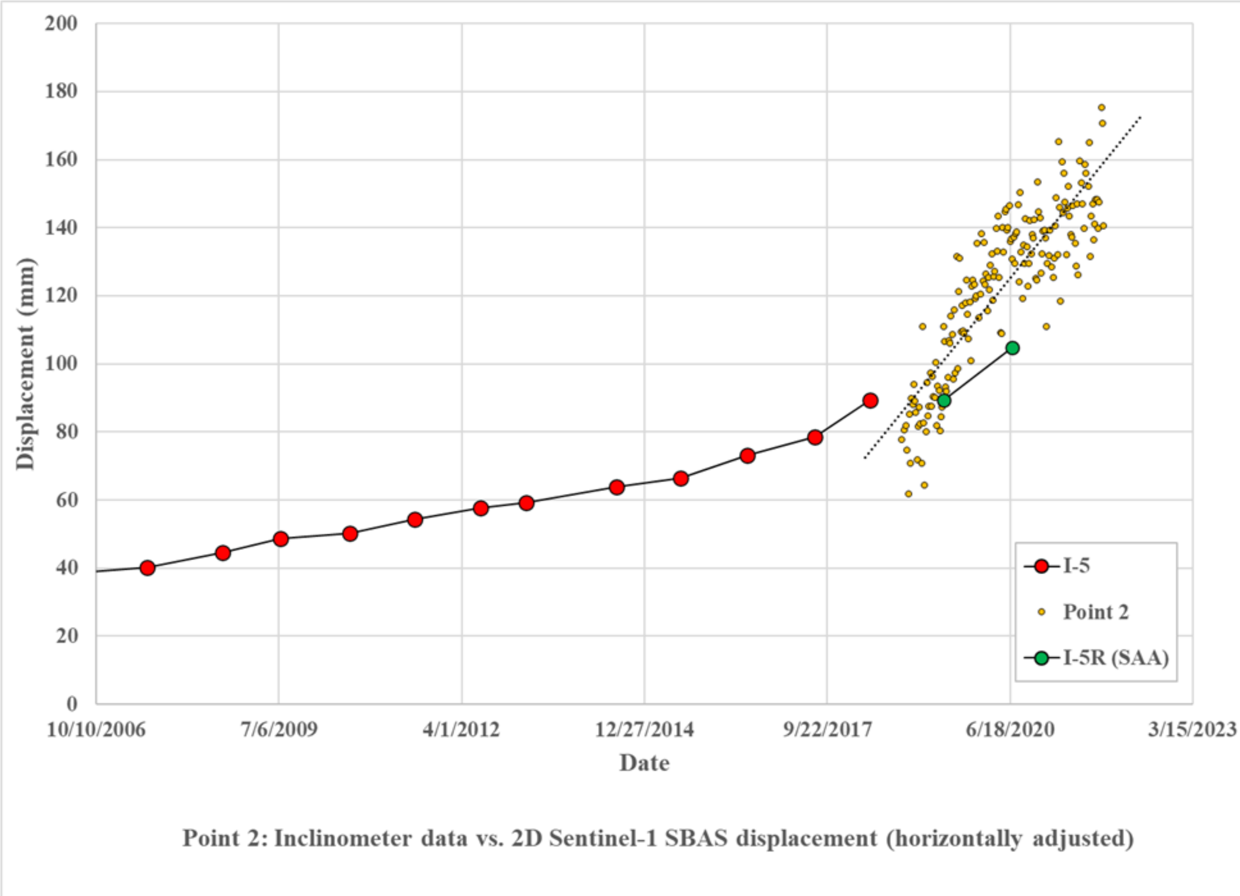

Figure 33 Inclinometers I-5 and I-5R (SAA) plotted with Point 2 displacement time-series

7.3.3. Inclinometer I-24 and SBAS measurements for Point 3

Time-series displacement measurements for Point 3 are plotted with the inclinometer readings collected for Inclinometer I-24 in Figure 34. SBAS points were collected from November 6, 2018, to December 14, 2021, overlapping with the inclinometer data from November 6, 2018, to June 30, 2020. The overlap period is approximately 1 year and 8 months. Inclinometer data are available on a yearly basis starting from August 2008 (Geolabs 2021). The inclinometer I-24 was installed to a depth of 57 feet (Geolabs 2021). Geolabs (2021) reported a basal slip surface at approximately 19 to 25 feet below ground surface. The trend of inclinometer movement is generally consistent through most of the monitoring period. However around June 30, 2020, the movement accelerated. SBAS measurements are consistent with the inclinometer readings.

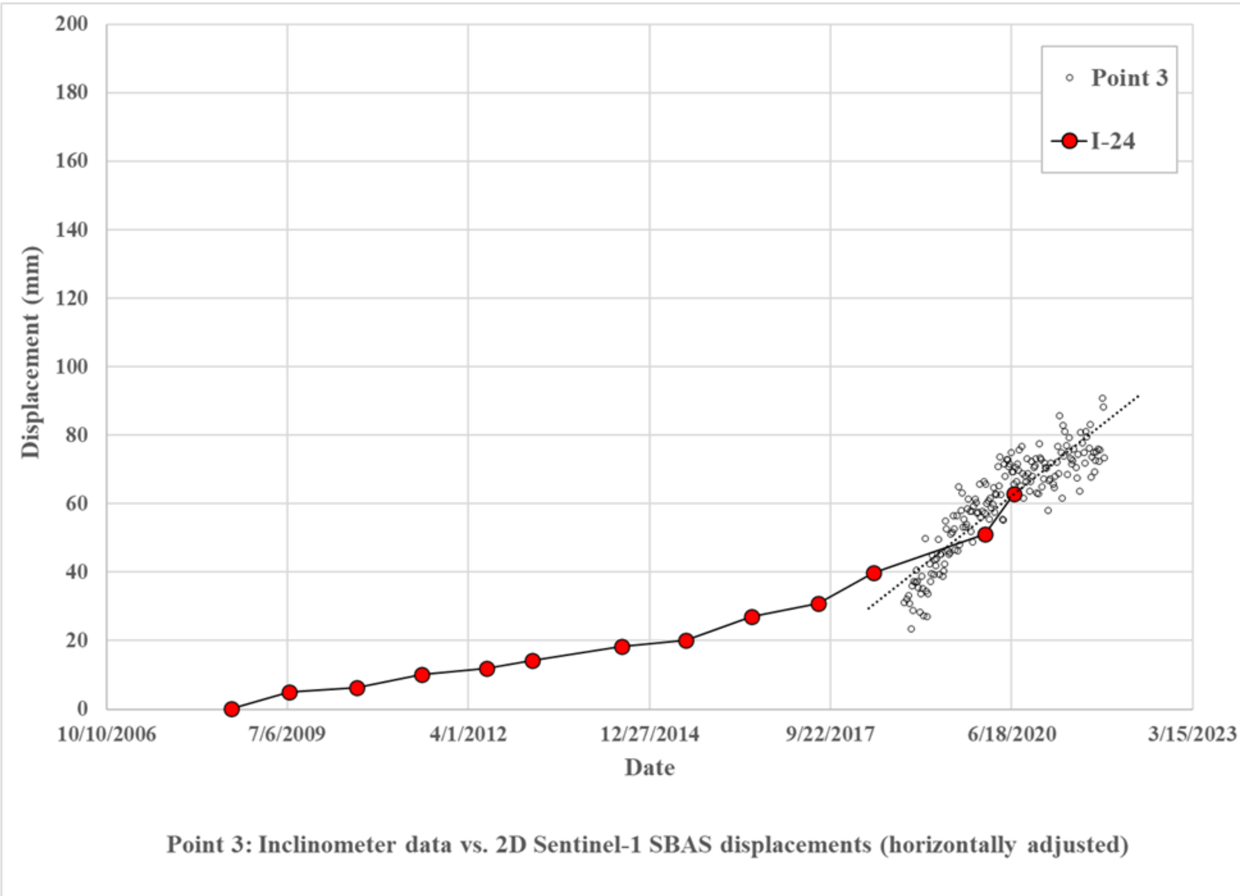

Figure 34 Inclinometer I-24 plotted with Point 3 displacement time-series

7.3.4. Inclinometers I-36 and I-36R (SAA) and SBAS measurements for Point 4

Time-series displacement measurements for Point 4 are plotted with inclinometer I-36 and I-36R (SAA) readings in Figure 35. SBAS points were collected from November 6, 2018, to December 14, 2021. Inclinometer readings for I-36 do not overlap with the SBAS dataset but the I-36R (SAA) datapoints do overlap from May 26, 2019, through June 30, 2020. The period of overlap is approximately 1 year and 1 month. Geolabs (2021) reported Inclinometer I-36 data on a yearly basis starting from July 11, 2016, to May 16, 2018. Inclinometer I-36 was installed to a depth of 67 feet (Geolabs 2021). A "well-defined basal slip surface" was reported at approximately 13 to 17 feet below ground surface (Geolabs 2021).

I-36R (SAA) was installed on May 29, 2019, to replace I-36 (Geolabs 2021). I-36R (SAA) was installed to a depth of 52 feet below ground surface (Geolabs 2021). The slip surface at the location is described in the monitoring report as a "sharp basal slip surface" at a depth between 15.5 and 17.5 feet (Geolabs 2021).

Displacement rates at Inclinometer I-36 are significantly greater than those for inclinometers I-20, I-5, and I-24. The corresponding SBAS measurements are not consistent with the inclinometer readings.

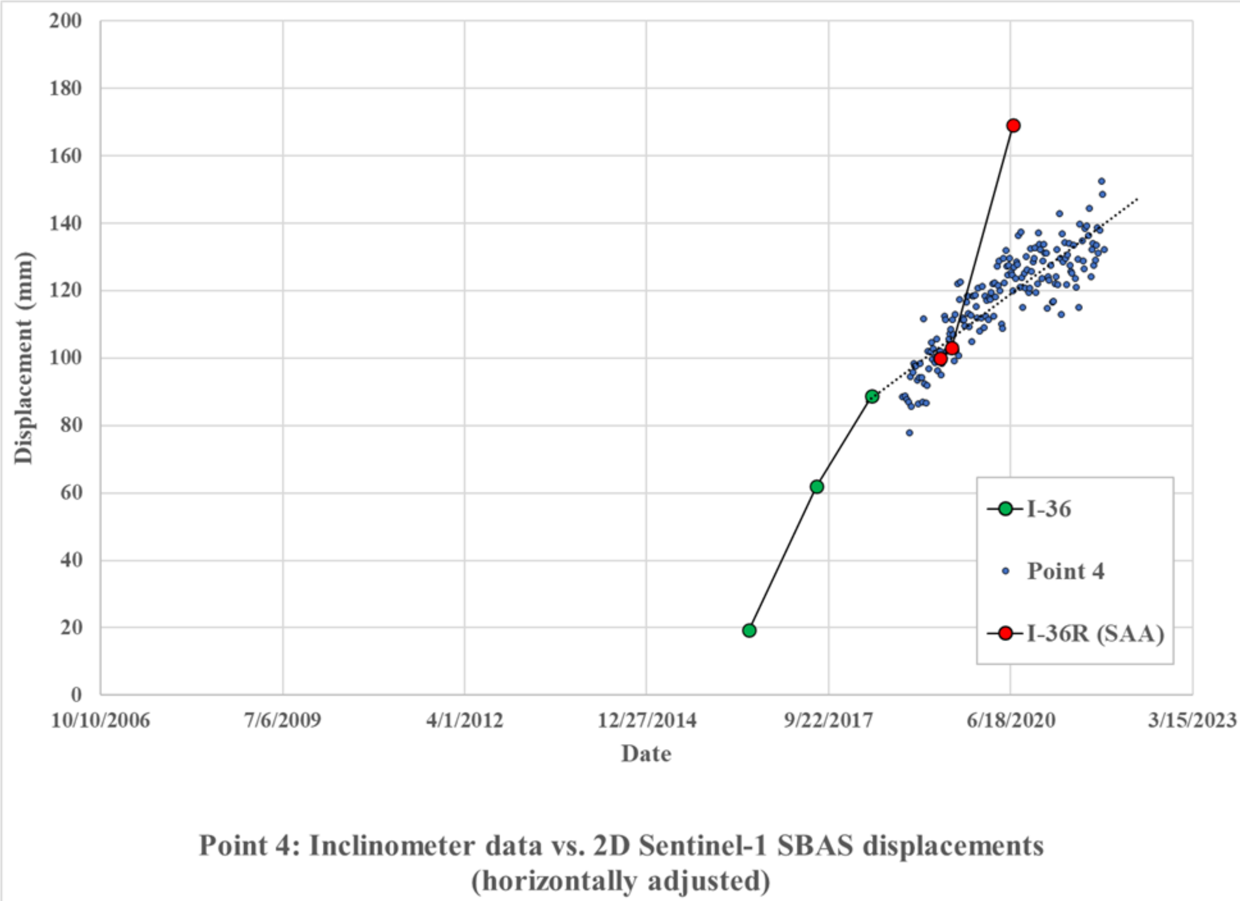

Figure 35 Inclinometers I-36 and I-36R (SAA) plotted with Point 4 displacement time-series

7.3.5. Inclinometers I-38 (SAA) and I-38R (SAA) and SBAS measurements for Point 5

Time-series displacement measurements for Point 5 are plotted with the inclinometer readings collected for inclinometers I-38 (SAA) and I-38R (SAA) in Figure 36. SBAS points were collected from November 6, 2018, to December 14, 2021. Inclinometer readings for I-38 (SAA) overlap with the SBAS dataset from April 11, 2019, to March 17, 2020. Datapoints for I-38R (SAA) overlap within the SBAS time-series displacements from April 22, 2020, to July 15, 2020, approximately 1 year and 3 months. Inclinometer I-38 (SAA) was installed to a depth of 52 feet (Geolabs 2021). Geolabs (2021) reported a “sharp basal slip surface” at approximately 13 to 17 feet below ground surface.

I-38R (SAA) was installed on April 22, 2020, to replace I-38 (SAA) after it stopped functioning to a depth of 46.5 feet below ground surface (Geolabs 2021). The slip surface at the location is not described in the report.

The displacement rates for I-38 (SAA) decreased between September 26, 2019, to November 22, 2019, but accelerated from November 22, 2019, till the inclinometer ceased to function on March 17, 2020.

The replacement, I-38R (SAA) showed continuous accelerated displacements from April 22, 2020, to May 15, 2020. Readings from May 15, 2020, to July 15, 2020, indicate that the displacements had slowed. SBAS measurements collected are not consistent with the inclinometer readings.

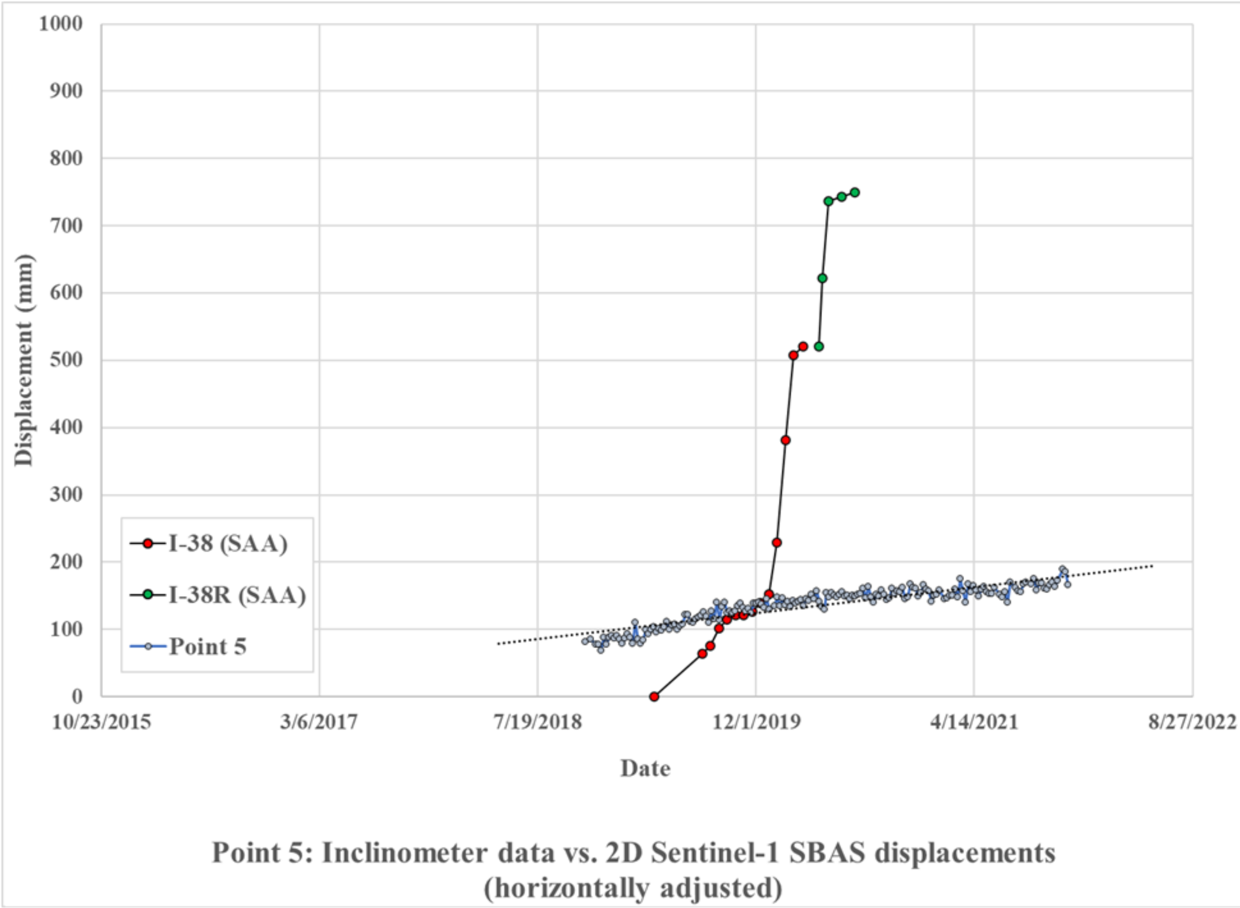

Figure 36 Inclinometers I-38 (SAA) and I-38R (SAA) plotted with Point 5 displacement time-series

7.3.6. Inclinometers I-37 (SAA) and I-37R (SAA) and SBAS measurements for Point 6

Time-series displacement measurements for Point 6 are plotted with the inclinometer readings collected for inclinometers I-37 (SAA) and I-37R (SAA) in Figure 37. SBAS points were collected from November 6, 2018, to December 14, 2021. Inclinometer readings for I-37 (SAA) do not overlap with the SBAS dataset. Datapoints for I-37R (SAA) overlap within the SBAS measurements from April 11, 2019, to August 1, 2019, approximately 4 months. Inclinometer I-37 (SAA) was installed to a depth of 52 feet (Geolabs 2021). Geolabs reported a "sharp basal slip surface" at approximately 22.5 to 25 feet below ground surface (Geolabs 2021).

I-37R (SAA) was installed on April 22, 2020, to replace I-37 (SAA) after it stopped functioning on November 1, 2018 (Geolabs 2021). I-37R (SAA) was installed to a depth of 52 feet below ground surface (Geolabs 2021). The slip surface at the location is not described in the monitoring report.

Readings for I-37 (SAA) showed two periods having accelerated movements: one between April 12, 2018, and May 12, 2018, and the other between October 12, 2018, and November 1, 2018. Inclinometer I-37 ceased to function on November 1, 2018. The trend of readings from I-37R (SAA) is consistent with the trend for I-37 (SAA).

SBAS measurements collected for the area of I-37 (SAA) and I-37R (SAA) are not consistent with the inclinometer readings.

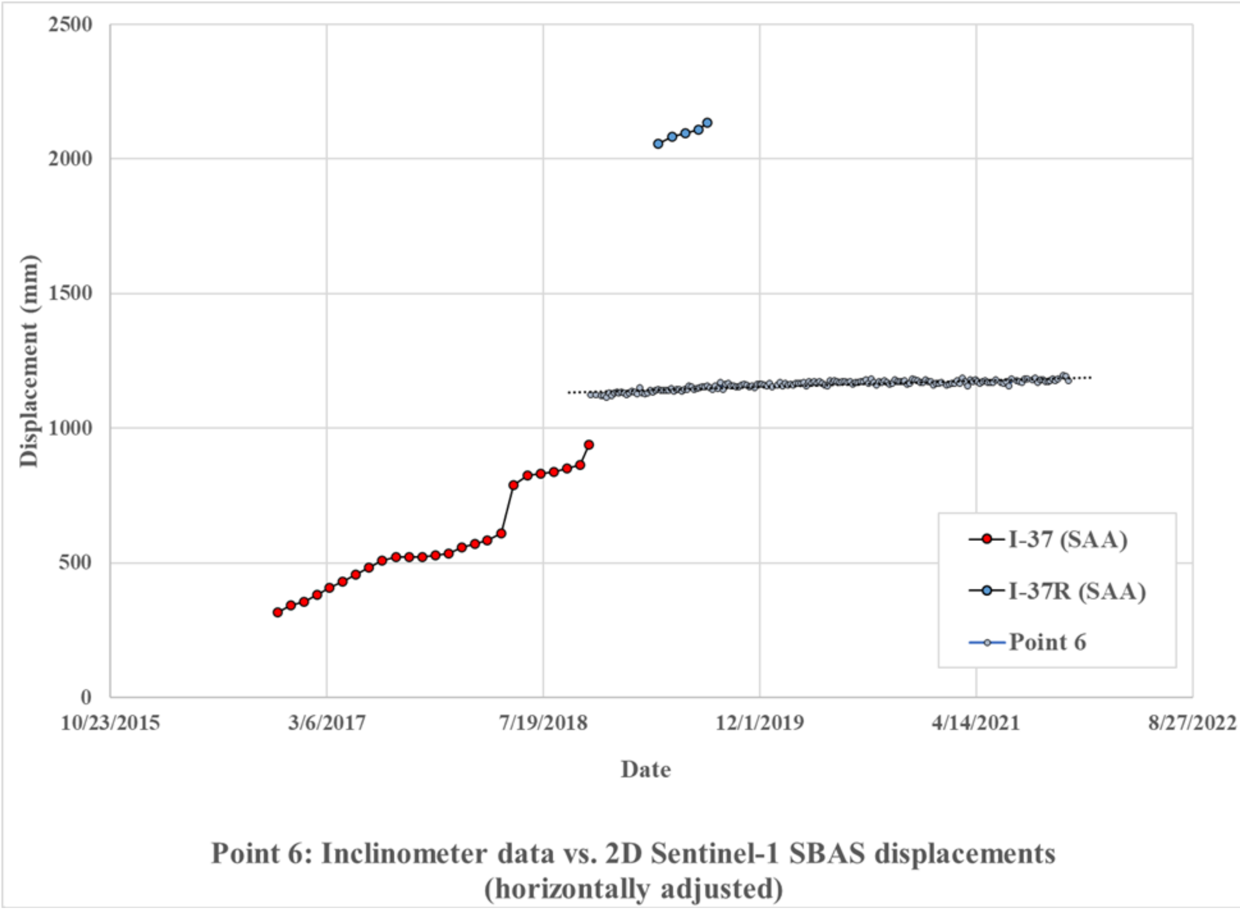

Figure 37 Inclinometers I-37 (SAA) and I-37R (SAA) plotted with Point 6 displacement time-series

7.3.7. Inclinometers I-35 (SAA), I-35R (SAA), I-35RR (SAA), and I-35RRR (SAA) and SBAS measurements for Point 7

Time-series displacement measurements for Point 7 are plotted with the readings for inclinometers I-35 (SAA), I-35R (SAA), I-35RR (SAA), and I-35RRR (SAA) in Figure 38. SBAS points were collected from November 6, 2018, to December 14, 2021. Inclinometer readings for I-35 (SAA) do not overlap with the SBAS dataset. Datapoints for I-35R (SAA) overlap with the SBAS time-series displacement measurements from November 6, 2018, to March 8, 2019, approximately 4 months. Datapoints for I-35RR (SAA) overlap with the SBAS time-series displacement measurements from April 2019 to April 2020, approximately 1 year. Datapoints for

I-35RRR (SAA) overlap within the SBAS time-series displacement measurements from April 2019 to May 2020, approximately 1 month.

Inclinometers I-35R (SAA), I-35RR (SAA) and I-35RRR (SAA) were installed to depths of 52, 52 and 46 ft, respectively (Geolabs 2021). Depth of installation for I-35 (SAA) was not provided.

I-35 (SAA) showed significant displacement rates until September 12, 2017. The displacements stopped between October 12, 2017, and November 1, 2017, shortly before the inclinometer became non-functional.

Readings for I-35R (SAA) were initially consistent with those of I-35 (SAA) but accelerated on October 8, 2018, until it ceased to function in March 2019.

Readings for I-35RR (SAA) were consistent with the slower rate of I-35RR (SAA) until November 2019 when significant acceleration of movement was recorded until it ceased to function in April 2020.

Readings from I-37RRR (SAA) is notably flat compared to the rest of the data.

SBAS measurements collected for the area of I-35 (SAA) through I-35RRR (SAA) are not consistent with the inclinometer readings.

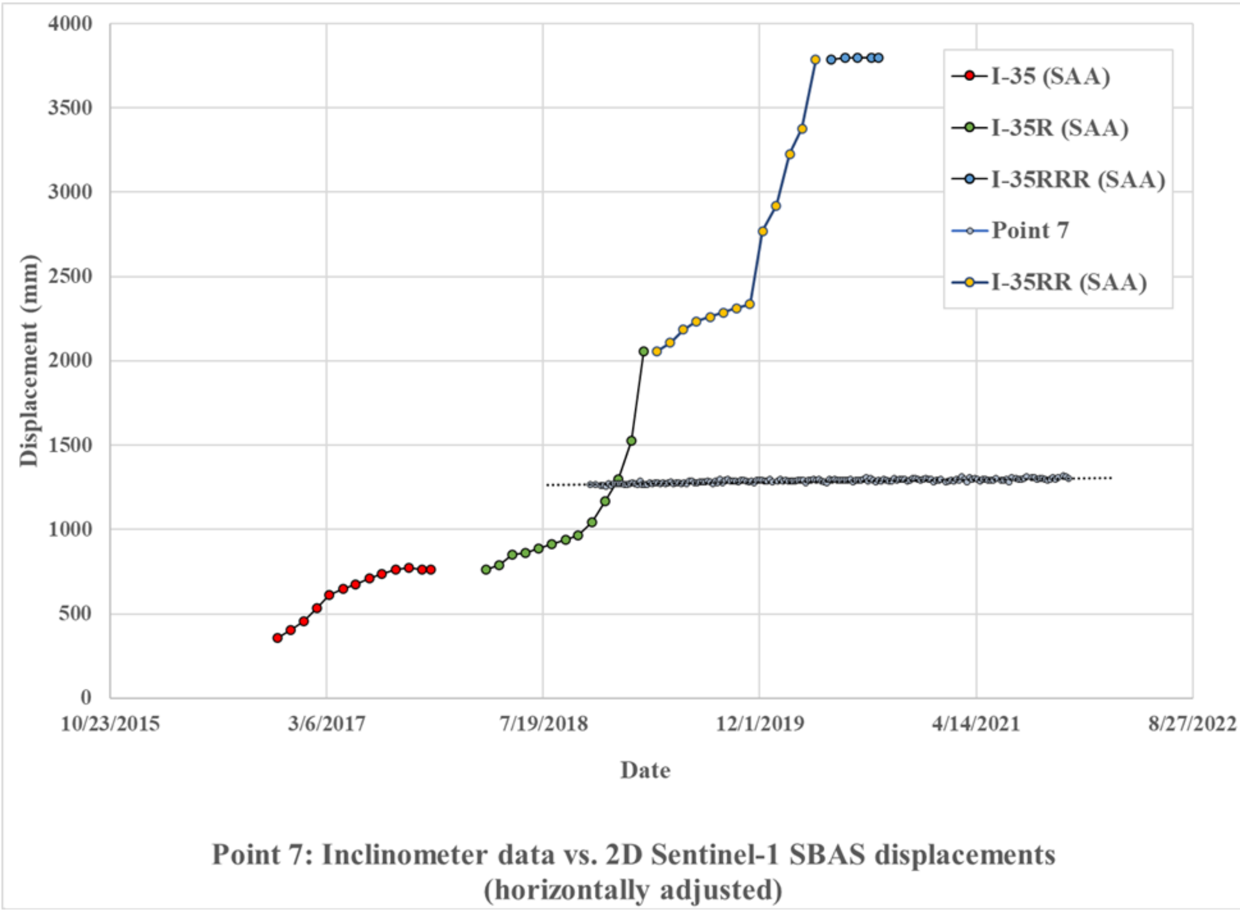

Figure 38 Inclinometers I-35R (SAA), I-35RR (SAA), and I-35RRR (SAA) plotted with Point 7 displacement time-series

7.3.8. Inclinometer I-33 and SBAS measurements for Point 8

Time-series displacement measurements for Point 8 are plotted with the inclinometer readings collected for inclinometer I-33 in Figure 39. The SBAS points were collected from November 6, 2018, to December 14, 2021. The SBAS data does not overlap with the inclinometer data. Inclinometer I-33 data is available from July 2015 through May 2018. Inclinometer I-33 was installed to a depth of 69 feet (Geolabs 2021). The movement trend for I-33 is nearly linear throughout the monitoring period. Although SBAS measurements do not overlap the inclinometer data in time, the trends of I-33 and SBAS measurements are quite agreeable.

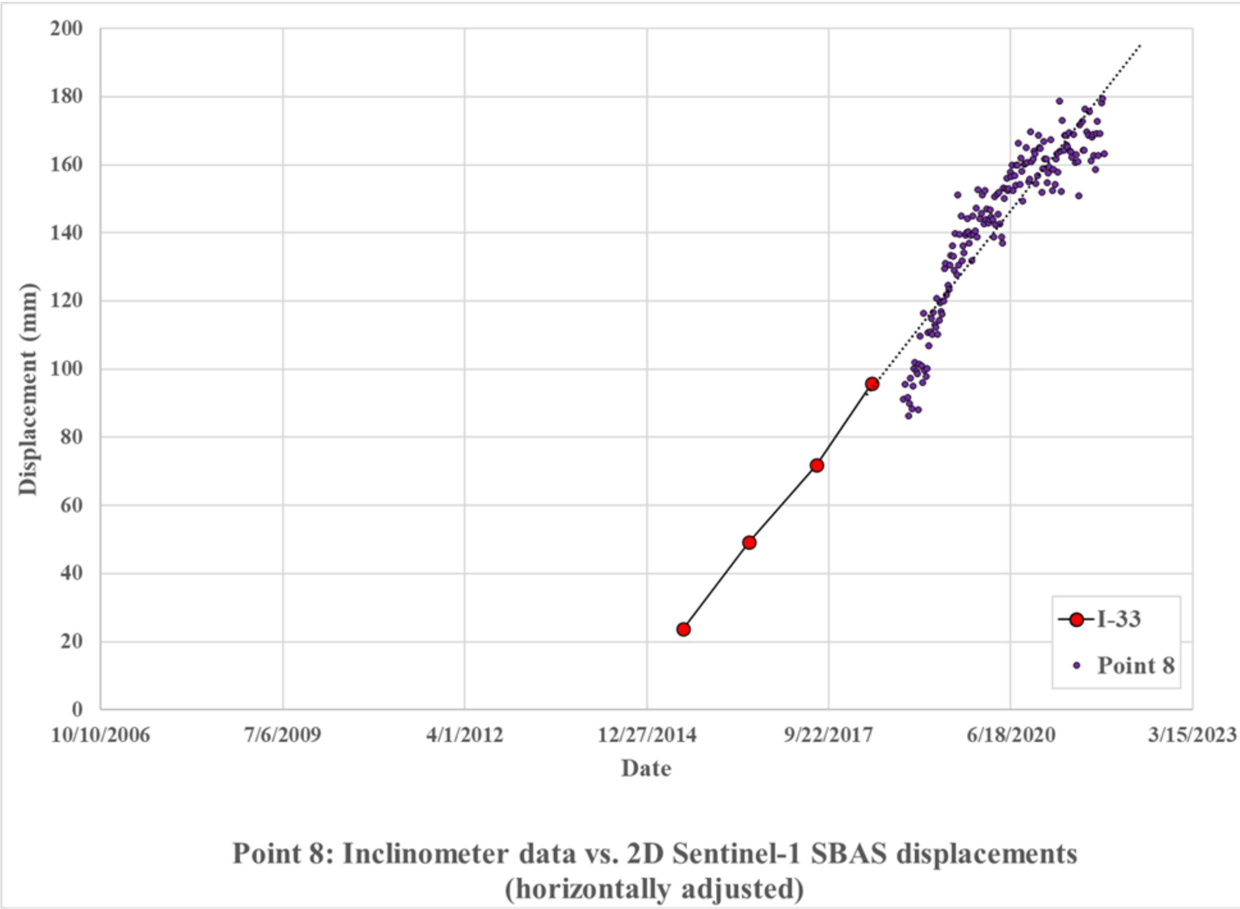

Figure 39 Inclinometer I-33 plotted with Point 8 displacement time-series

7.3.9. Inclinometers I-33 and I-41 (SAA) with SBAS measurements for Point 9

Time-series displacement measurements for Point 9 are plotted with the readings for inclinometers I-33 and I-41 (SAA) in Figure 40. The SBAS dataset was collected from November 6, 2018, to December 14, 2021. The SBAS data do not overlap with the inclinometer data for I-33 but do overlap with I-41 (SAA). Geolabs (2021) collected inclinometer data from July 2015 through May 2018. Readings for I-41 (SAA) were provided from July 2018 to July 2020.

Inclinometer I-33 and I-41 (SAA) were installed to depths of 69 and 35 feet below ground surface, respectively (Geolabs 2021). Geolabs (2021) did not define a basal slip surface for I-33 but does list a “gradual basal slip surface” for I-41 (SAA) at 10 to 12 feet below ground surface.

The trend of movement for I-41 (SAA) and I-33 are quite consistent with SBAS measurements.

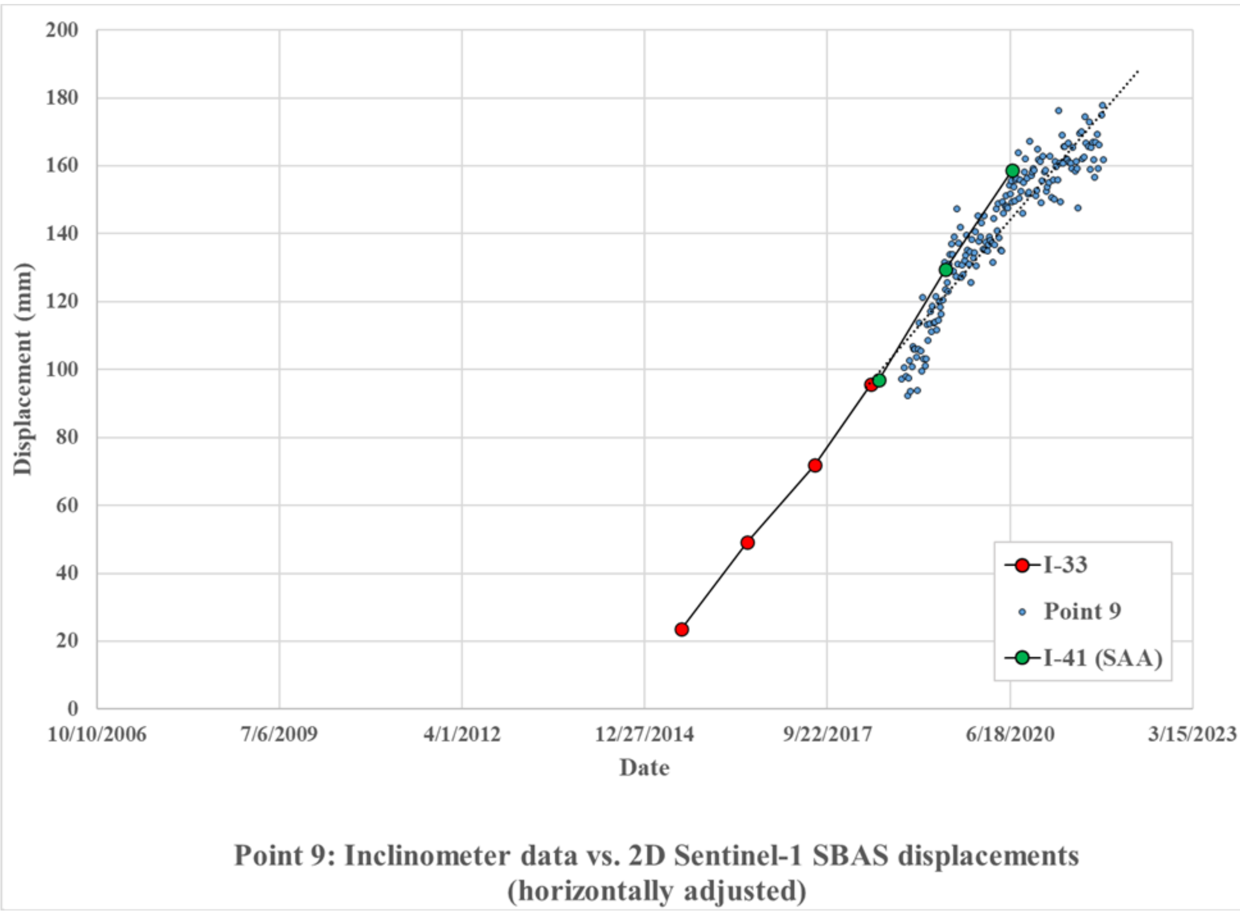

Figure 40 Inclinometers I-33 and I-41 (SAA) plotted with Point 9 displacement time-series

7.3.10. Inclinometer I-34 and SBAS measurements for Point 10

Time-series displacement measurements for Point 10 are plotted with the inclinometer readings for inclinometer I-34 in Figure 41. The SBAS dataset were collected from November 6, 2018, to December 14, 2021. The SBAS data overlaps with the inclinometer data from November

2018 to July 2020. Geolabs (2021) collected inclinometer data starting from July 2015 to July 2020 (Geolabs 2021). Inclinometer I-33 was installed to a depth of 69 feet (Geolabs 2021). Geolabs (2021) reported a "sharp basal slip surfaces" at 13 feet and 17 below ground surface (Geolabs 2021). Movement rates were higher from July 2015 to May 2018 but decreased from May 2018 to January 2020 and then accelerated again from January 2020 to July 2020. The trend of SBAS measurements are not consistent with the trend of the inclinometer readings.

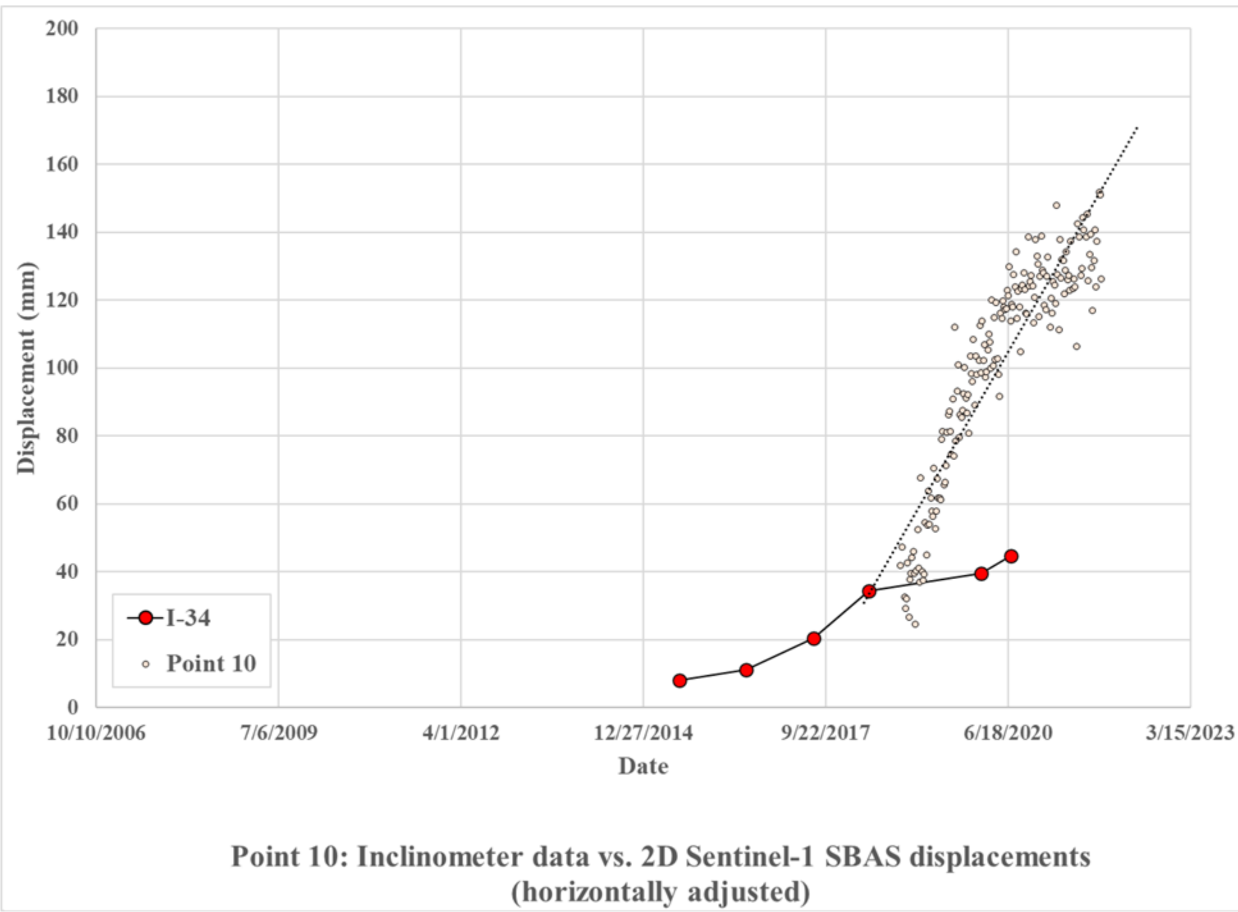

Figure 41 Inclinometer I-34 plotted with Point 10 displacement time-series

7.3.11. Inclinometer I-40 and SBAS measurements for Point 11

Time-series displacement measurements for Point 11 were plotted with the inclinometer readings from inclinometer I-40 in Figure 42. The SBAS dataset were collected from November 6, 2018, to December 14, 2021, and does not overlap with the inclinometer data. Inclinometer readings were collected from July 2016 to May 2018 (Geolabs 2021). Inclinometer I-40 was installed to a depth of 67 feet (Geolabs 2021). A “sharp basal slip surface” was observed between 47 and 49 feet below ground surface at I-40 (Geolabs 2021). Although SBAS measurements do not overlap with the inclinometer data, the trend of inclinometer movement is very consistent with the SBAS measurements.

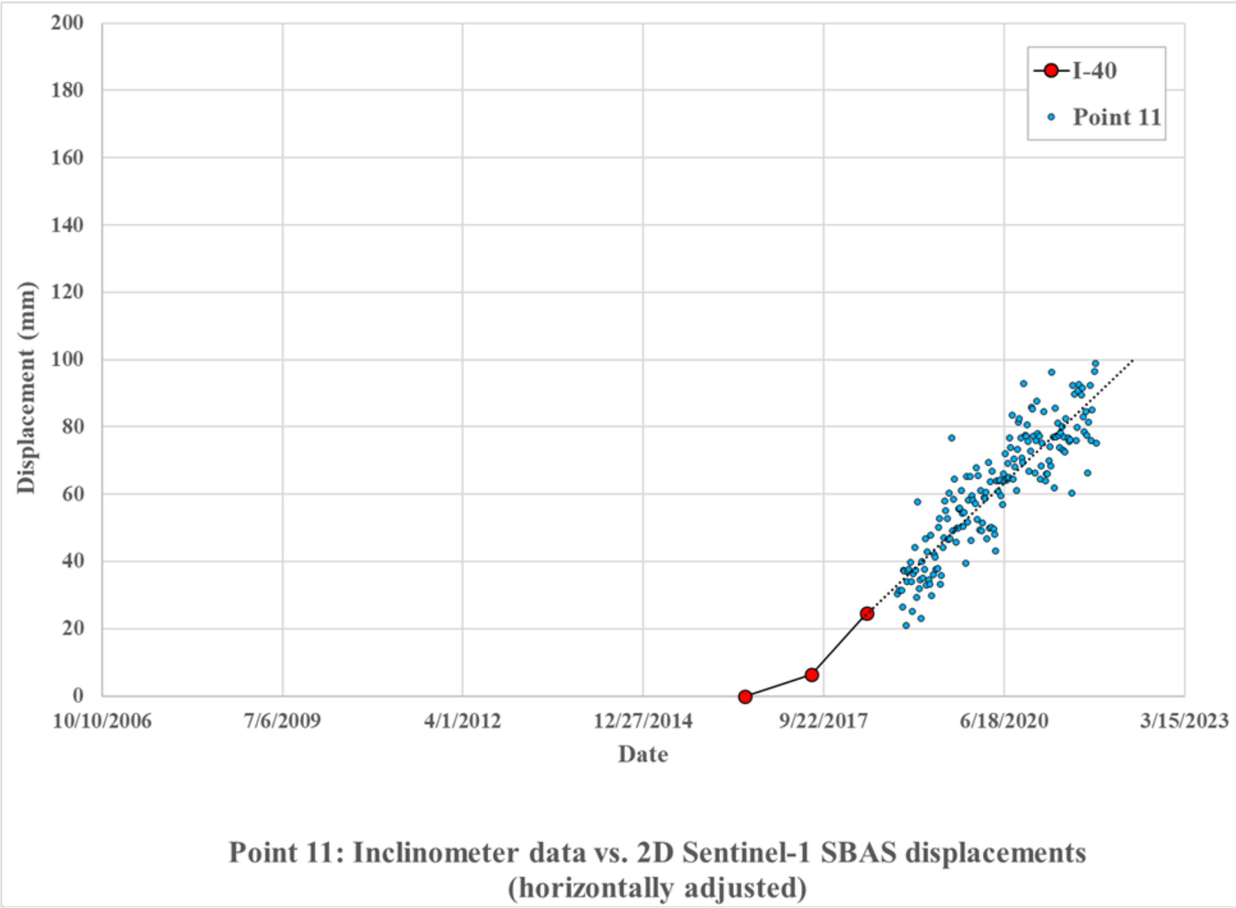

Figure 42 Inclinometer I-40 plotted with Point 11 displacement time-series

7.3.12. Inclinometer I-31 and SBAS measurements for Point 12

Time-series displacement measurements for Point 12 are plotted with the inclinometer readings from Inclinometer I-31 in Figure 43. The SBAS dataset was collected from November 6, 2018, to December 14, 2021. They overlap with inclinometer data from November 2018 to July 2020, approximately 1 year and 9 months. Geolabs (2021) collected readings between July 2010 and July 2020. Inclinometer I-31 was installed to a depth of 93 feet (Geolabs 2021). Geolabs (2021) reported a “sharp basal slip surface” between 20 and 25 feet below ground surface. The displacement velocity was generally consistent throughout the monitoring period; however, readings collected from January 2020 to July 2020 showed a notable increase in displacement rate. Overall, the SBAS results are consistent with the inclinometer readings.

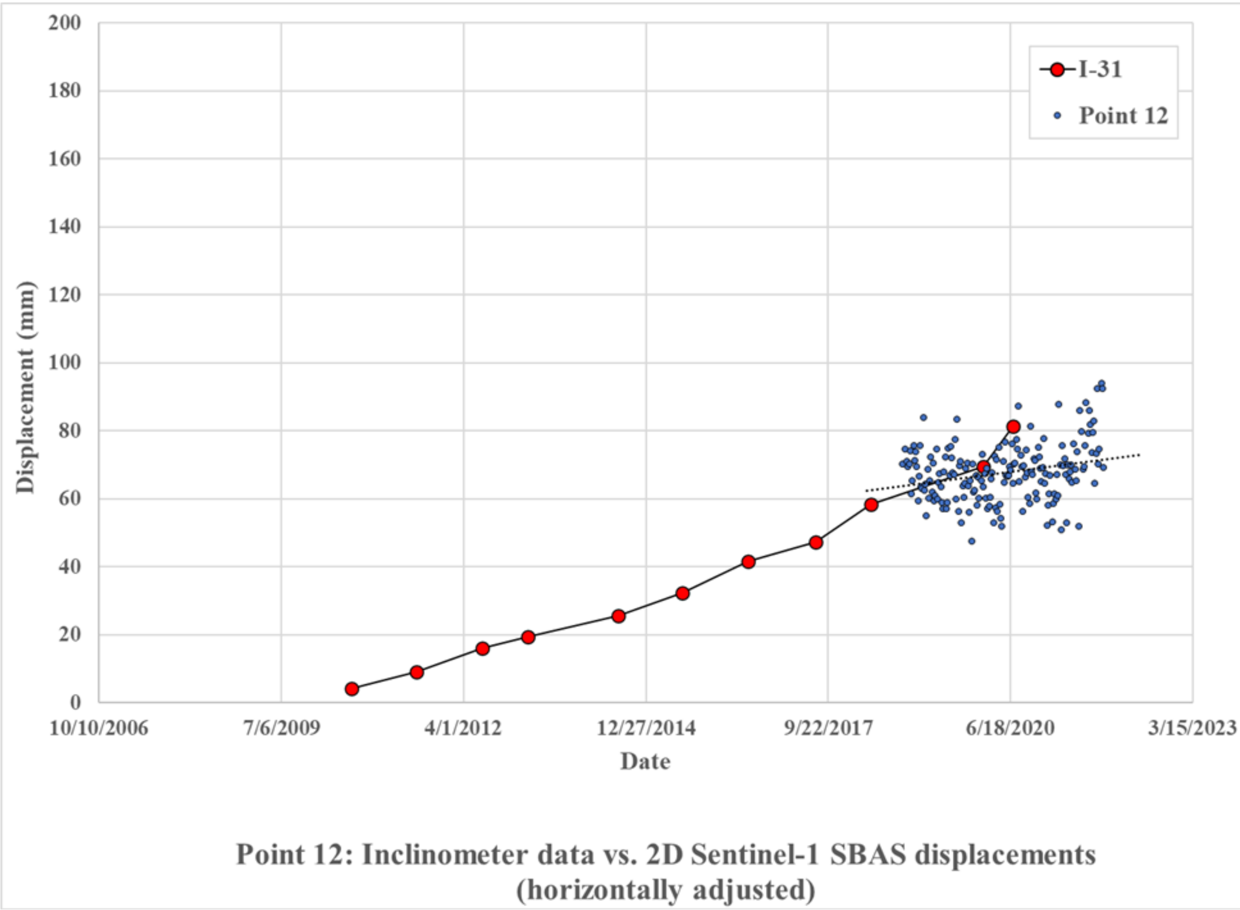

Figure 43 Inclinometer I-31 plotted with Point 12 displacement time-series

7.3.13. Inclinometer I-30 and SBAS measurements for Point 13

Time-series displacement measurements for Point 13 are plotted with the inclinometer readings from inclinometer I-30 in Figure 44. The SBAS dataset was collected from November 6, 2018, to December 14, 2021. It overlaps with inclinometer data from November 2018 to July 2020, approximately 1 year and 9 months. Geolabs (2021) started collecting readings in July 2010 ending in July 2020 (Geolabs 2021). Inclinometer I-30 was installed to a depth of 81 feet (Geolabs 2021).

Geolabs (2021) reported a “primary basal slip surface” between 25 and 35 feet below ground surface (Geolabs 2021). The displacement rate was generally consistent throughout the monitoring period; however, readings collected from January 2020 to July 2020 show a notable increase in velocity. Overall, the SBAS results are consistent with the inclinometer readings.

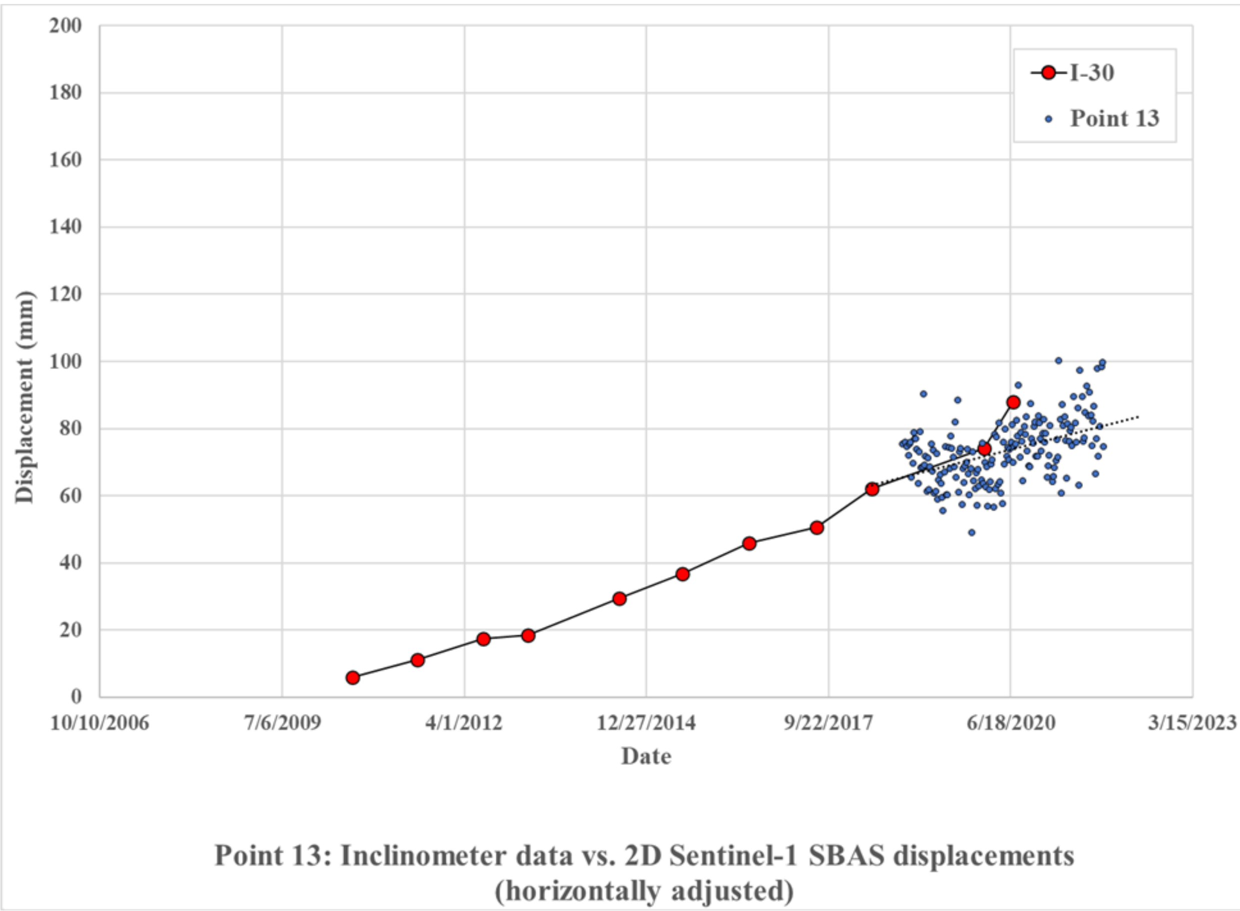

Figure 44 Inclinometer I-30 plotted with Point 13 displacement time-series

7.3.14. Inclinometer I-29 (SAA) and SBAS measurements for Point 14

Time-series displacement measurements for Point 14 are plotted with the inclinometer readings from inclinometer I-29 (SAA) in Figure 45. The SBAS dataset was collected from November 6, 2018, to December 14, 2021. It overlaps with inclinometer data from November 2018 to July 2020. Geolabs (2021) collected inclinometer readings starting in July 2010 and ending in July 2020 (Geolabs 2021). Inclinometer I-29 (SAA) was installed to a depth of 55 feet (Geolabs 2021). Geolabs (2021) reported a "sharp basal slip surface" between 26 and 29 feet below ground surface. The displacement trend was generally consistent throughout the monitoring period; however, readings collected from January 2020 to July 2020 showed a notable increase in displacement rate. Overall, the SBAS results are generally consistent with the inclinometer readings.

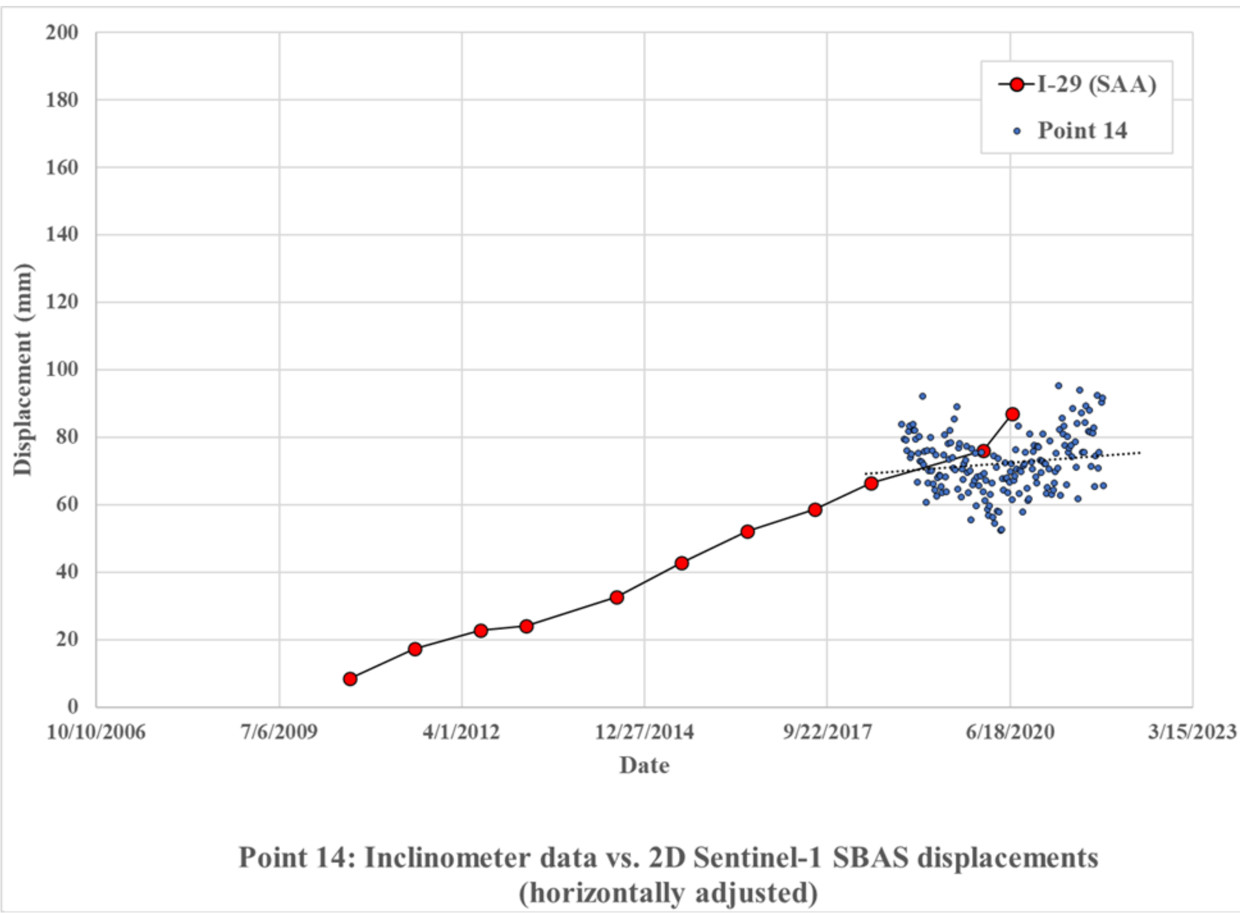

Figure 45 Inclinometer I-29 (SAA) plotted with Point 14 displacement time-series

7.3.15. Inclinometer I-42 (SAA) and SBAS measurements for Point 15

Time-series displacement measurements for Point 15 are plotted with the inclinometer readings from inclinometer I-42 (SAA) in Figure 46. The SBAS dataset was collected from November 6, 2018, to December 14, 2021. It overlaps with the inclinometer data from November 2018 to July 2020. Geolabs (2021) collected inclinometer readings from July 2018 to July 2020 (Geolabs 2021). Inclinometer I-42 (SAA) was installed to a depth of 55 feet (Geolabs 2021). Geolabs (2021) reported a "sharp basal slip surface" between 23 and 27 feet below ground surface. SBAS measurements for the area are generally consistent with the trend of inclinometer data.

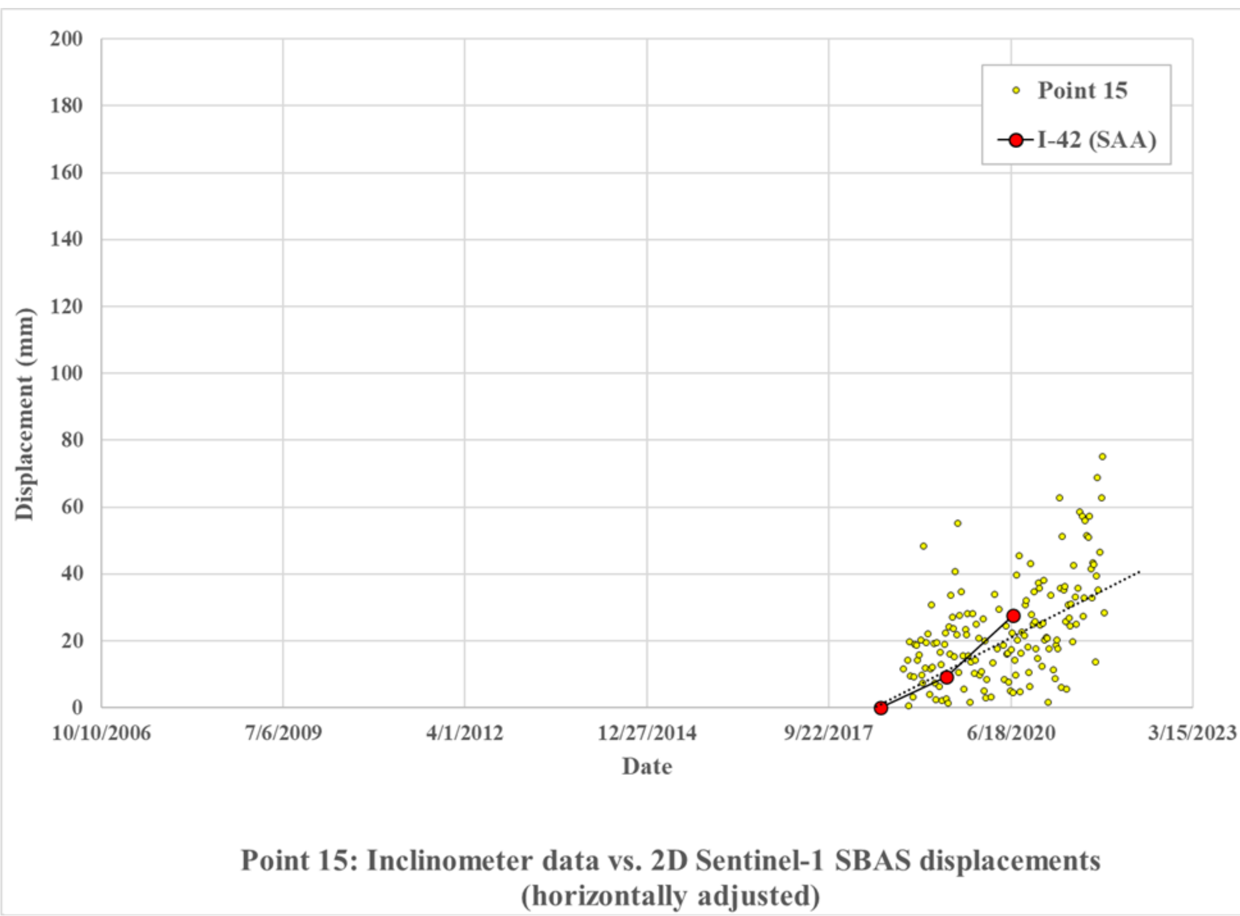

Figure 46 Inclinometer I-42 (SAA) plotted with Point 15 displacement time-series

7.3.16. Inclinometer I-39 and SBAS measurements for Point 16

Time-series displacement measurements for Point 16 are plotted with the inclinometer readings from inclinometer I-39 in Figure 47. The SBAS dataset was collected from November 6, 2018, to December 14, 2021. It overlaps with inclinometer data from November 2018 to July 2020. Geolabs (2021) collected inclinometer readings from July 2016 to July 2020. Inclinometer I-39 was installed to a depth of 69 feet (Geolabs 2021). Geolabs (2021) reported a “sharp basal slip surface” between 41 and 45 feet below ground surface. The trend for displacement at I-39 is generally consistent throughout the monitoring period; however, readings collected from January 2020 to July 2020 showed a notable increase in displacement rate. SBAS measurements from the area are generally consistent with inclinometer data from May 2018 to January 2020.

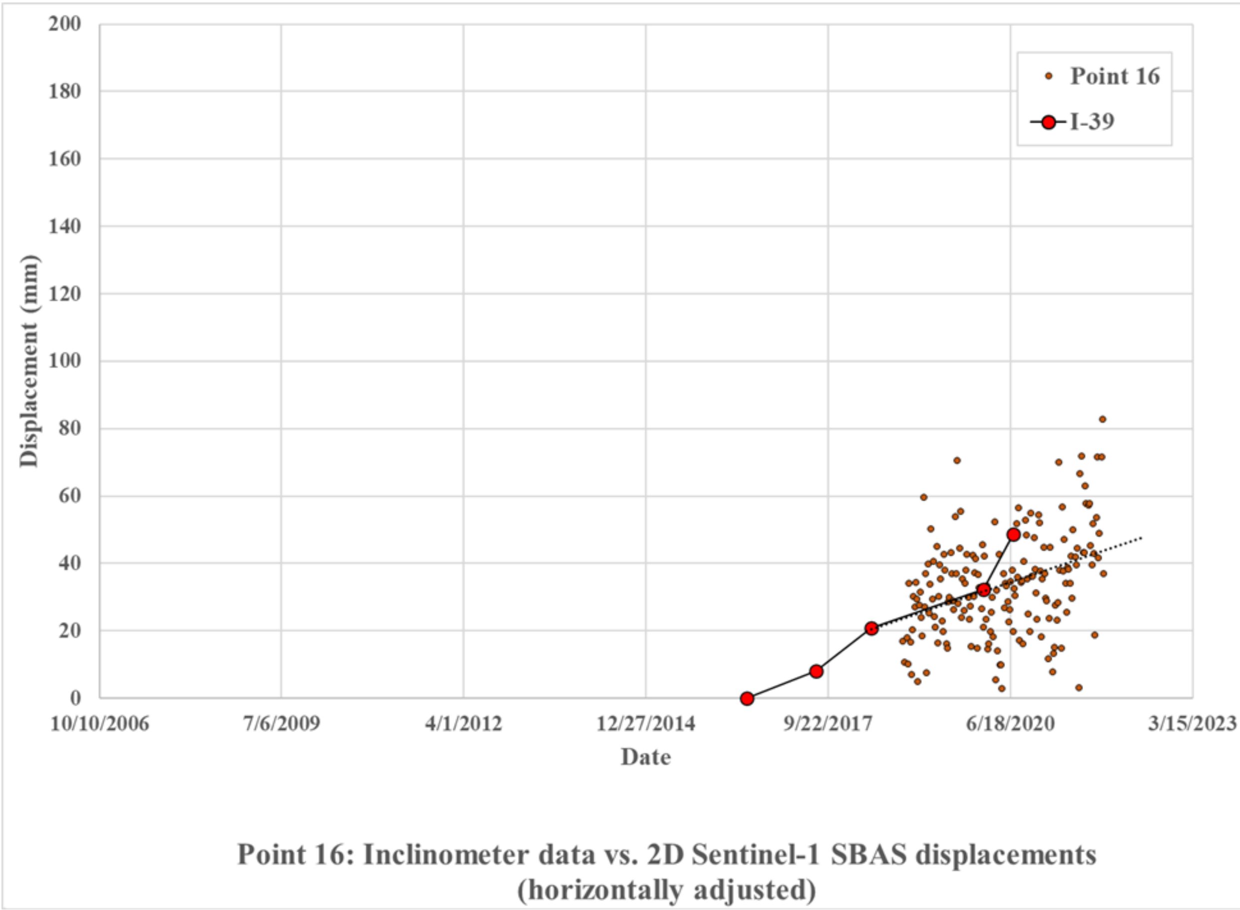

Figure 47 Inclinometer I-39 plotted with Point 16 displacement time-series

7.3.17. Inclinometer I-7 and SBAS measurements for Point 17

Time-series displacement measurements for Point 17 are plotted with the inclinometer readings from inclinometer I-7 in Figure 48. The SBAS dataset was collected from November 6, 2018, to December 14, 2021. It overlaps with inclinometer data from November 2018 to July 2020. Geolabs (2021) collected readings from July 2000 to July 2020. Note that data collected prior to October 2006 is not shown to maintain consistency in the y-axis range. Inclinometer I-7 was installed to a depth of 68 feet (Geolabs 2021). Geolabs (2021) noted that displacement readings collected may be inaccurate due to “instrumentation error but a comparison of the I-7 data with

SBAS measurements for Point 17 is still provided. SBAS measurements from the area are generally consistent with inclinometer data from May 2018 to January 2020.

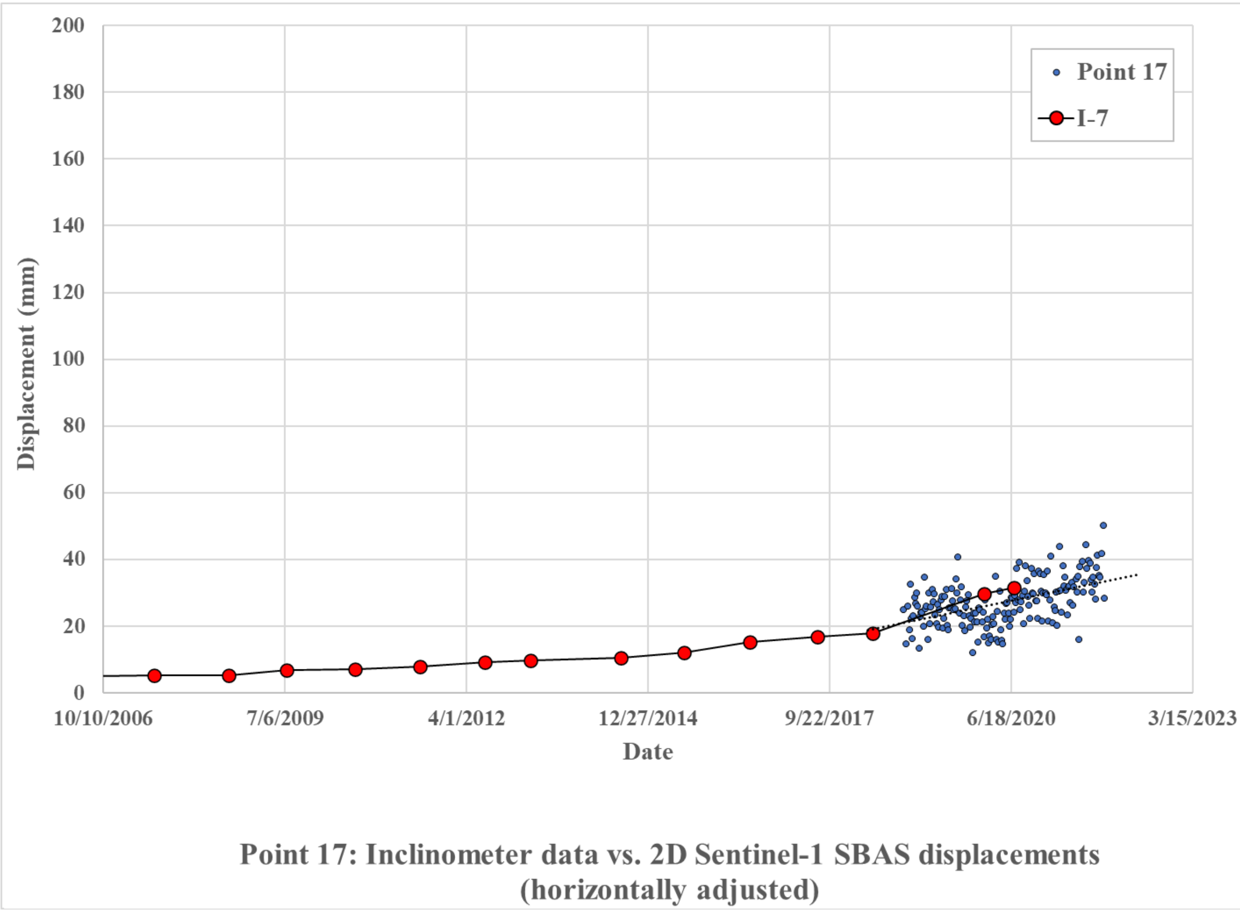

Figure 48 Inclinometer I-7 plotted with Point 17 displacement time-series

The comparisons in the case study generally demonstrate that 2D decomposition of SBAS measurements is effective when adjustments are made to the d_{east} displacement vector to match the true direction of movement. Use of SBAS is effective for detection and collecting measurements for slow-moving slides. Twelve (12) of the fourteen (14) comparisons for slow moving displacements have good agreement between inclinometer measurements and SBAS. All three (3) of the inclinometers that recorded rapid movement were not well captured by SBAS. The results indicate that determining rapid failure is not possible with SBAS.

8. SBAS TIME-SERIES ANALYSIS RESULTS FOR HAWAIʻI ISLAND AND THE ISLAND OF MAUI

This section presents the SBAS results for Hawaiʻi Island and Maui. The results highlight the capabilities and limitations of conducting SBAS in the Hawaiian Islands. Notable limitations are attibuted to vegetation, radar shadows caused by Haleakalā and Mauna Kea, and the spatial resolution of the satellite systems. .

8.1. *Hawaiʻi Island*

8.1.1. Hawaiʻi Island SBAS Sentinel-1 Descending Results

The Sentinel-1 descending SBAS results contain displacement measurements from June 04, 2018, to December 15, 2021, with no significant data gaps. Figure 49 shows a total of 292,681 points collected along the Northeast slope of the Mauna Kea. Each point contains displacement time-series measurements acquired from the descending line-of-sight of approximately 280° from North.

The color symbology for velocity measurements in Figure 49 show extreme negative and positive velocities of -48.02 mm/year and +24.23 mm/year, respectively. Route 19 is shown in black in Figure 49 below and labels are provided for mileposts 10 and 30. Areas circled in red are known to have historical occurrences of land sliding and rockfalls.

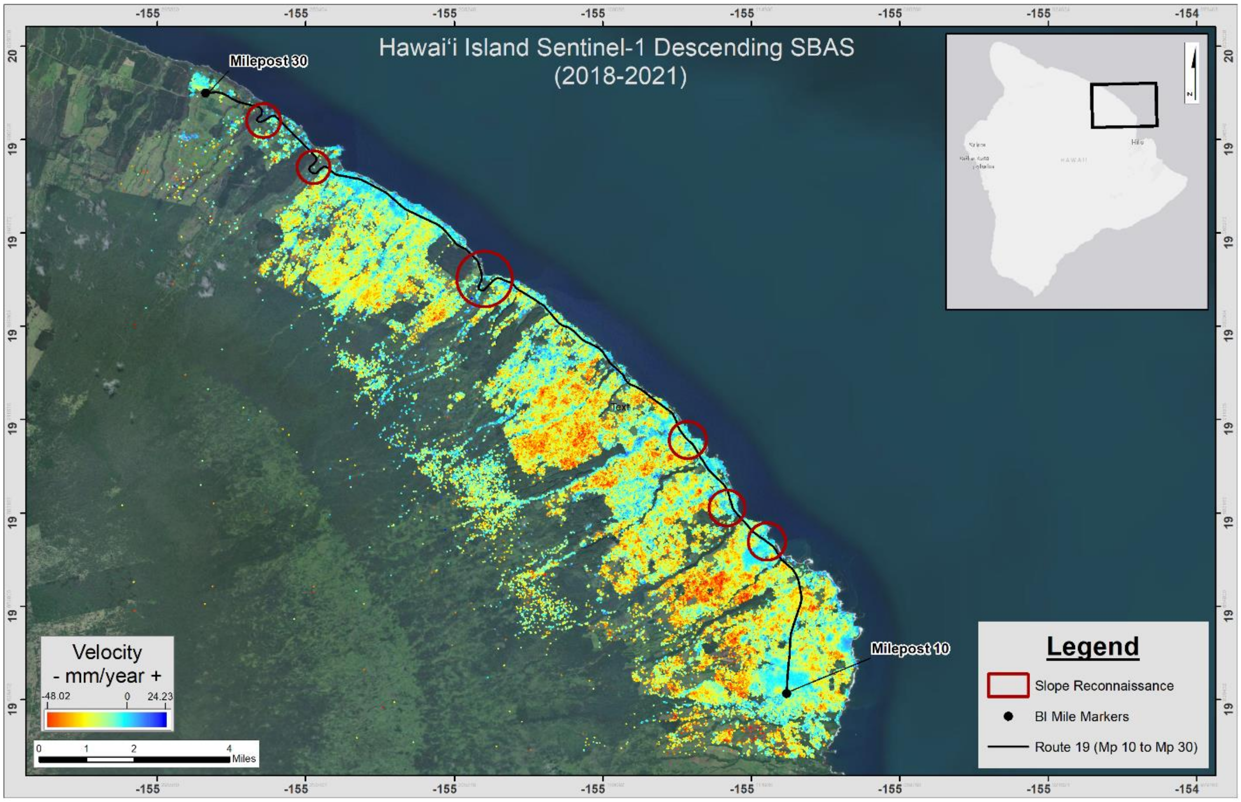

Figure 49 Hawai‘i Island Sentinel-1 descending SBAS results

8.1.2. Hawai‘i Island SBAS Sentinel-1 Ascending Results

The Sentinel-1 ascending SBAS results contain displacement measurements from December 13, 2014, to December 12, 2021. A significant data gap exists between May 18, 2015, and May 20, 2018. Figure 50 shows a total of 57,739 points collected along the Northeast slope of the Mauna Kea shield volcano. Each point contains displacement time-series measurements acquired from the ascending line-of-sight of approximately 79° from North.

The color symbology for velocity measurements in Figure 50 show extreme negative and positive velocities of -49.58 mm/year and +30.90 mm/year, respectively. Route 19 is shown in black in Figure 53 below and labels are provided for mileposts 10 and 30.

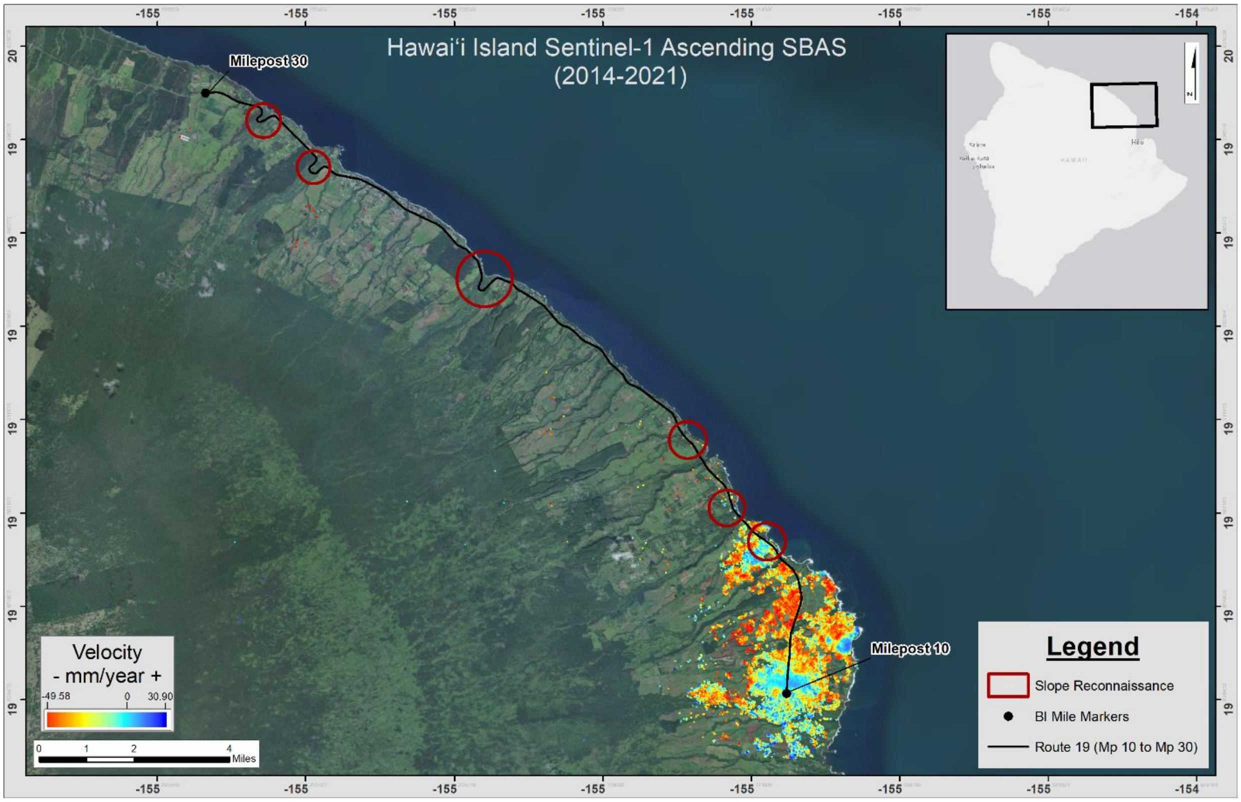

Figure 50 Hawaiʻi Island Sentinel-1 ascending SBAS results

Eight areas along Route 19 (Areas A through H) were selected for review based on point clusters with high displacement velocity values as shown below in Figure 51. The number of points with time-series displacements within each area ranged between 21 points (Area C, Nīnole) to 178 Points (Area B, Maulua). The average velocity and average coherence of all points within each selected area was calculated.

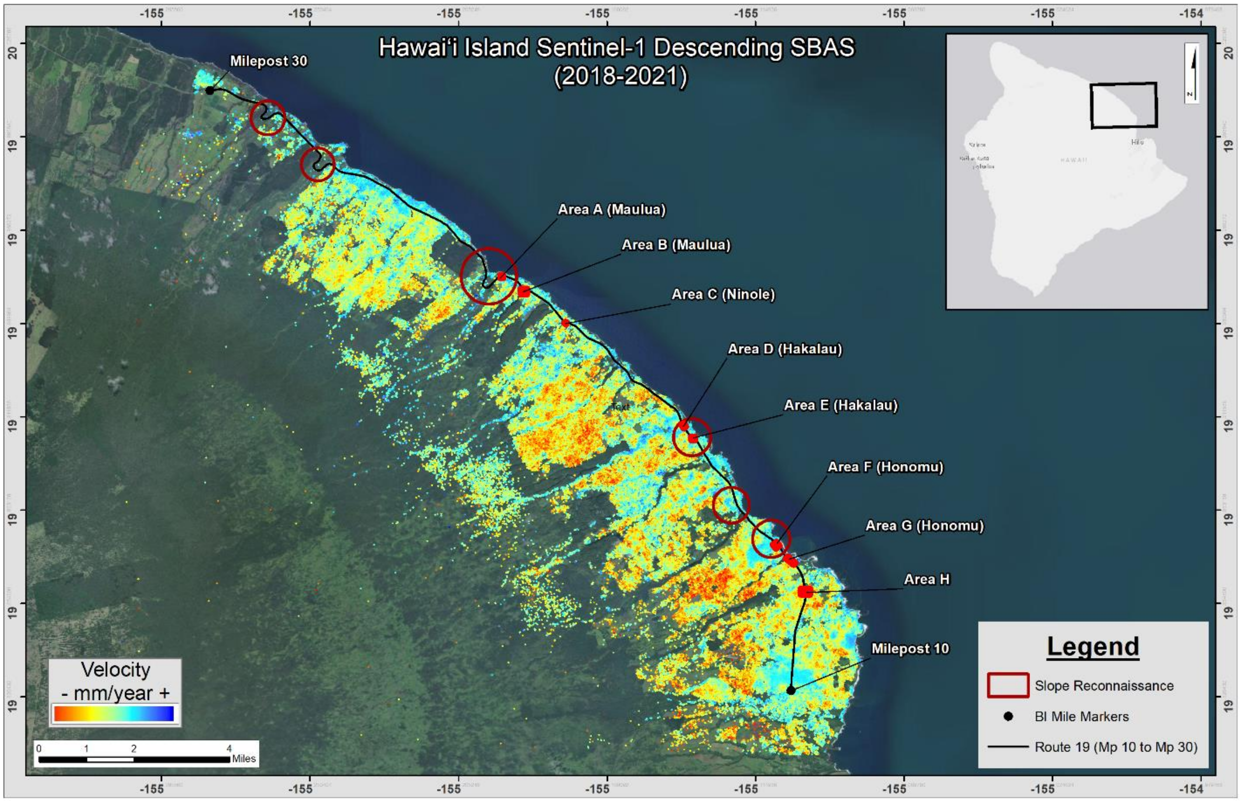

Figure 51 Selected areas of additional analysis

Five of the selected areas (Maulua A, Maulua B, Nīnole C, Hakalau D, and Hakalau E), did not have both descending and ascending SBAS results. Consequently, 2D decomposition could not be conducted and only descending line-of-sight measurements are provided.

For two of the locations (Honomū F and Honomū G), both ascending and descending datasets exist that allowed for 2D decomposition. After decomposition, the horizontal component was resolved to the downslope direction perpendicular to the contour lines. Figure 52 illustrates that the corrected (downslope) displacement is d_{East} divided by the cosine of θ.

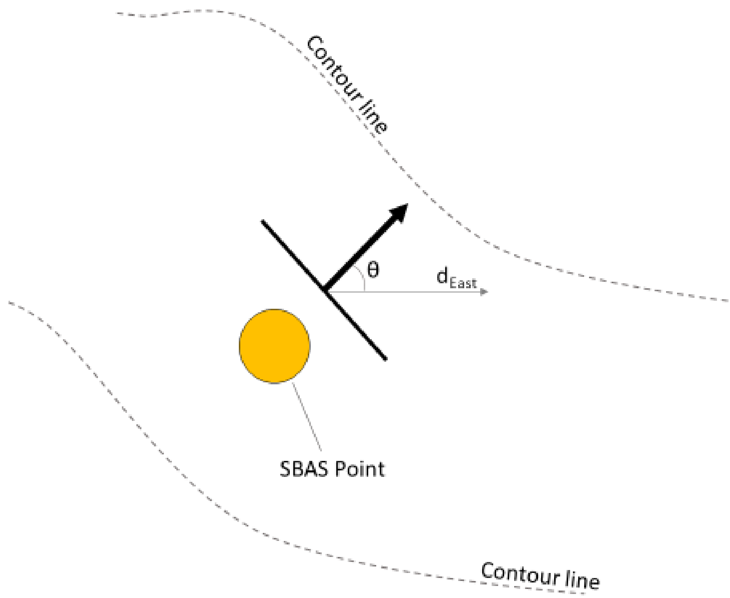

Figure 52 d_{East} displacements resolved to downslope direction

Area A

Area A (Maulua) is on a slope above the highway approximately halfway between mileposts 21 and 22 as shown in Figure 53. Area A is between GPS coordinates latitude 19.95457, longitude -155.19264 and latitude 19.9545, longitude -155.19159.

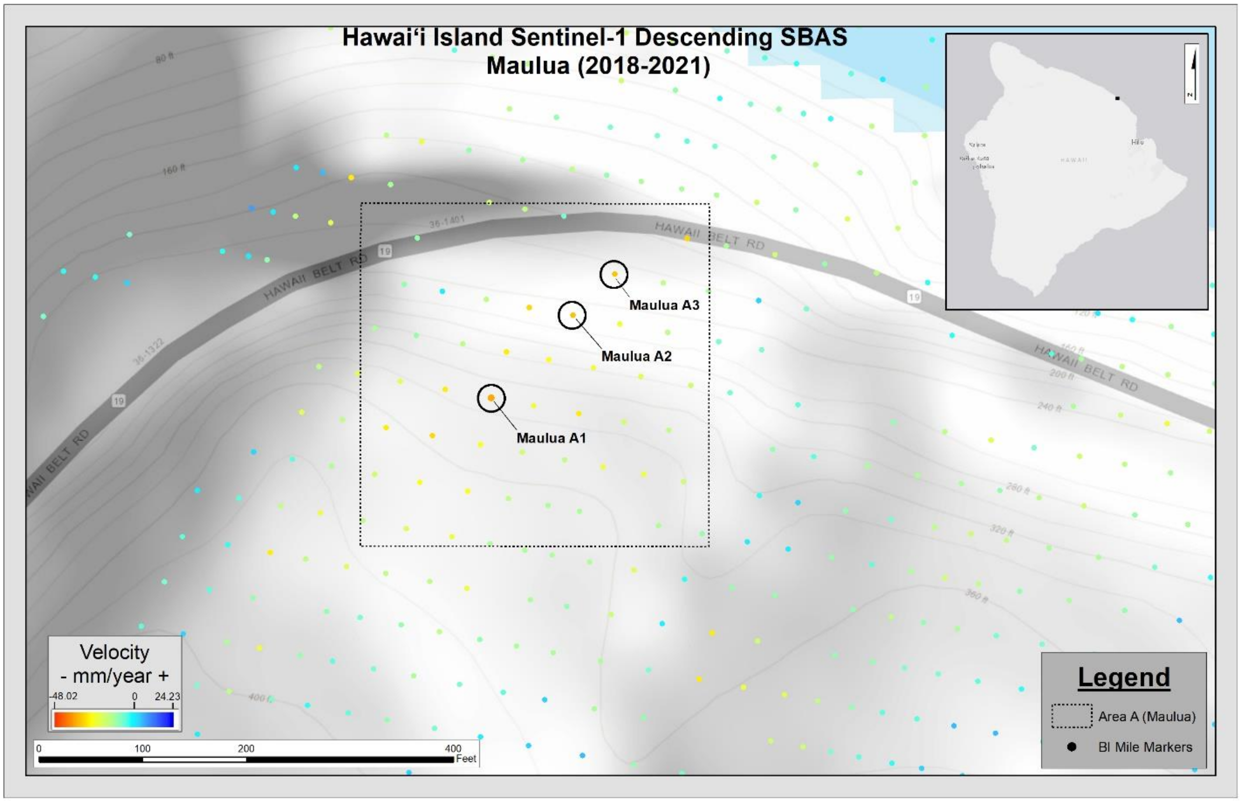

Figure 53 Location of Area A (Maulua)

There are 51 SBAS points within Area A. Line-of-sight displacements for three points with the highest values are shown in Figure 53 and are labeled as Maulua A1, Maulua A2, and Maulua A3. As seen in Figure 53, the line-of-sight displacements for the descending dataset with look direction of 280˚ will be in a direction that is nearly parallel to the slope contours. It is unlikely that the line-of-sight displacements can provide the true motion because the direction of slope movement in this case would likely be perpendicular to the contours which is almost true North.

The average velocity, total displacement, and calculated coherence of the Maulua A points are shown in Table 7. The total displacement is the value at the end of the analysis period of December 15, 2021.

Table 7 Ave. velocity, total displacement, and coherance for Maulua (Area A)

Point	Ave. Velocity (mm/year)	Total displacement (mm)	Calculated coherence
Maulua A1	-33.94	-98.69	0.223
Maulua A2	-29.65	-100.30	0.217
Maulua A3	-30.63	-115.20	0.193

The displacement time-series plots for Maulua A1, A2 and A3 are shown in figures 54, 55 and 56, respectively.

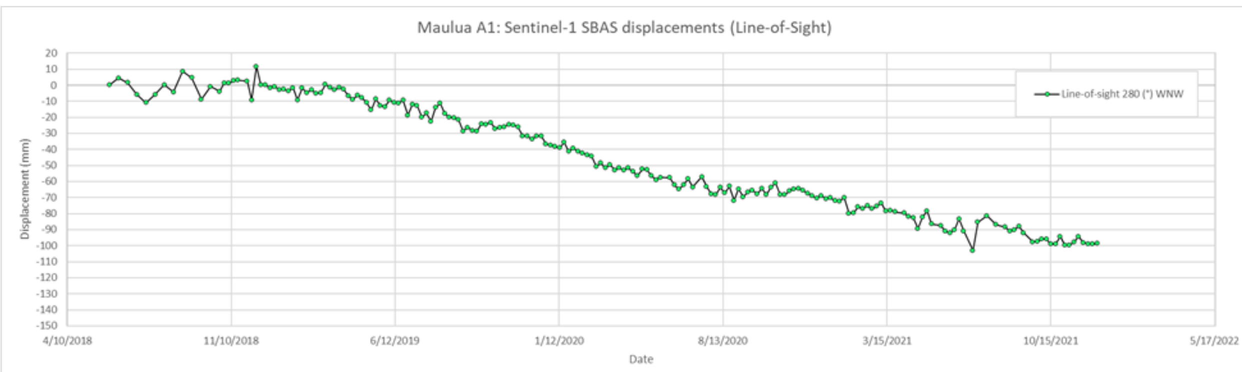

Figure 54 Line-of-sight time-series plot of Maulua A1

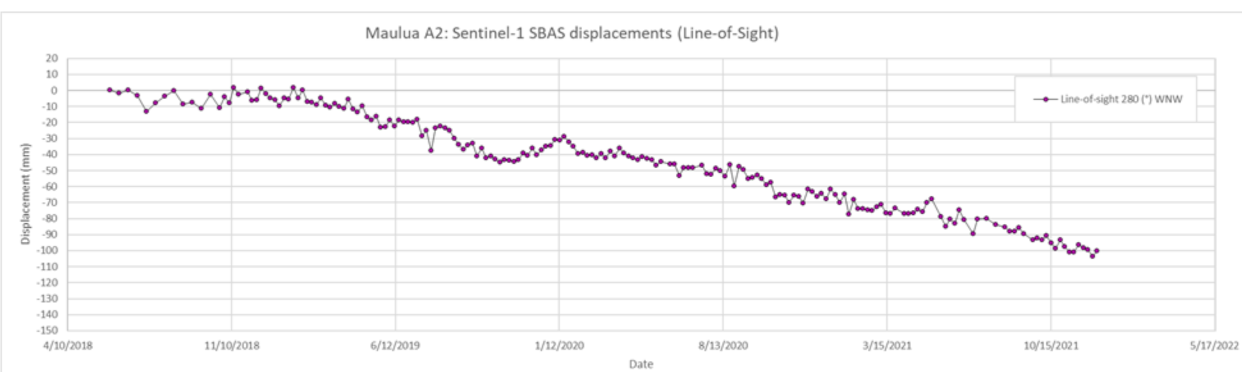

Figure 55 Line-of-sight time-series plots for Maulua A2

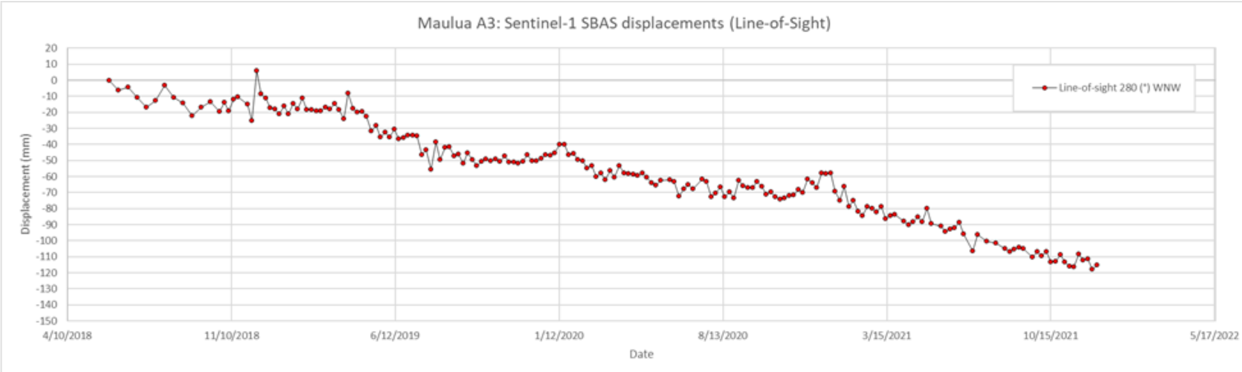

Figure 56 Line-of-sight time-series plots for Maulua A3

Area B

Area B (Maulua) is located south of the highway approximately 1000 feet (0.2 miles) to the east of Milepost 21. Area B is between GPS coordinates latitude 19.951, longitude -155.18579 and latitude 19.94985, longitude -155.18371 as shown in Figure 57.

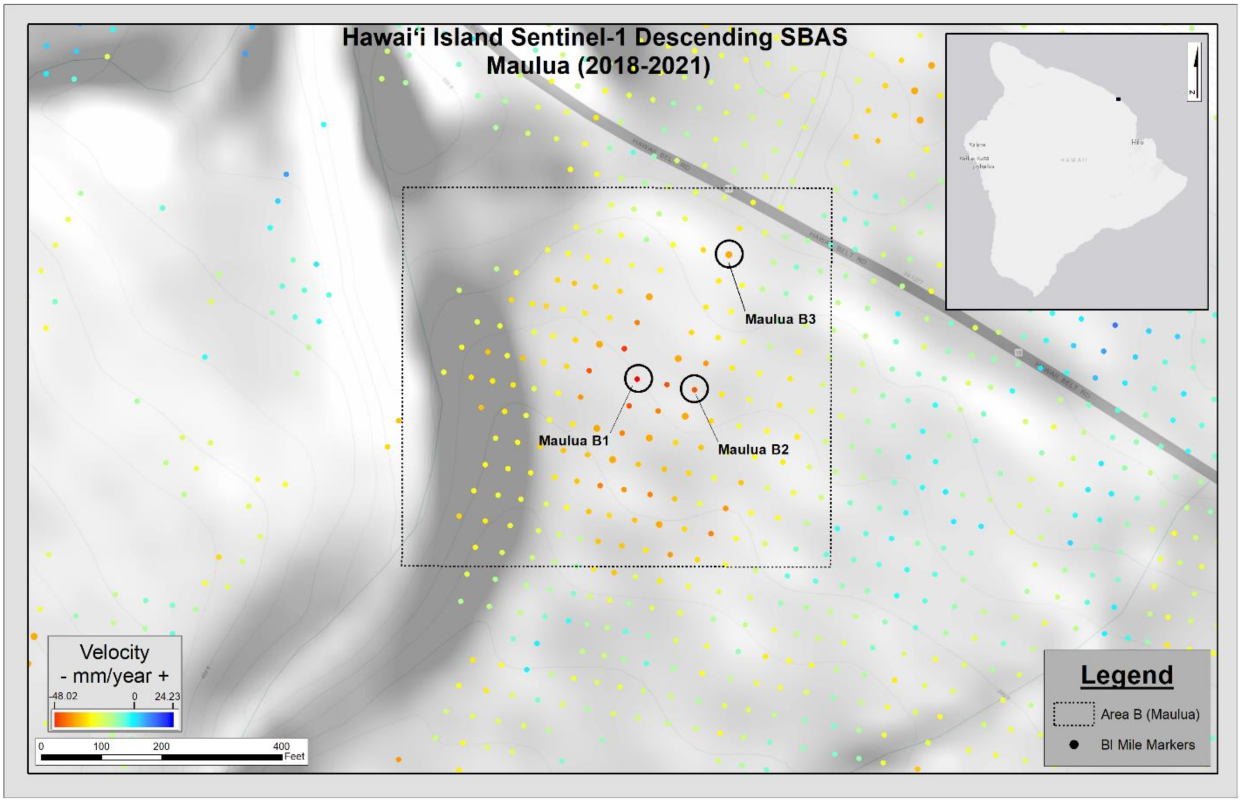

Figure 57 Location of interest for Area B (Maulua)

There are 178 SBAS points within the area with a calculated average velocity of -24.06 mm/year and a calculated average coherence of 0.227. Line-of-sight displacements for three points with the highest values are shown in Figure 57 and are labeled as Maulua B1, Maulua B2, and Maulua B3.

The measured average velocity, total measured displacement, and calculated coherence of the three points are shown in Table 8. The total displacement is the measured value of accumulated displacement at the end of the analysis period of December 15, 2021.

Table 8 Ave. velocity, total displacement, and coherance for Maulua (Area B)

Point	Ave. Velocity (mm/year)	Total displacement (mm)	Calculated coherence
Maulua B1	-47.01	-125.20	0.110
Maulua B2	-42.99	-118.90	0.239
Maulua B3	-33.22	-96.30	0.133

The displacement time-series plot for Maulua B1, B2 and B3 are shown in figures 58, 59 and 60, respectively.

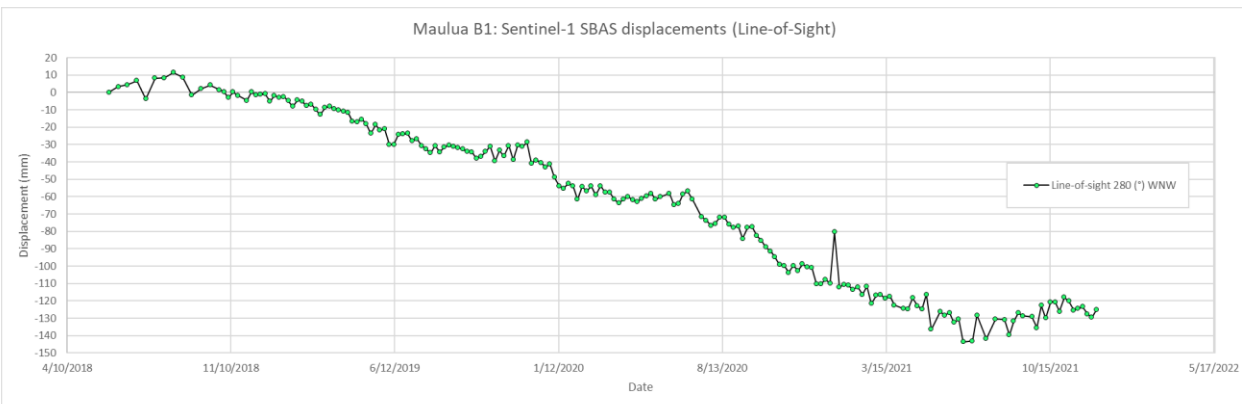

Figure 58 Line-of-sight time-series plot of Maulua B1

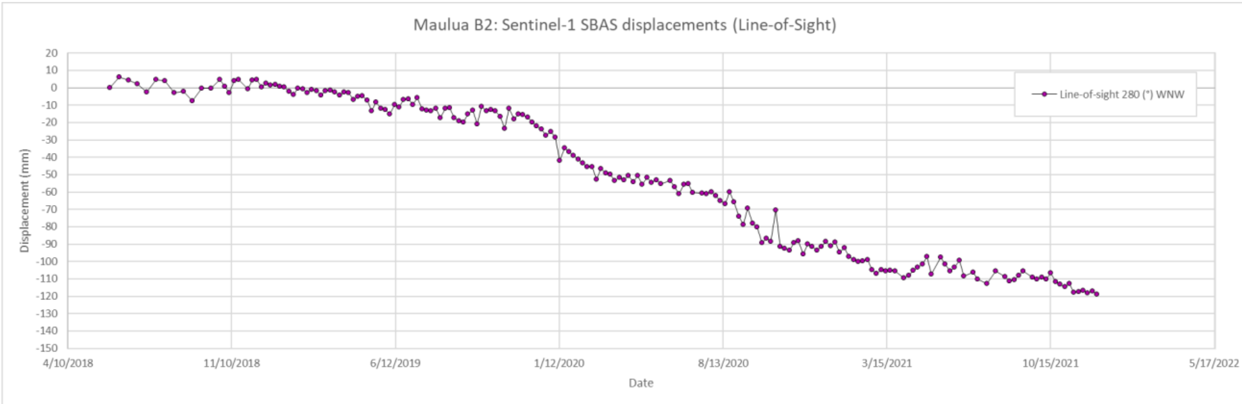

Figure 59 Line-of-sight time-series plot for Maulua B2

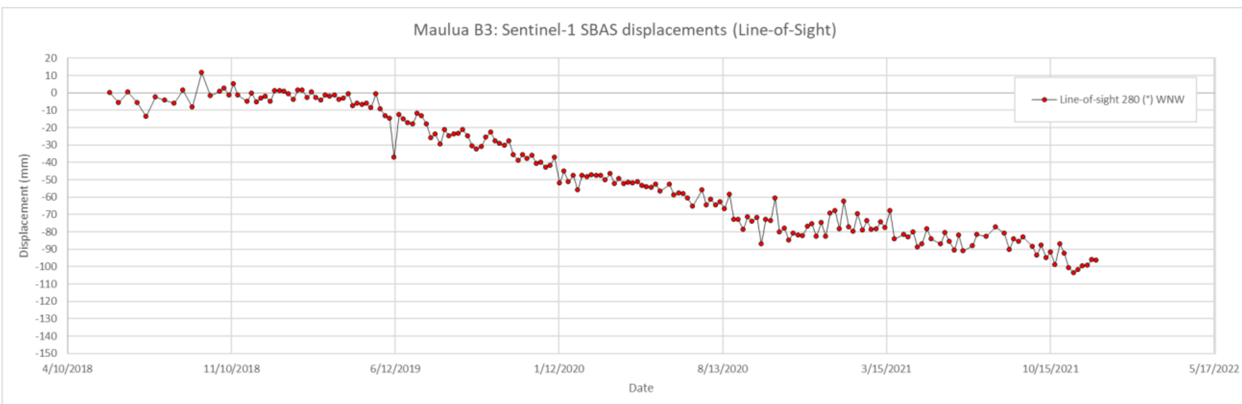

Figure 60 Line-of-sight time-series plot for Maulua B3

Area C

Area C (Nīnole) is on a slope to the south the highway approximately 1500 feet (0.3 miles) to the east of Milepost 20 as shown in Figure 61. Nīnole Stream is less than 150 feet to the east of the slope. Area C is between GPS coordinates latitude 19.94051, longitude -155.18579 and latitude 19.94018, longitude -155.17233.

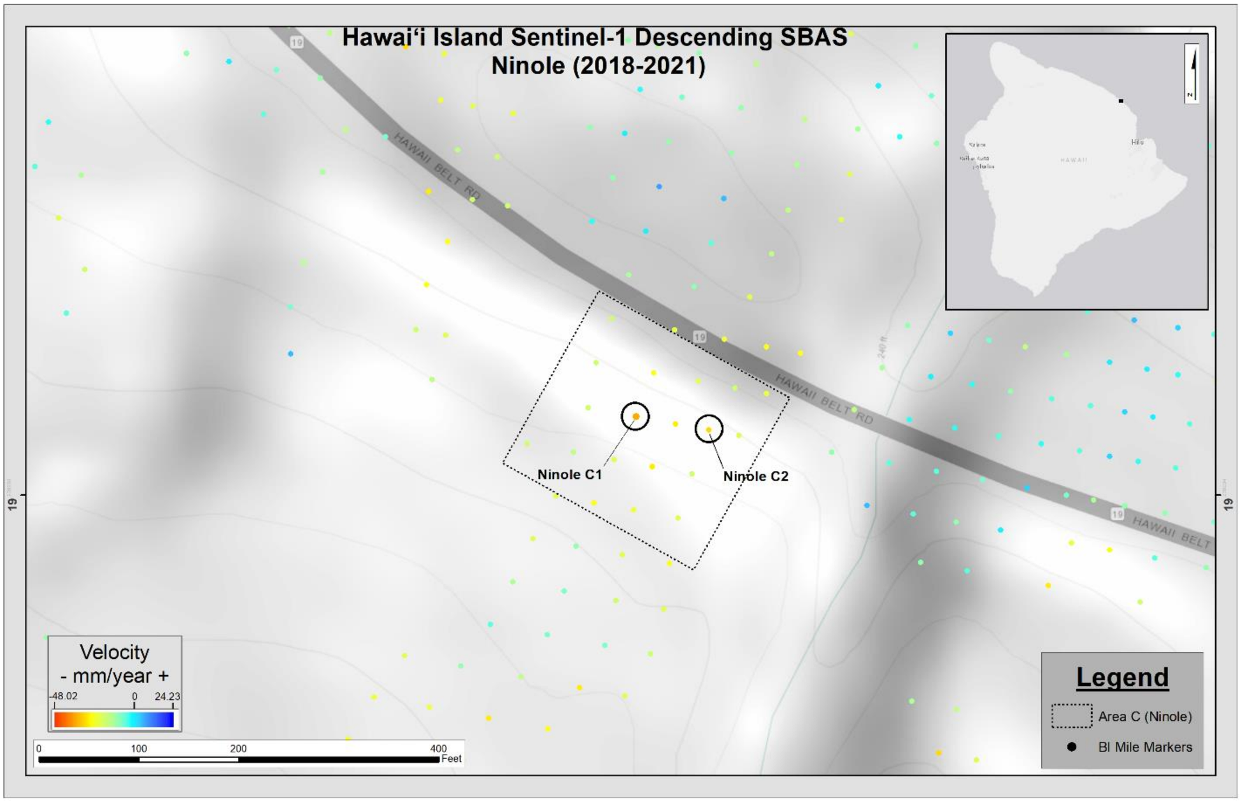

Figure 61 Location of interest for Area C (Nīnole)

There are 21 SBAS points within the area with a calculated average velocity of -20.15 mm/year and a calculated average coherence of 0.168. Two points with high measured displacements (Nīnole C1 and Nīnole C2) were selected for additional review.

The measured average velocity, total measured displacement, and calculated coherence of the selected points are shown in Table 9. The total displacement is the measured value of accumulated displacement at the end of the analysis period of December 15, 2021.

Table 9 Ave. velocity, total displacement, and coherance for Nīnole (Area C)

Point	Ave. Velocity (mm/year)	Total displacement (mm)	Calculated coherence
Nīnole C1	-32.92	-104.50	0.152
Nīnole C2	-28.44	-99.50	0.140

Line-of-sight displacement time-series plots for Nīnole C1 and C2 are shown in figures 62 and 63, respectively.

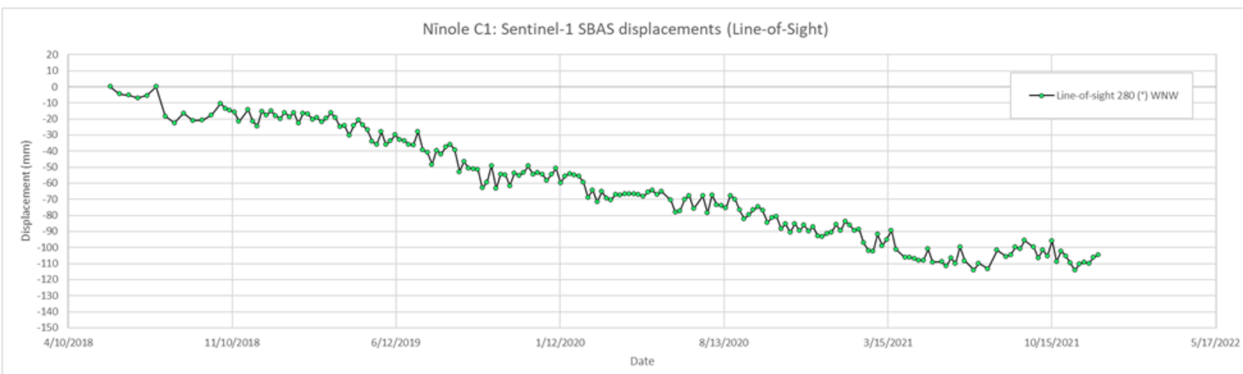

Figure 62 Line-of-sight time-series plot of Nīnole C1

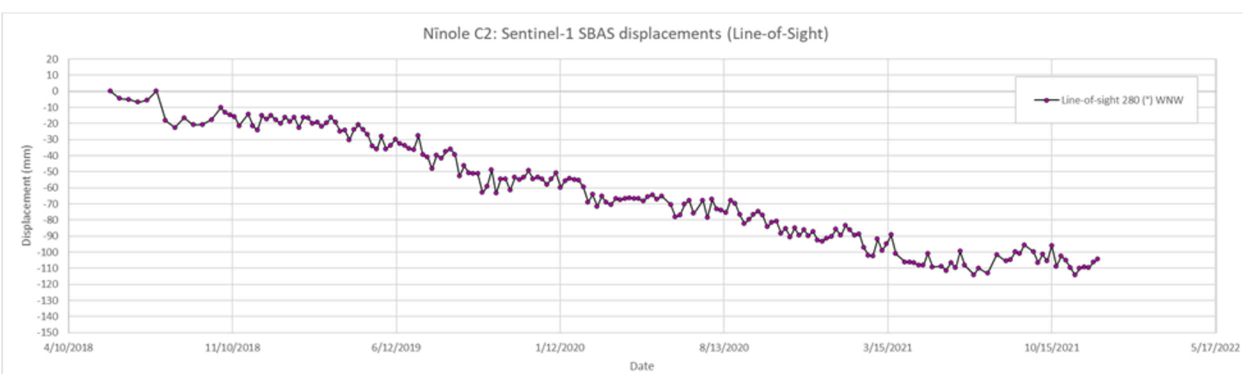

Figure 63 Line-of-sight time-series plot for Nīnole C2

Area D

Area D (Hakalau) encompasses land on either side of the highway. It is approximately 500 feet to the Northwest of Umauma Stream and is approximately halfway between Mileposts 17 and 16 as shown in Figure 64. GPS coordinates for Area D are between latitude 19.90941, longitude -155.13703 and latitude 19.90839, longitude -155.13637.

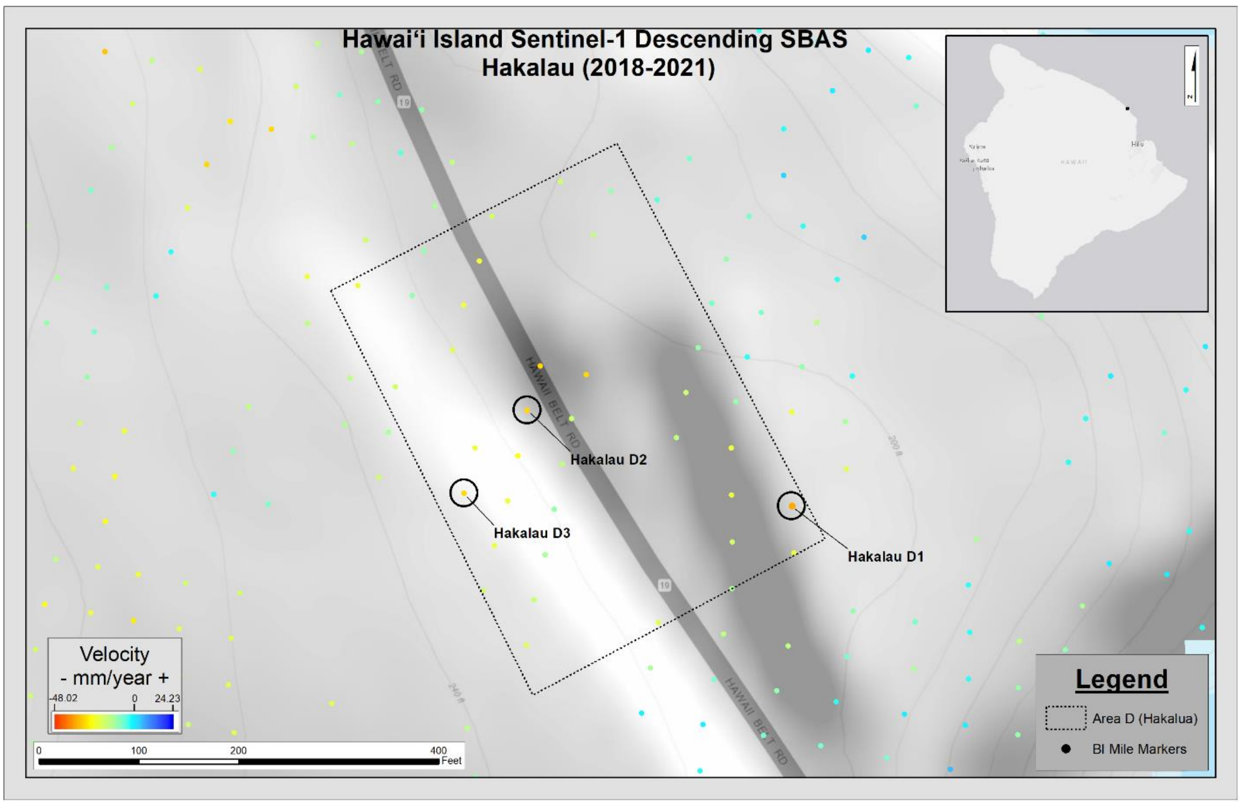

Figure 64 Location of interest for Area D (Hakalau)

There are 37 SBAS points within the area with a calculated average velocity of is -17.66 mm/year and a calculated average coherence of 0.123. Three Points with high measured displacements (Hakalau D1, Hakalau D2, and Hakalau D3) were selected for additional review.

The measured average velocity, total measured displacement, and calculated coherence of the selected points are shown in Table 10. The total displacement is the measured value of accumulated displacement at the end of the analysis period on December 15, 2021.

Table 10 Ave. velocity, total displacement, and coherance for Hakalau (Area D)

Point	Ave. Velocity (mm/year)	Total displacement (mm)	Calculated coherence
Hakalau D1	-32.18	-92.70	0.174
Hakalau D2	-27.55	-82.70	0.146
Hakalau D3	-29.077	-91.10	0.123

Line-of-sight displacement time-series plots for Hakalau D1, D2 and D3 are shown in figures 65, 66 and 67, respectively.

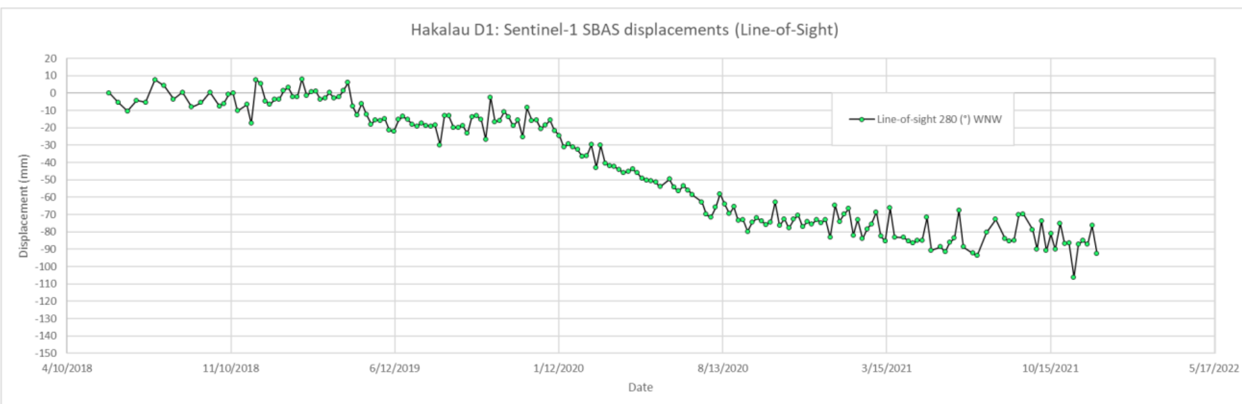

Figure 65 Line-of-sight time-series plot of Hakalau D1

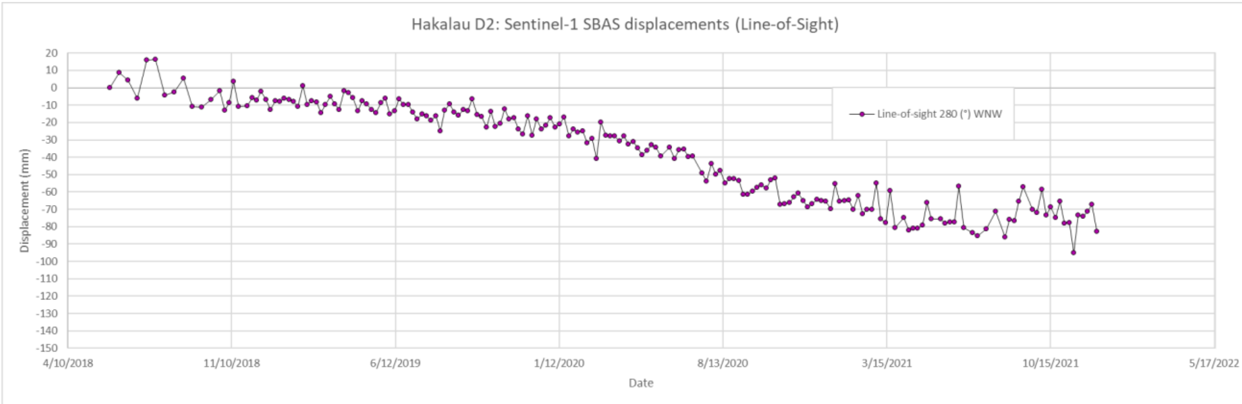

Figure 66 Line-of-sight time-series plots for Hakalau D2

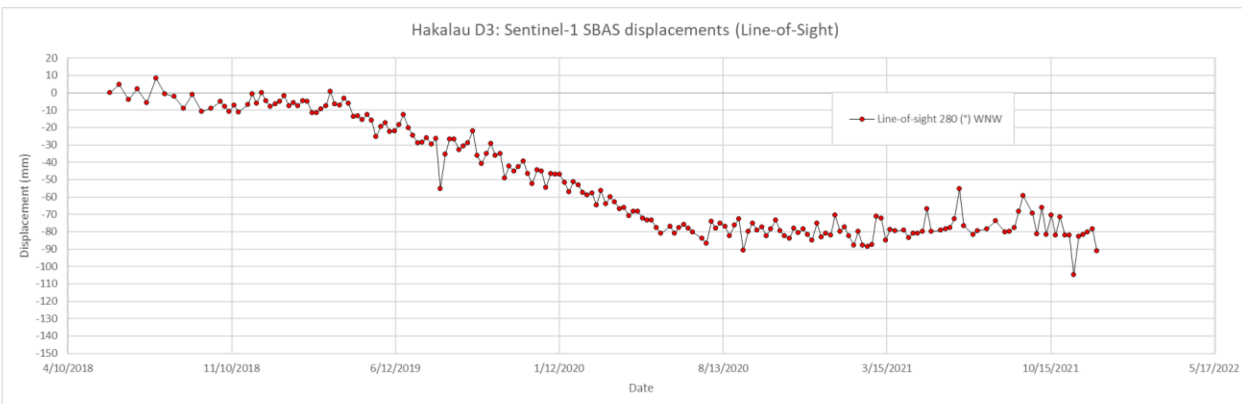

Figure 67 Line-of-sight time-series plot for Hakalau D3

Area E

Area E (Hakalau) encompasses land on either side of the highway and is approximately 150 feet to the Northwest of Leopolino Road and approximately 500 feet to the Northwest of Milepost 16 as shown in Figure 68. GPS coordinates for Area E are between latitude 19.90558, longitude -155.13439 and latitude 19.90461, longitude -155.13328.

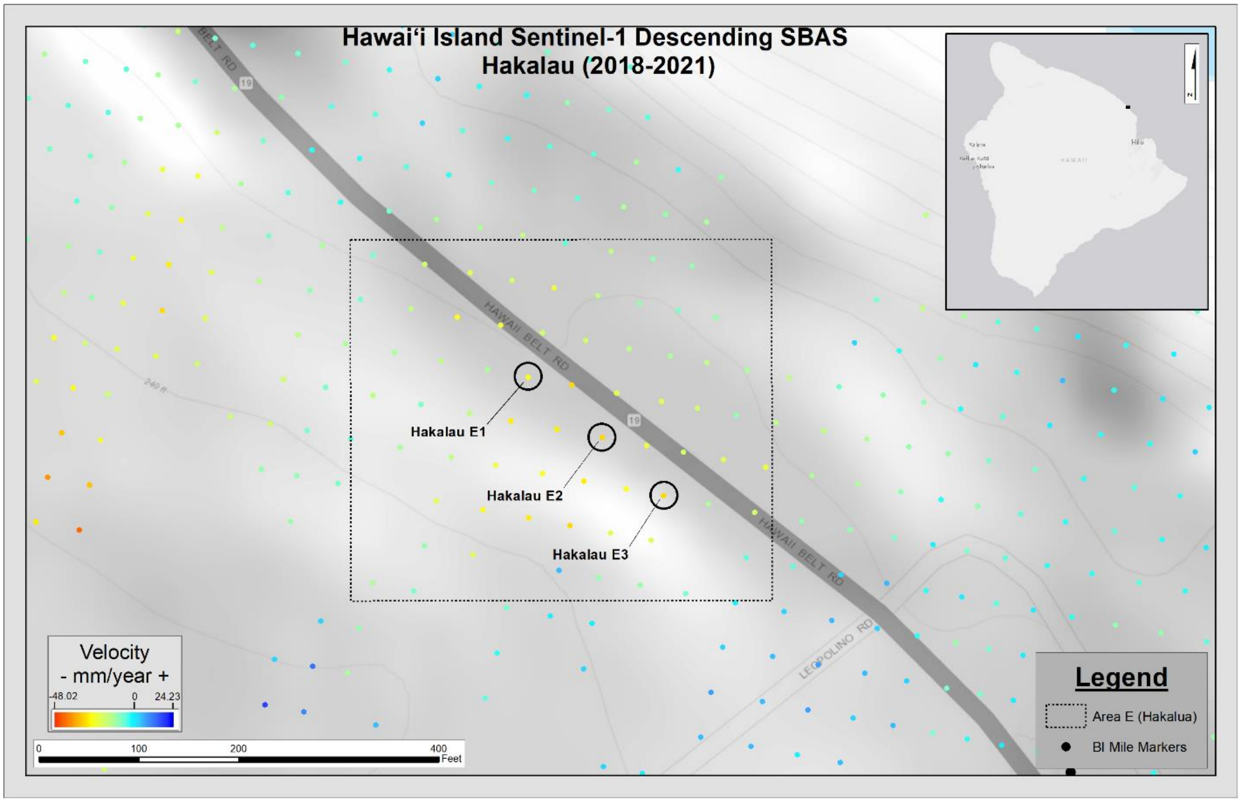

Figure 68 Location of interest for Area E (Hakalau)

There are 67 SBAS points within the area with a calculated average velocity of -14.98 mm/year and a calculated average coherence of 0.148. Three Points with high measured displacements (Hakalau E1, Hakalau E2, and Hakalau E3) were selected for further review.

The measured average velocity, total measured displacement, and calculated coherence of the points are shown in Table 11. The total displacement is the measured value of accumulated displacement at the end of the analysis period of December 15, 2021.

Table 11 Ave. velocity, total displacement, and coherance for Hakalau (Area E)

Point	Ave. Velocity (mm/year)	Total displacement (mm)	Calculated coherence
Hakalau E1	-24.35	-84.40	0.125
Hakalau E2	-27.34	-99.90	0.154
Hakalau E3	-27.989	-82.40	0.169

The line-of-sight displacement time-series plots for Hakalau E1, E2 and E3 are shown in figures 69, 70 and 71, respectively.

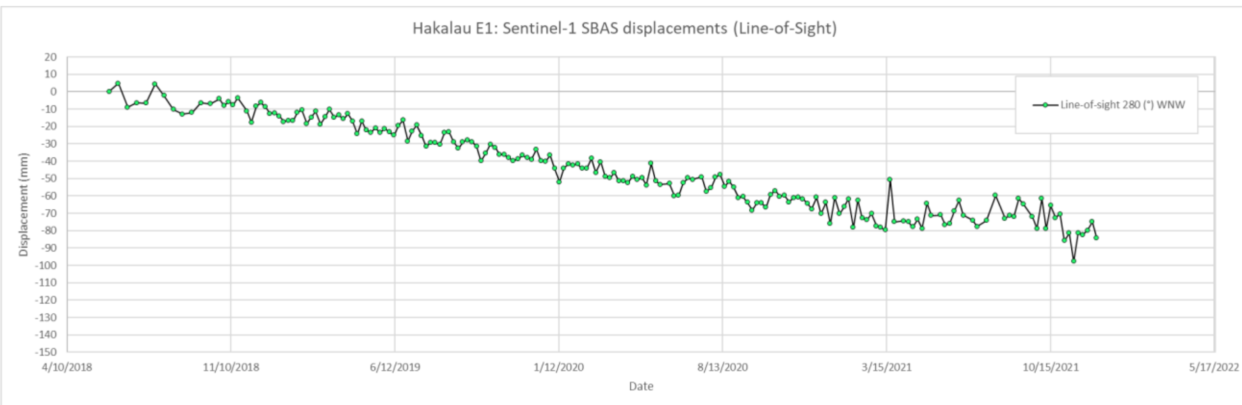

Figure 69 Line-of-sight time-series plot of Hakalau E1

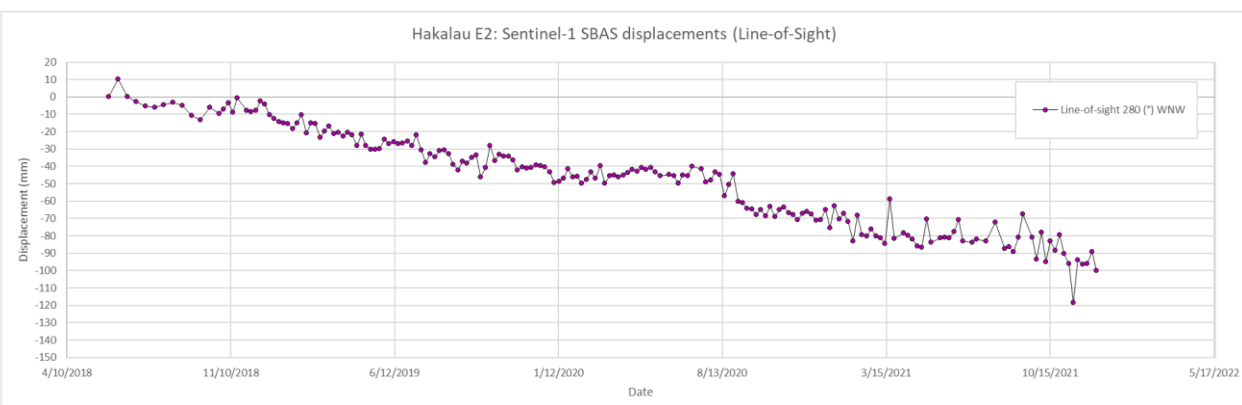

Figure 70 Line-of-sight time-series plot for Hakalau E2

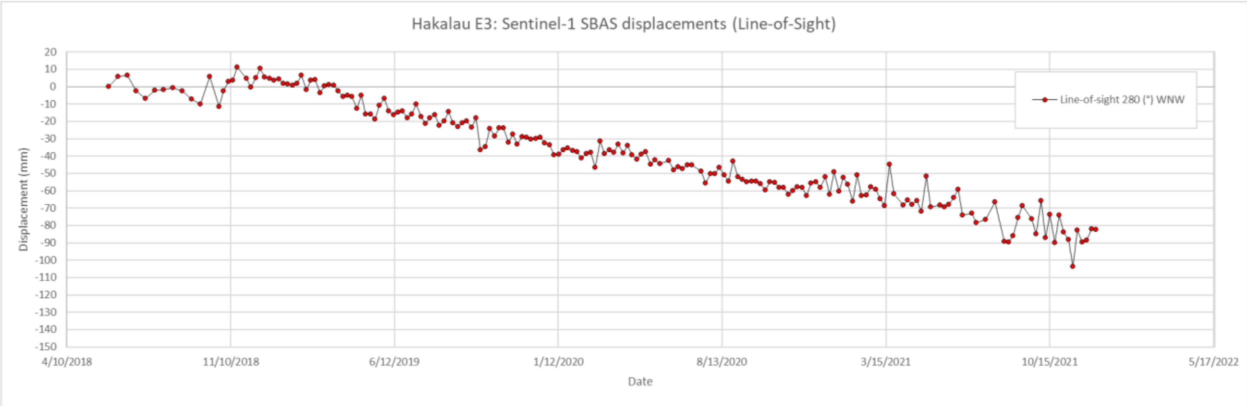

Figure 71 Line-of-sight time-series plot for Hakalau E3

Area F

On a slope to the southwest of Route 19, Area F (Honomū) is approximately 1300 feet (0.24 miles) to the Northwest of Milepost 13 and Honomū Stream as shown in Figure 72. GPS coordinates for Area F are between latitude 19.87336, longitude -155.10886 and latitude 19.87226, longitude -155.10775.

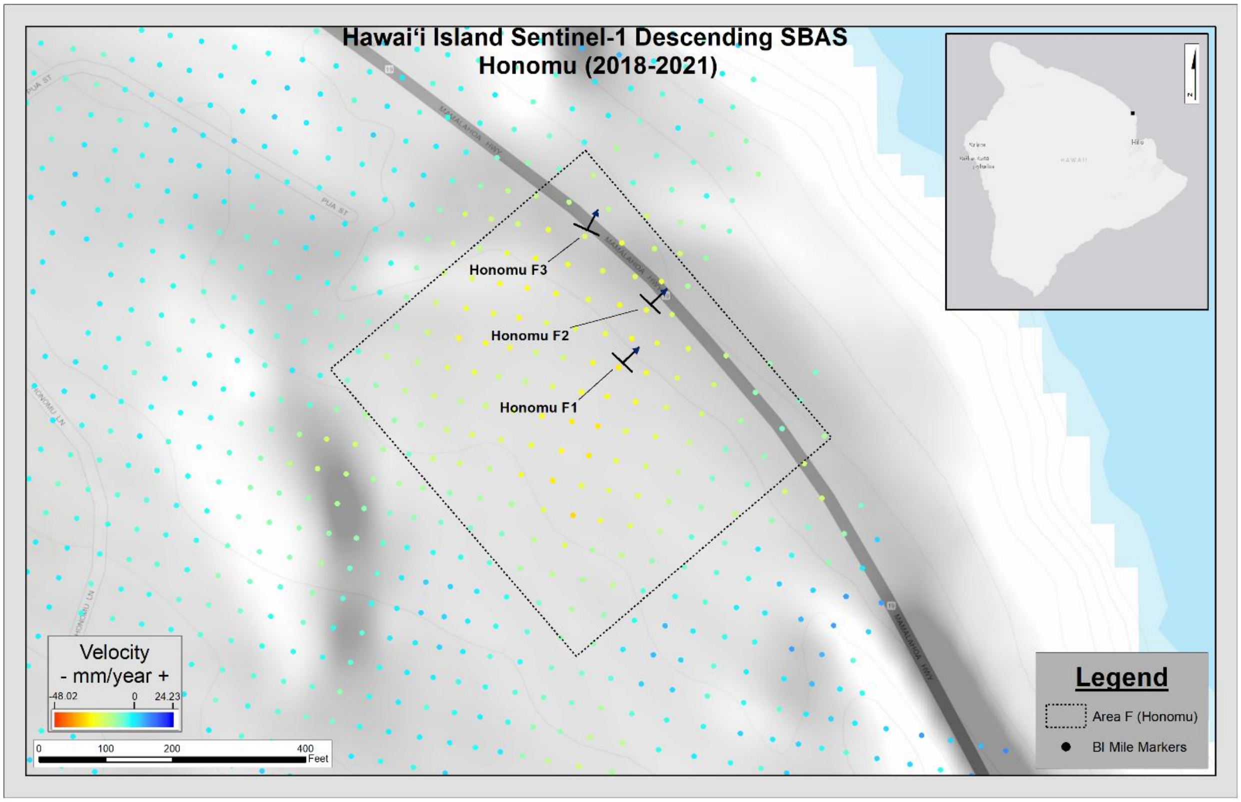

Figure 72 Location of interest for Area F (Honomū)

There are 130 SBAS points within the area with a calculated average velocity of -16.26 mm/year and a calculated average coherence of 0.260. Three Points with high measured displacements (Honomū F1, Honomū F2, and Honomū F3) were selected for further review. Strike and dip symbols are provided at each point to indicate the slope orientation.

The line-of-sight and decomposed displacement time-series plots for Honomū F1, F2 and F3 are shown in figures 73, 74 and 75, respectively. Displacements shown include the descending and ascending line-of-sight, the east facing displacement vector, the vertical displacement vector, and the adjusted-to-slope estimate. Based on the adjusted-to-slope estimate, displacements for points F1, F2 and F3 are ±10 to 25 mm on average over the monitoring period indicating that movements are not significant.

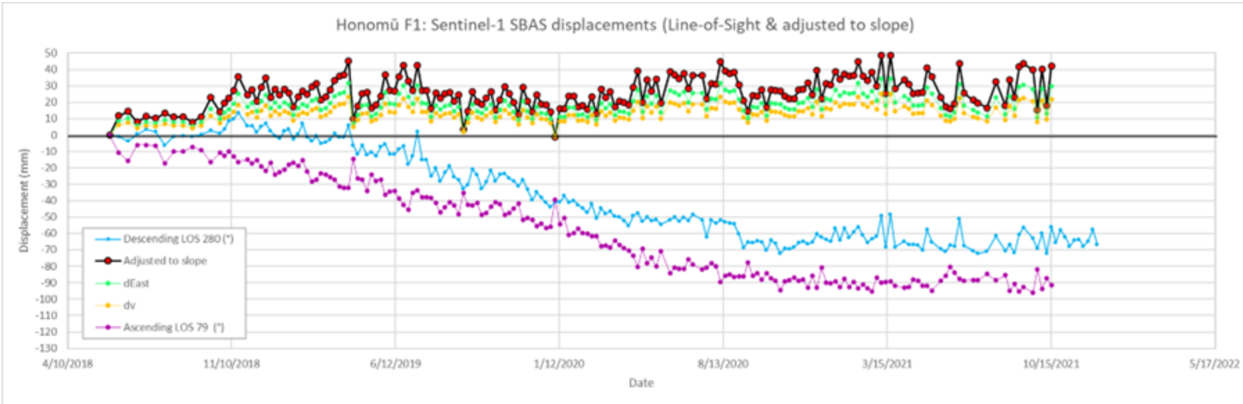

Figure 73 Line-of-sight and adjusted time-series plot of Honomū F1

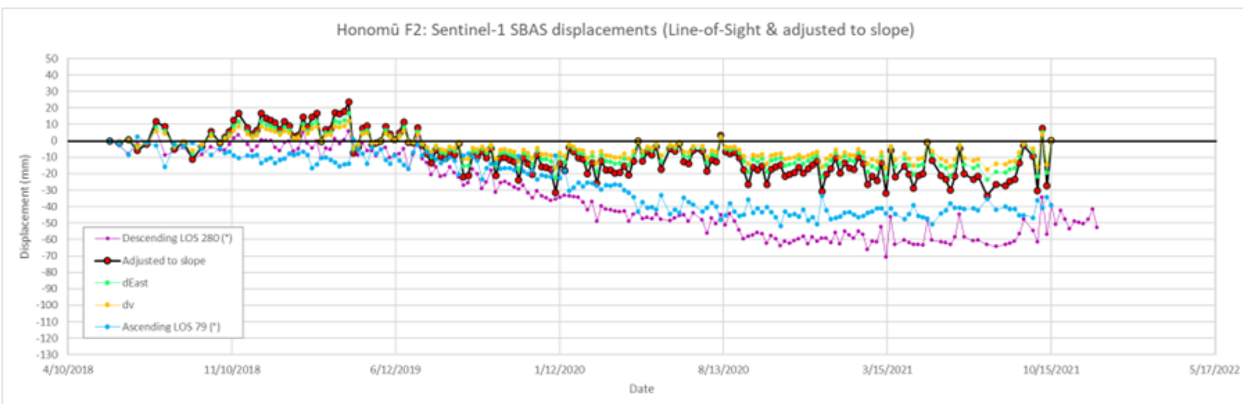

Figure 74 Line-of-sight and adjusted time-series plots for Honomū F2

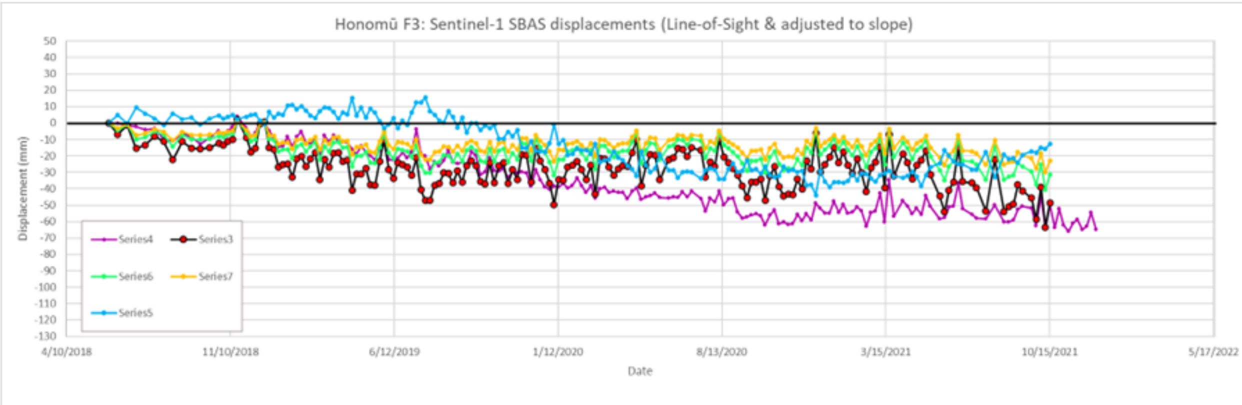

Figure 75 Line-of-sight and adjusted time-series plots for Honomū F3

Area G

Area G (Honomu) encompasses land on either side of the highway and is approximately 200 feet to the Southeast of Milepost 13 and 150 feet to the Southeast of Honomū Stream as shown in Figure 76. GPS coordinates for Area G are between latitude 19.86884, longitude -155.10526 and latitude 19.86677, longitude -155.10309.

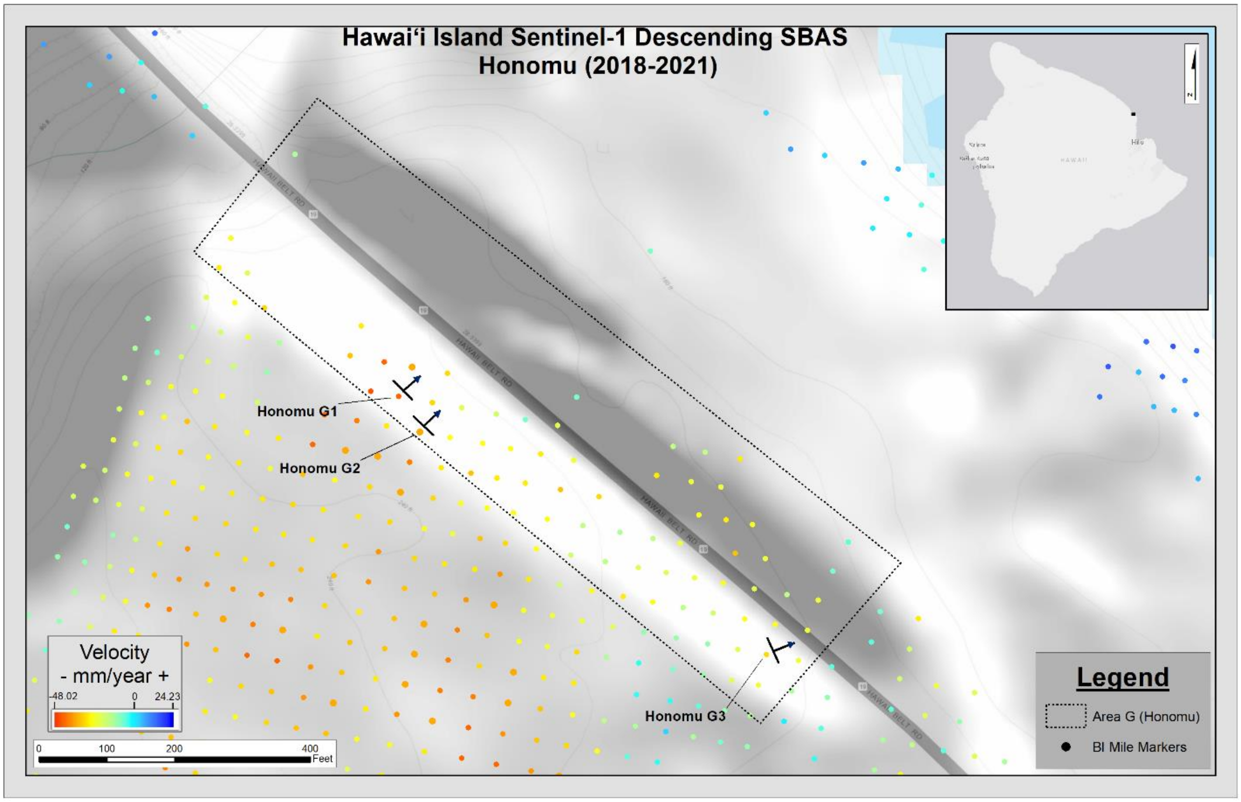

Figure 76 Location of interest for Area G (Honomū)

There are 74 SBAS points within the area with a calculated average velocity of -21.00 mm/year and a calculated average coherence of 0.153. Three points with high measured displacements (Honomū G1, Honomū G2, and Honomū G3) were selected for further review.

The line-of-sight and adjusted displacement time-series plots for Honomū G1, G2 and G3 are shown in figures 77, 78 and 79, respectively. Based on the adjusted-to-slope estimate, true displacements for these points are less significant than LOS values.

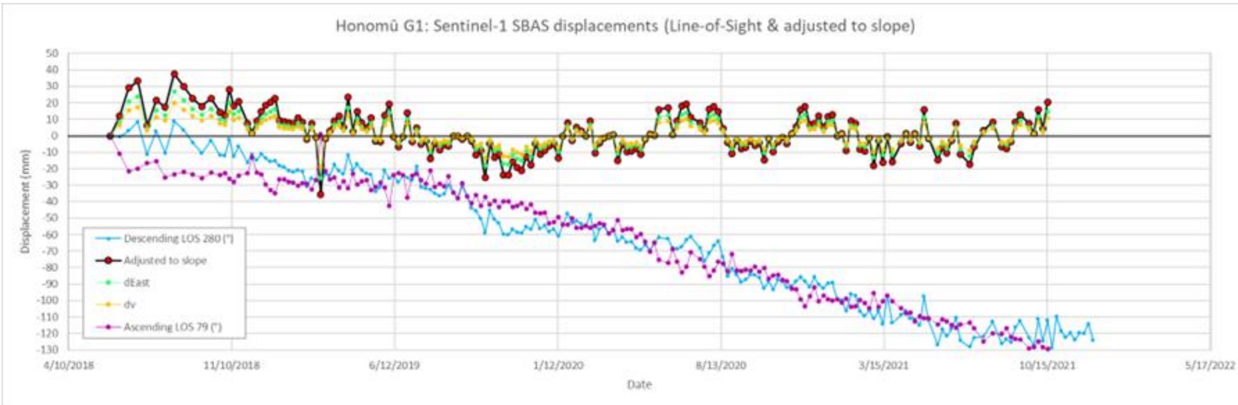

Figure 77 Line-of-sight and adjusted time-series plot of Honomū G1

Figure 78 Line-of-sight and adjusted time-series plots for Honomū G2

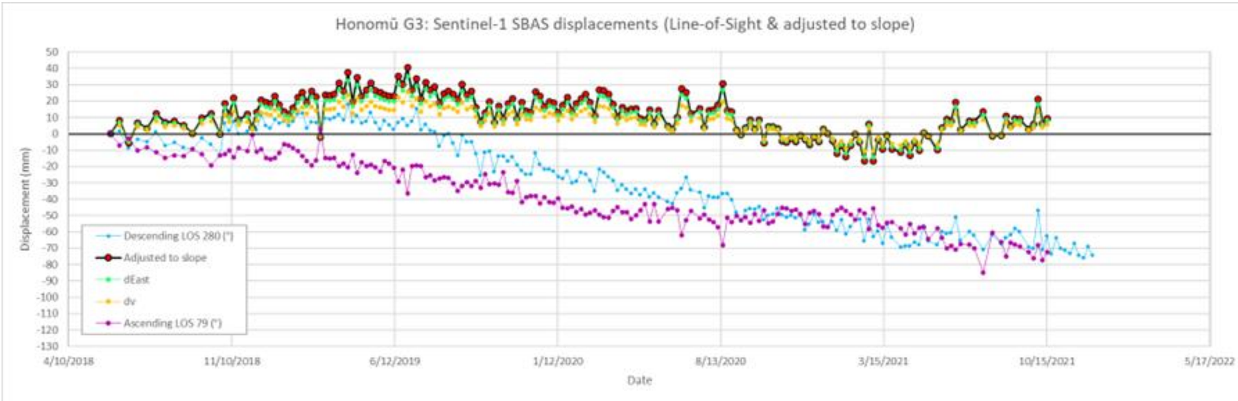

Figure 79 Line-of-sight and adjusted time-series plots for Honomū G3

Area H

Area H encompasses land on either side of the highway and is approximately 200 feet to the North of Milepost 12 as shown in Figure 80. GPS coordinates for Area H are between latitude 19.85924, longitude -155.09993 and latitude 19.85752, longitude -155.09966.

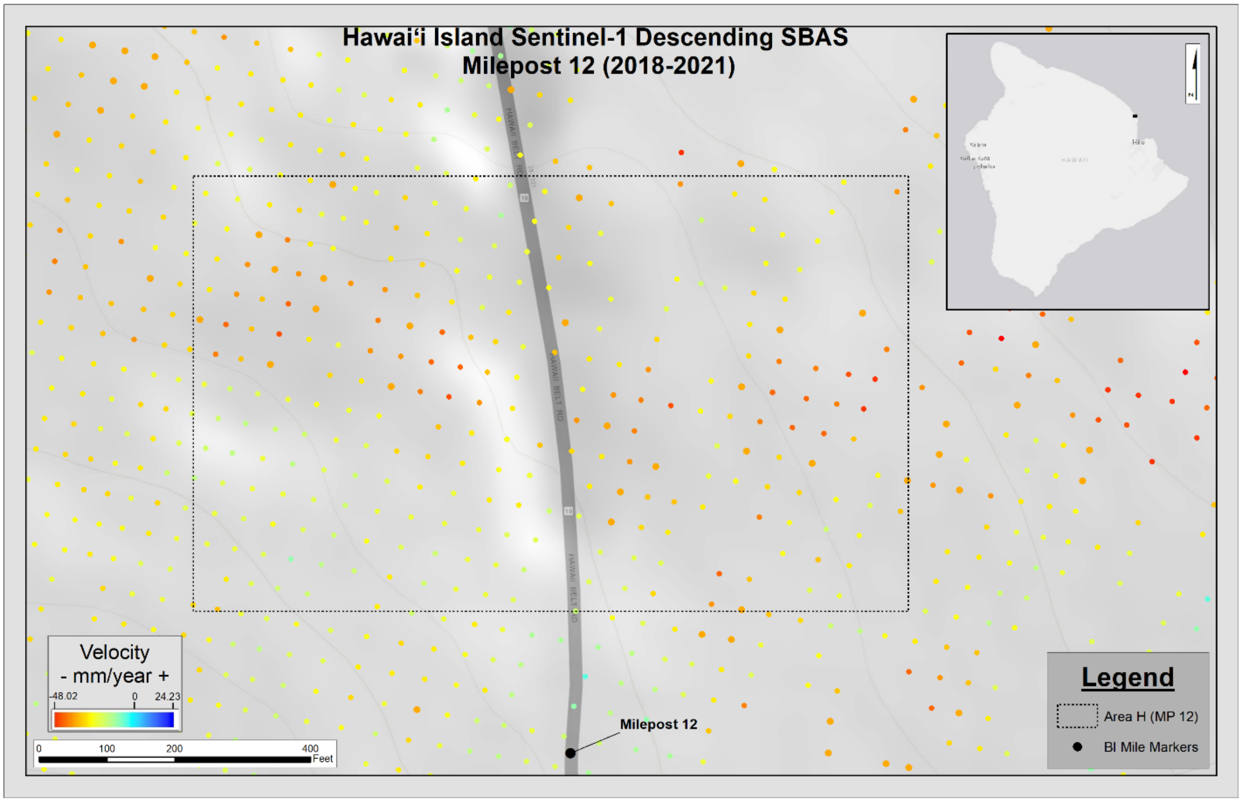

Figure 80 Location of interest for Area H (Milepost 12)

Review of the area with aerial imagery shows that displacement measurements from the location are likely the result of agricultural activity. Figure 81 shows aerial imagery with displacements overlaying the image. . Because the displacements are likely related to agricultural activities, no review of time-series displacement plots was conducted.

Figure 81 Location of interest for Area H (Milepost 12)

8.1.3. Hawai‘i Island SBAS ALOS-1 PALSAR-1 Descending Results

The Hawai‘i Island ALOS-1 PALSAR-1 descending SBAS results include measurements from May 28, 2006, to March 11, 2011. Because there were only 13 SLC images used in the interferometric stack, there are large data gaps between each displacement measurement. The duration of each data gap is between 1.5 months to 6 months. The ALOS SBAS results consist of 321,769 points. Figure 82 presents the ALOS-1 PALSAR-1 results.

The extreme negative and positive velocities of the dataset are -14.96 mm/year and +21.35 mm/year, respectively.

Figure 82 shows that the points to the left consist of data with primarily positive velocity values whereas those to the right are primarily negative. This pattern is suggestive of residual phase ramps, meaning that the results likely do not represent accurate measurements of displacement rates in the study area. Typically, SBAS analysis is conducted with greater than 20-30 SLC images. The exercise was conducted to investigate whether the L-band wavelengths with generally greater penetration through vegetated areas, would yield a favorable dataset. However, due to the presence of residual phase ramps, the dataset was abandoned. However, some further analysis of the time-series information is conducted below to review the data for patterns.

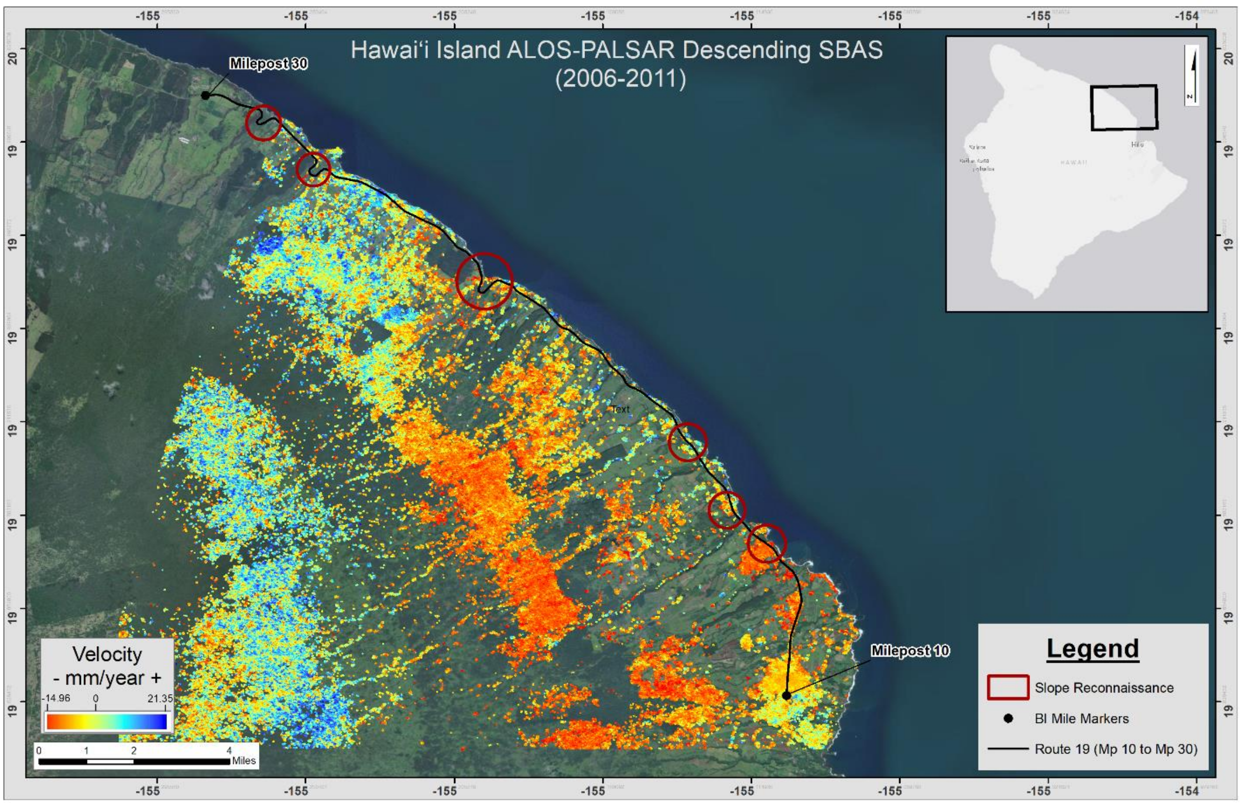

Figure 82 Hawai'i Island ALOS-1 PALSAR-1 descending SBAS results

To evaluate the effect of residual phase ramps, random points were selected to review their time-series displacement measurements in two areas. Figure 83 shows two areas, Area X to the west and area Y to the east. Random points in each area were selected to determine if patterns are present in the data.

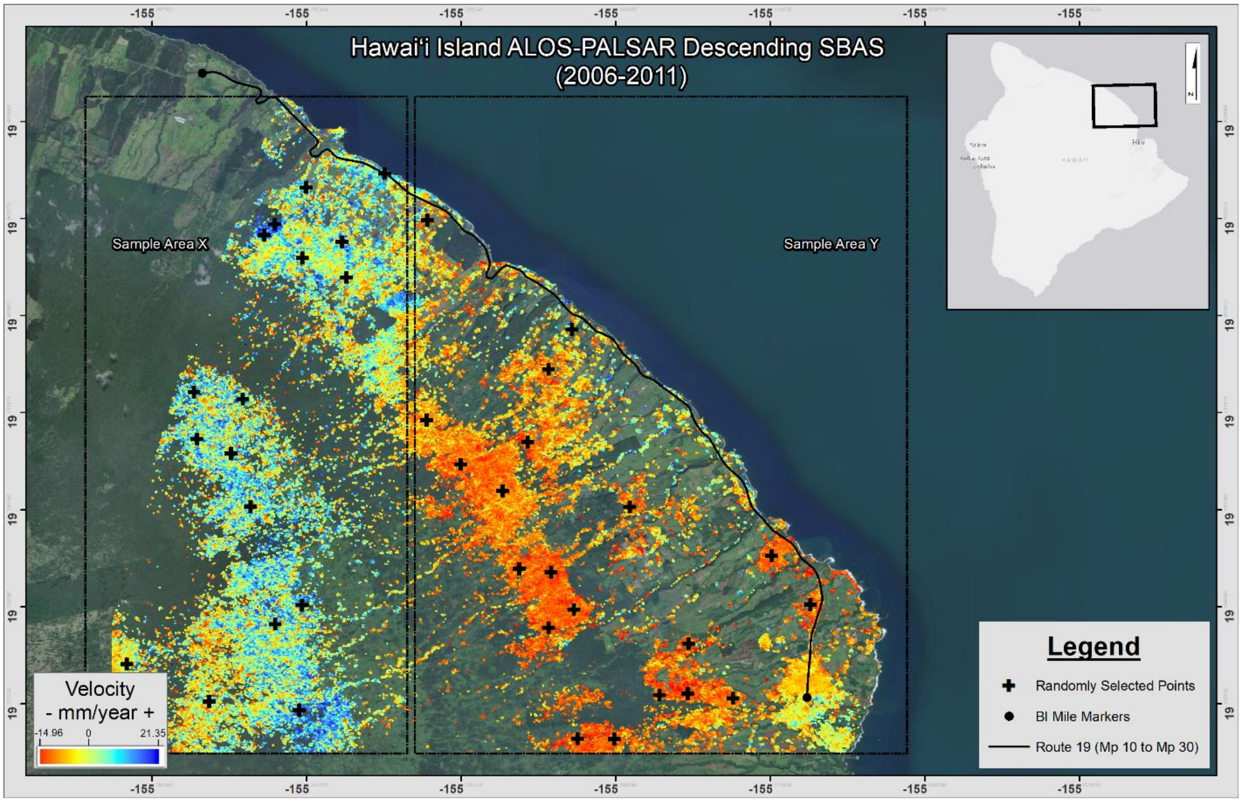

Figure 83 Sample areas X and Y with randomly selected points

The time-series displacement plots for select random points in Area X are shown in Figure 84. Although the magnitudes of each datapoint are different, they all follow the same pattern of increases and decreasing with time. Because these points are randomly located, it is difficult to understand how the temporal patterns for data in Area X can be so consistent. This suggests that the time-series displacement measurements are not reliable.

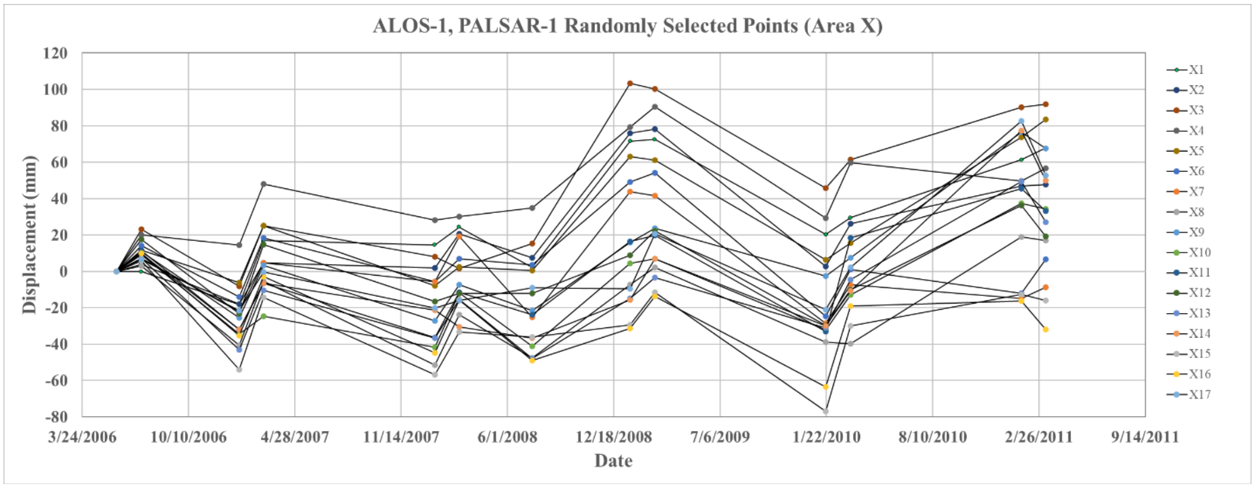

Figure 84 Plots of points selected in Area X

Time-series displacement plots for random points selected in Sample Area Y also show an obvious pattern as shown in Figure 85. There is a tighter grouping of the time-series displacement plots but the peaks are not so well defined. Nevertheless, the plots should not follow a consistent trend and should generally be more random.

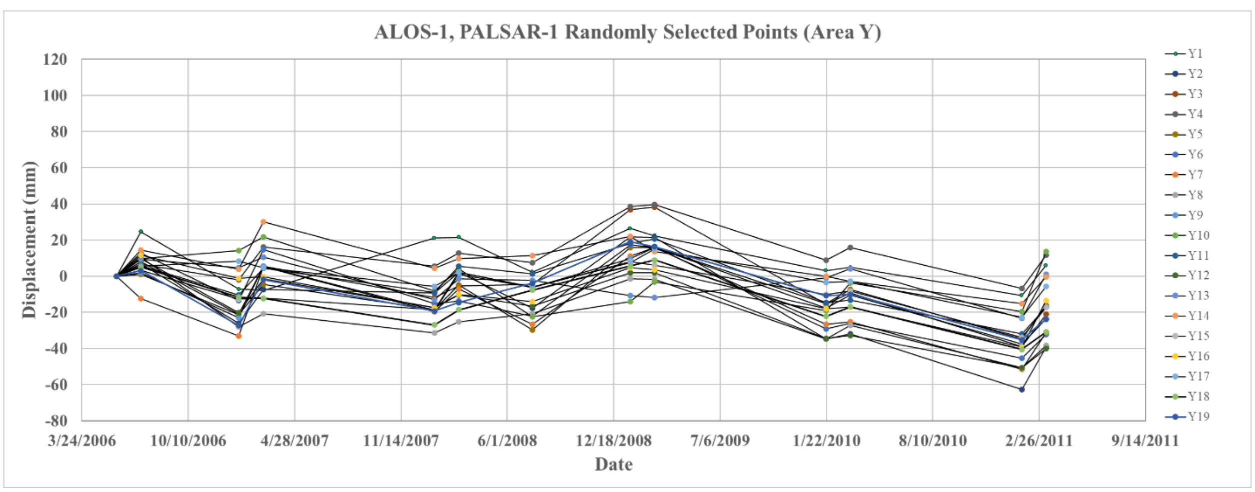

Figure 85 Plots of points selected in Area Y

Figure 86 superimposes the time-series displacement plots of the SBAS points in both areas X and Y. Plots for points in Area X are shown in blue, while plots for points in Area Y are shown in red. Based on the grouping, it can be seen that the residual phase ramps have not only affected the trends of the plots but also the magnitude.

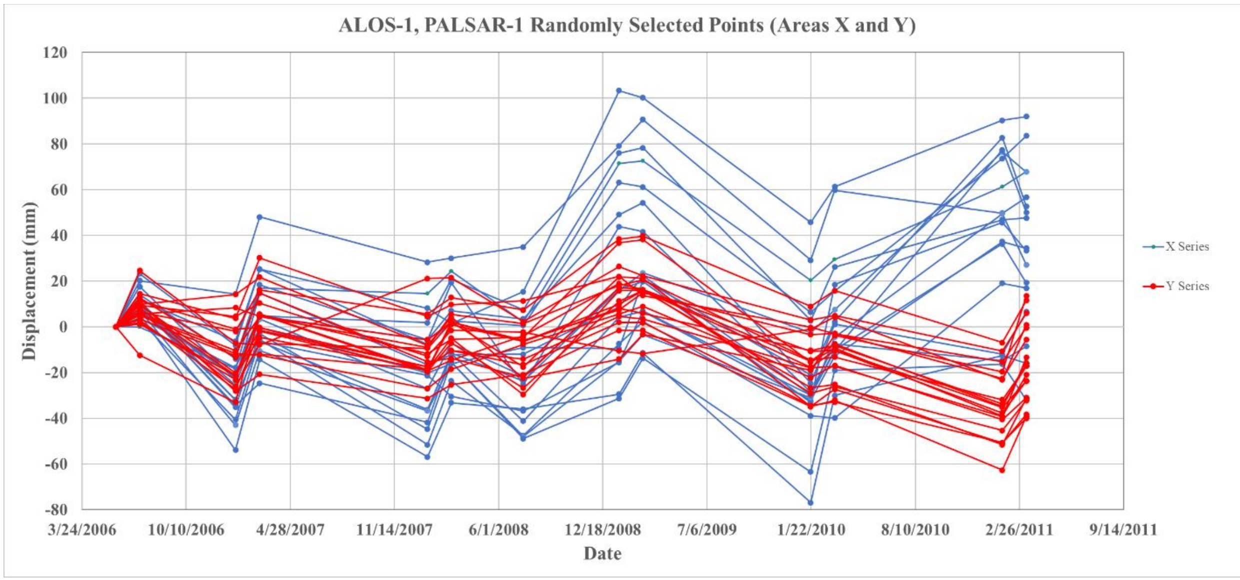

Figure 86 Comparison of X and Y series data plots

8.2. *Island of Maui*

Only descending datasets could be processed in SARscape for the available Sentinel-1 images. Attempts to process ascending datasets were unfruitful due to radar shadowing by Haleakalā. Radar shadowing prooved to be significant because Hana Highway lies on the northern flank of the Haleakalā volcano. Therefore, only line-of-sight displacements will be briefly presented for Maui.

8.2.1. Island of Maui SBAS Sentinel-1 Descending Results

Descending Sentinel-1 SBAS displacement measurements were obtained from November 11, 2015, to December 21, 2021, with a gap in the data from May 09, 2016, to November 01, 2018. Despite the large area as shown in Figure 87, SBAS returned only 13,032 points due to vegetation. The C-band (5.6 cm) wavelengths are easily scattered by vegetation. It is not anticipated that the topography is of significant concern for the descending dataset. Having less signal return results in low coherence. If the coherence for a point falls below the threshold of 0.1, that datapoint will be deleted by the SBAS algorithm.

The color symbology for velocity measurements have extreme negative and positive velocities of -42.86 mm/year and +36.65 mm/year. Route 360 is shown in black in Figure 87 with labels provided for mileposts 0 and 35.

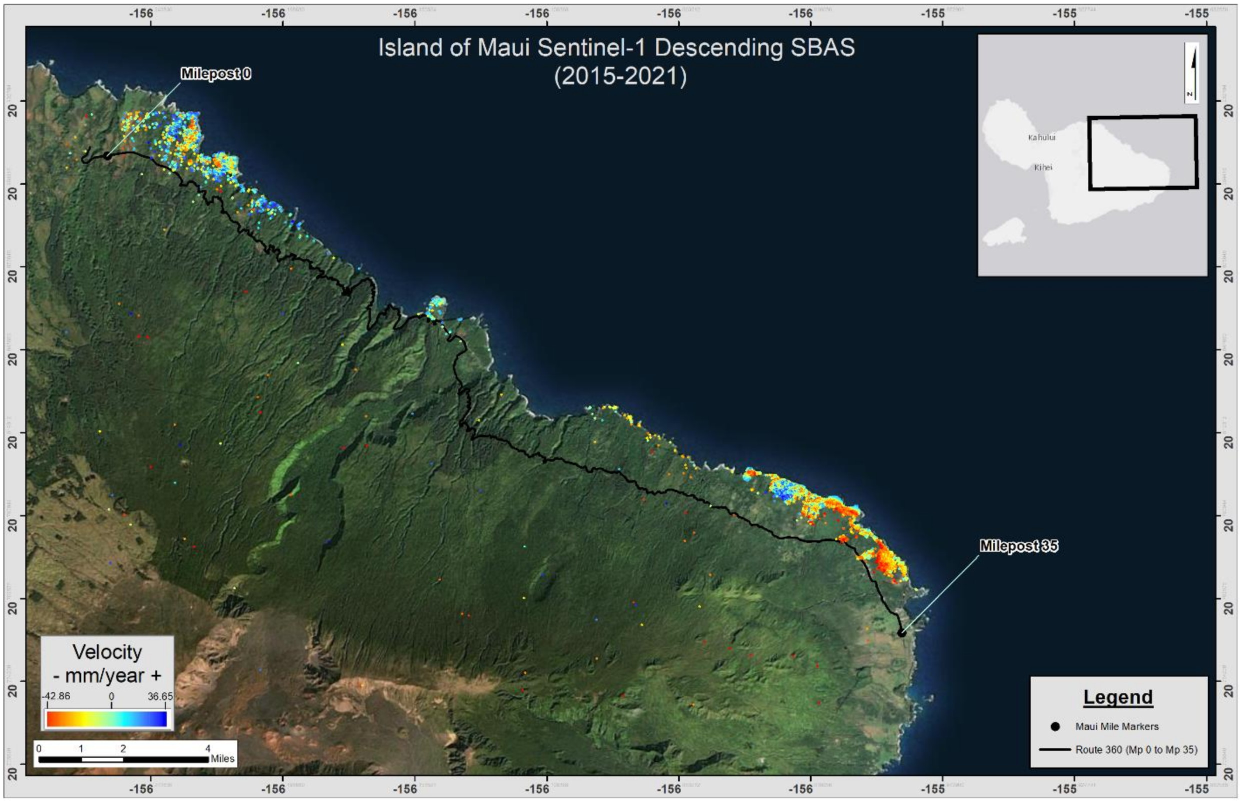

Figure 87 Island of Maui Sentinel-1 descending SBAS results

5 points along Route 360 with significant line-of-sight displacements were selected for review. The location of these points are shown in the labels in Figure 88 below.

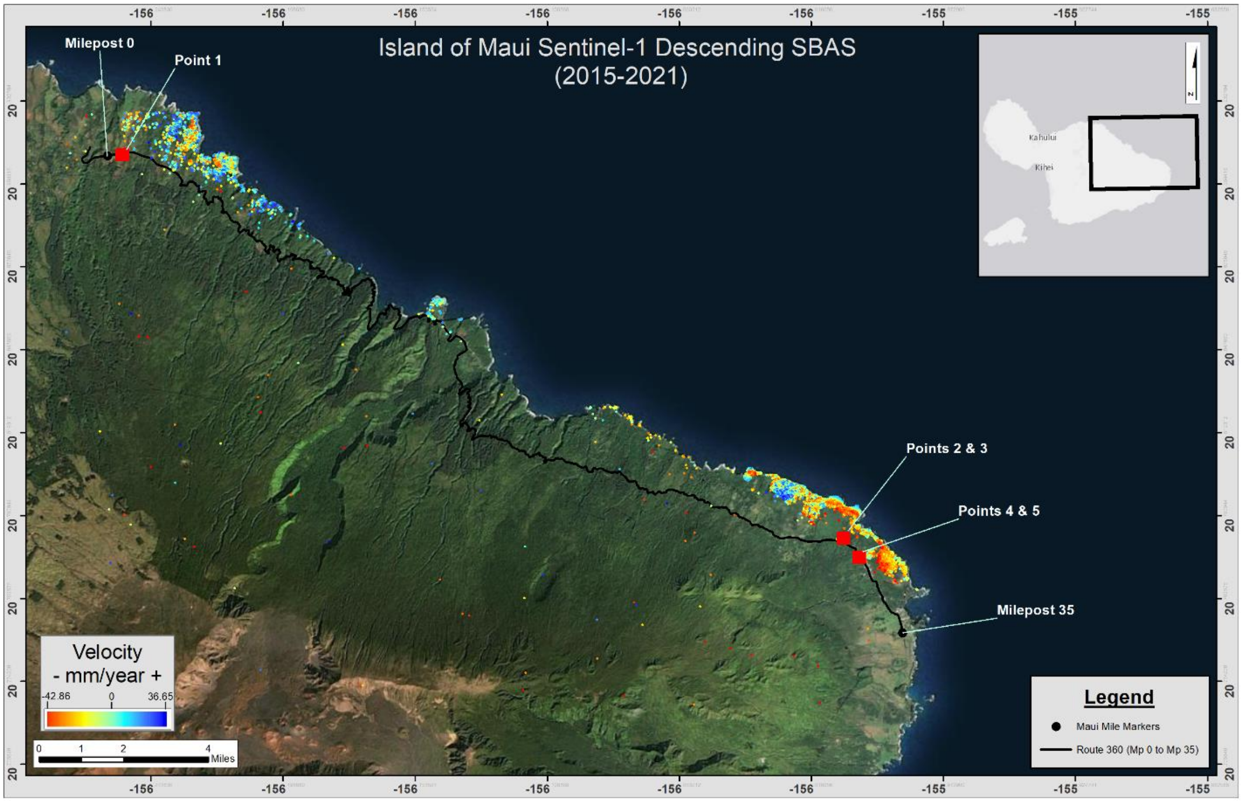

Figure 88 Island of Maui SBAS results with selected locations

Maui Point 1

Point 1 is approximately 1,700 feet or 0.33 miles east of Milepost 0. GPS coordinates for Point 1 are at latitude 21.91403, longitude -156.25353. The location is amplified in Figure 89.

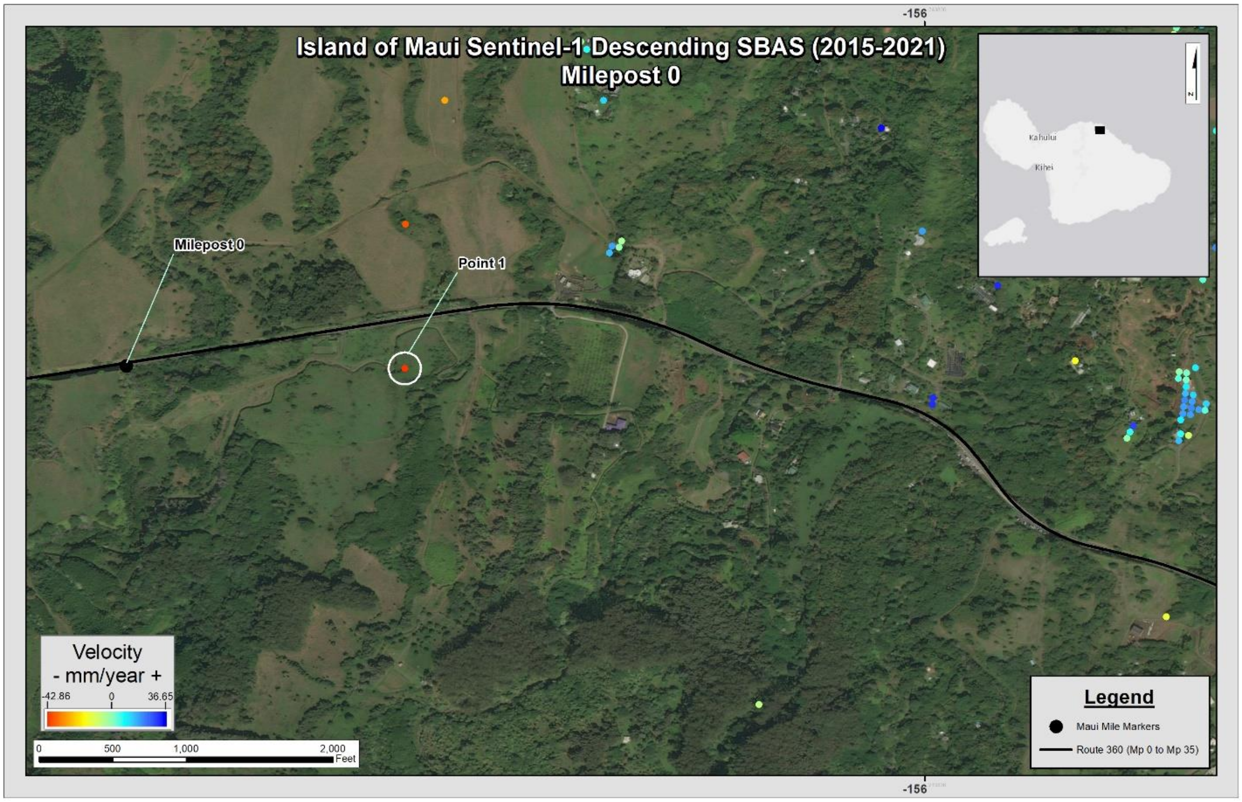

Figure 89 Location of interest for Maui's Point 1

Point 1 is approximately 330 feet south of the highway. Based on aerial imagery and the United States Geological Surveys 2017 *Topographic Map of the Nāhiku Quadrangle* (USGS 2017), the point is along the bank of the Koʻolau Ditch. The topography of the area is generally flat with mapped elevations of approximately 600 feet. This point is so far removed from the highway that it will unlikely affect the conditions of Route 360. Figure 90 blows up further the reference point in relation to Route 360.

Figure 90 Location of interest for Maui Point 1

Figure 91 provides line-of-sight measurements from November 11, 2015, to December 21, 2021. The calculated average velocity of Maui Point 1 is -18.20 mm/year and the coherence is 0.103. The vertical and horizontal precision of displacement measurements are 6.64 mm and and 5.16 mm, respectively. The parameters indicate that the result is somewhat reliable although the calculated coherence is near the coherence threshold.

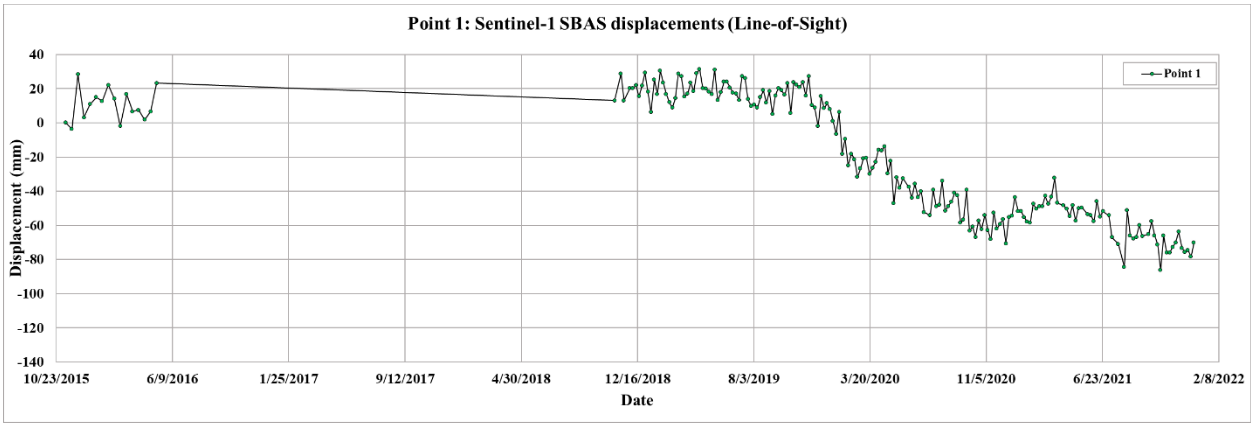

Figure 91 Time-series displacement plot for Maui Point 1

Maui Points 2 and 3

Points 2 and 3 lie approximately 750 feet or 0.14 miles East of Milepost 32 as shown in Figure 92. GPS coordinates for points 2 and 3 are latitude 20.78188, longitude -156.0075 and latitude 20.78183, longitude -156.00719, respectively.

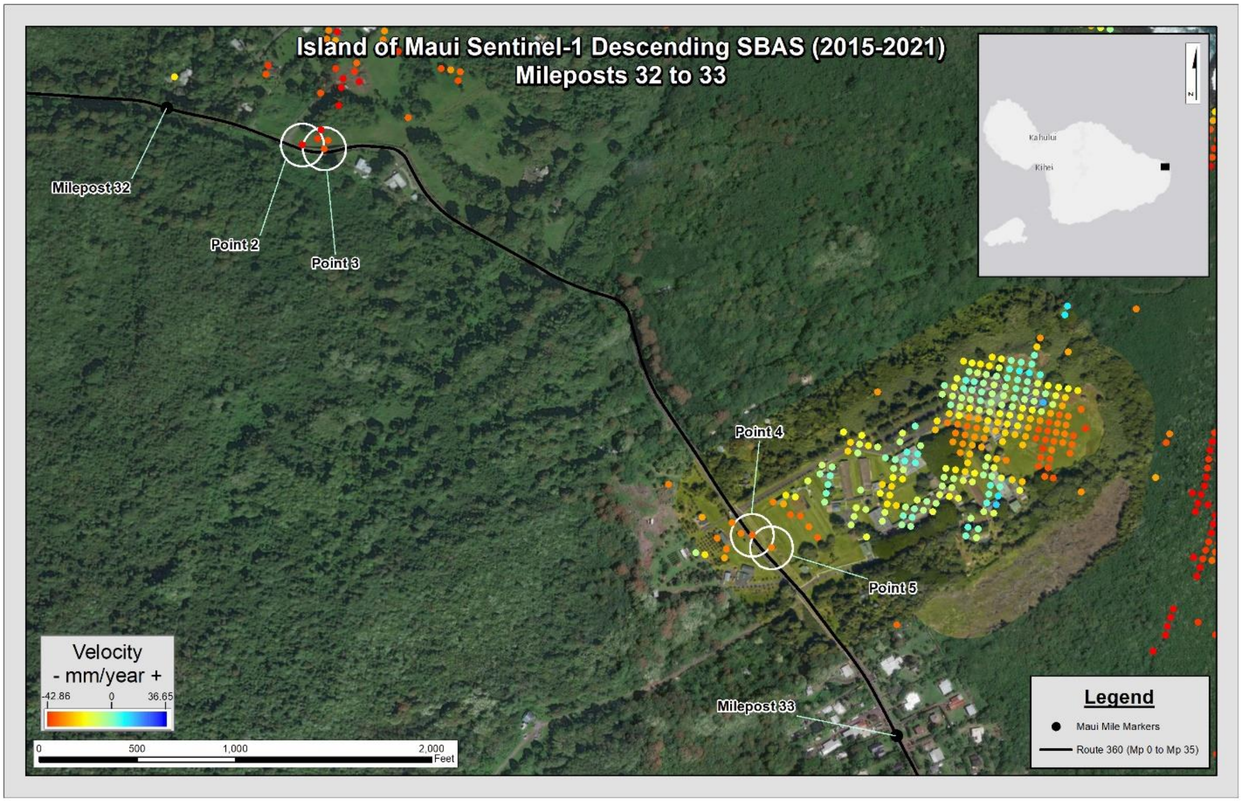

Figure 92 Location of interest for Maui Points 2 through 5

Google Earth Street View imagery indicate that the area of SBAS measurements is along a rock wall parallel to the highway (Google Earth 2019). The wall appears to be 4 feet to 6 feet tall and consists of uncemented rock placed along a near vertical cut along the highway along the easement of a private residence. Figure 93 blows up further the locations of Point 2 and Point 3.

Figure 93 Location of interest for Maui Points 2 and 3

Figures 94 and 95 provide line-of-sight measurements for Maui points 2 and 3, respectively from November 11, 2015, to December 21, 2021, with a gap in the data between May 9, 2016, and November 1, 2018. The calculated average velocity of Maui Point 2 is -17.42 mm/year and the coherence is 0.106. The vertical and horizontal precision of displacement measurements are 6.58 mm and 5.10 mm, respectively.

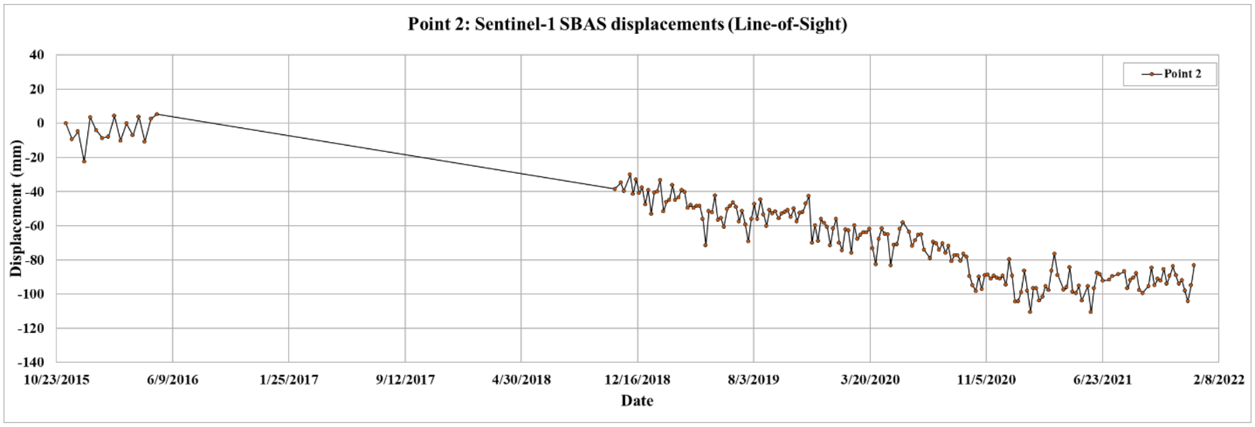

Figure 94 Time-series displacement plot for Maui Point 2

The calculated average velocity of Maui Point 3 is -24.97 mm/year and the coherence is 0.106. The vertical and horizontal precision of displacement measurements are 6.58 mm and 5.06 mm, respectively.

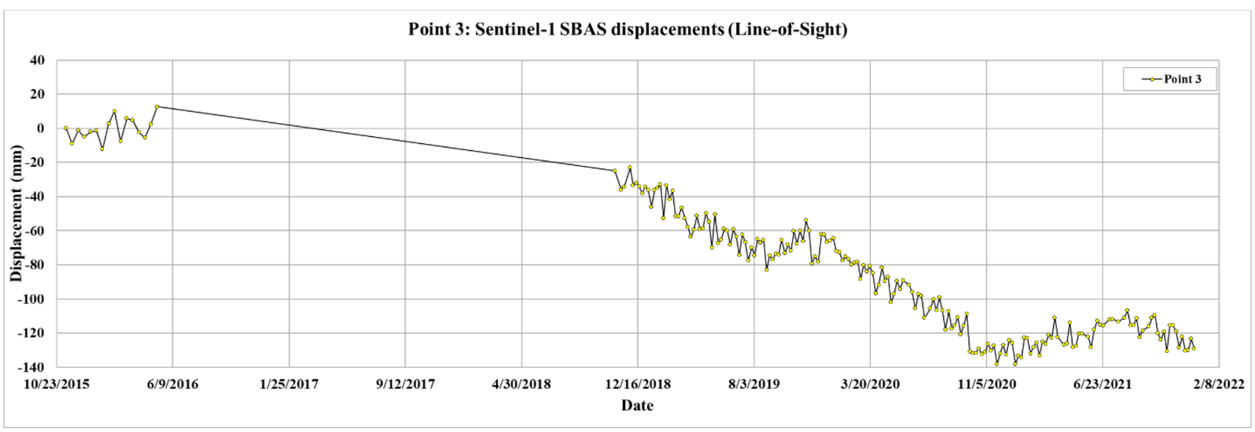

Figure 95 Time-series displacement plot for Maui Point 3

Maui Points 4 and 5

Points 4 and 5 are approximately 1,100 feet or 0.22 miles to the Northwest of Milepost 33 as shown in Figure 96. GPS coordinates for points 4 and 5 are latitude 20.77642, longitude -156.00121 and latitude 20.77624, longitude -156.00094, respectively.

Google Earth Street View imagery indicate that the points are within a drainage swale at the edge of the Hana High & Elementary School baseball field (Google Earth 2019).

Figure 96 Location of interest for Maui Points 4 and 5

Figure 97 provides line-of-sight measurements for Maui Point 4 from November 11, 2015, to December 21, 2021, with a gap in the data between May 9, 2016, and November 1, 2018. The calculated average velocity is -13.37 mm/year and the coherence is 0.103. The vertical and horizontal precision of displacement measurements are 3.61 mm and 2.50 mm, respectively.

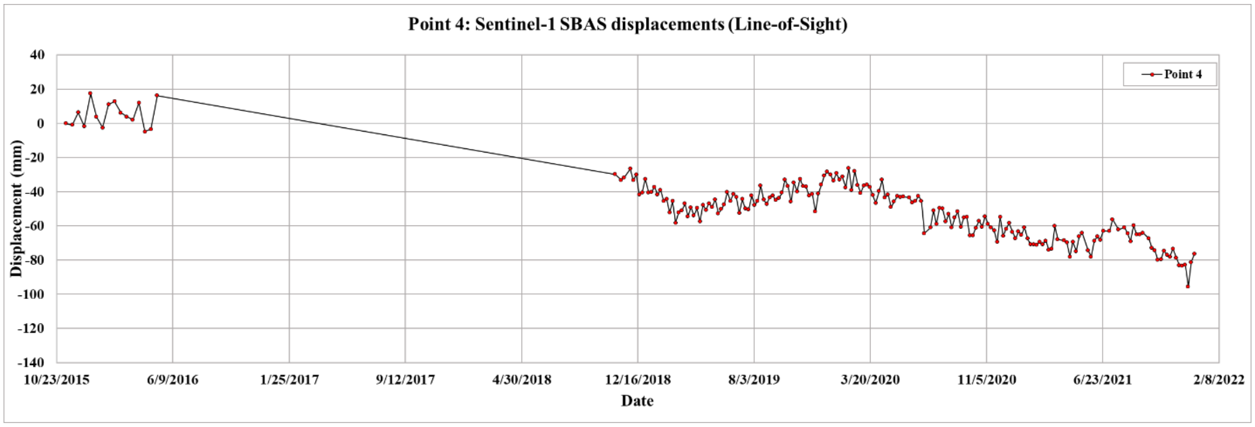

Figure 97 Time-series displacement plot for Maui Point 4

Figure 98 provides the line-of-sight measurements from November 11, 2015, to December 21, 2021, with a gap in the data between May 9, 2016, and November 1, 2018. The calculated average velocity is -12.68 mm/year and the coherence is 0.104. The vertical and horizontal precision of displacement measurements are 3.72 mm and 2.58 mm, respectively.

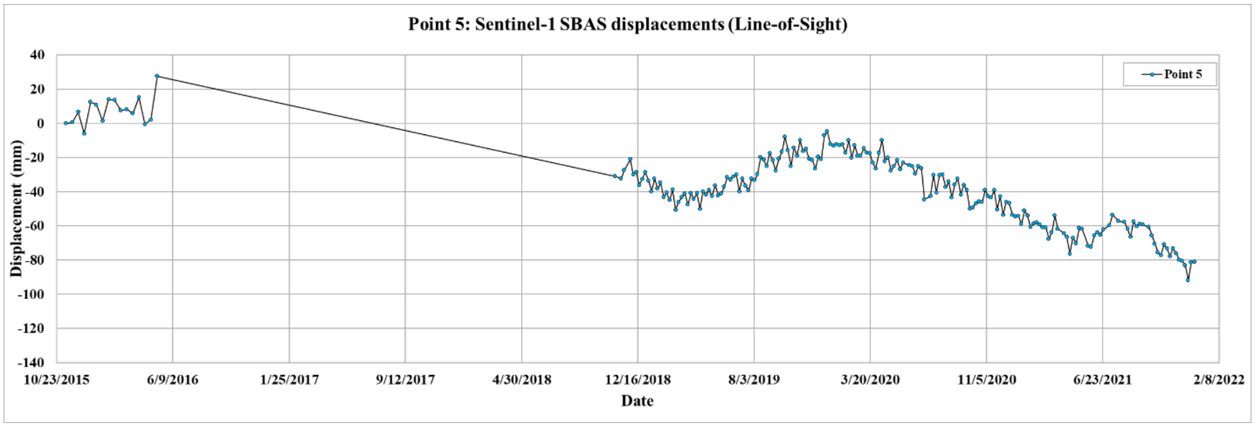

Figure 98 Time-series displacement plot for Maui Point 5

9. DISCUSSION

9.1. *O‘ahu Case Study*

The O‘ahu SBAS case study was conducted as a proof of concept for its use in the Hawaiian Islands due to the availability of inclinometer data for the Wai‘ōma‘o Landslide site for comparison. Ascending and descending Sentinel-1 datasets were processed for the south shore of O‘ahu. Attempts to acquire and process SAR imagery other than Sentinel-1 were not successful.

2D decomposition of the combined descending and ascending datasets is necessary to obtain the vertical and horizontal components of displacements. The horizontal displacement component (dEast) was then adjusted to match the direction of movement recorded by inclinometers to compare displacement trends. Seventeen (17) inclinometers were used in the comparison. Plots of inclinometer readings with SBAS results were made to determine if trends of inclinometers were consistent with SBAS results.

Of the seventeen plots, twelve (12) have SBAS trends that are generally consistent with the trends of inclinometer measurements. The plots with good or reasonably good agreement are shown below in Table 12.

Table 12 Inclinometer and SBAS measurements with agreeable trends

Inclinometer	SBAS Point	Inclinometer Displacement Rate (mm/year)
I-20	1	14.22
I-5 and I-5R (SAA)	2	15.49
I-24	3	23.88
I-33	8	24.05
I-33 and I-41 (SAA)	9	27.45
I-40	11	18.29
I-31	12	7.72
I-30	13	8.20
I-29 (SAA)	14	7.85
I-42 (SAA)	15	18.54
I-39	16	12.19
I-7	17	1.76

The plots with good agreement all consist of datasets with relatively gradual displacement velocities over time (approximately 25 mm per year).

Five (5) plots have trends that are inconsistent between SBAS and inclinometer readings as shown in Table 13.

Table 13 Inclinometer and SBAS trends that do not agree

Inclinometer	SBAS Point	Inclinometer Displacement Rate (mm/year)
I-36 and I36R (SAA)	4	66.04
I-38 (SAA) and I-38R (SAA)	5	520.70
I-37 (SAA) and I-37R (SAA)	6	269.88
I-35 (SAA), I-35R (SAA), I-35RR (SAA), I-35RRR (SAA)	7	866.78
I-34	10	7.32

Three plots (I-35, I-37 and I-38) showing entirely different trends were all in areas experiencing rapid movement velocities (between 56.64 to 236.68 mm per year).

Three (3) plots with relatively low displacement rates that were well captured by SBAS are shown in Table 14.

Table 14 SBAS measurements with low velocities

Inclinometer	SBAS Point	Inclinometer Displacement Rate (mm/year)	Maximum SBAS displacement (mm)	Horizontal Precision (mm)
I-31	12	7.72	34.00	2.90
I-30	13	8.20	36.00	2.93
I-29 (SAA)	14	7.85	25.00	2.95

For these three, the precision values are fairly close to the line-of-sight measurements.

The O‘ahu case study generally shows that SBAS analysis conducted with medium resolution Sentinel-1 datasets can be used to estimate ground movements. The results show that it is important to resolve line-of-sight displacement measurements to capture ground surface displacements. Also, it works well for areas experiencing relatively gradual displacements over time with rates not exceeding 25 mm per year.

Displacements between 56.64 mm per year and 236.68 mm per year were not well captured by SBAS. Therefore, use of Sentinel-1 and SBAS for landslide detection is likely only possible for slow moving events.

9.2. *Hawai‘i Island Sentinel-1 SBAS*

Both ascending and descending Sentinel-1 datasets were generated for Hawai‘i Island. The point density of the descending dataset was significantly greater than that of the ascending dataset. The descending dataset contained coverage for most of the areas between mileposts 10 and 30 on Route 19. The ascending dataset only provided coverage in the eastern portion of Route 19 due to the shadow effect whereby Mauna Kea blocked the radar signal from reaching the area. Due to the low point density of the ascending dataset, detailed analysis could only be conducted for the eastern portion of the study area.

The SBAS analysis in Area F (Honomū) using descending and ascending datasets revealed that 2D decomposition displacements are less than line-of-sight measurements. The results indicate that line-of-sight measurements alone may cause unnecessary alarm.

The SBAS results of Area G (Honomū) provide additional evidence that adjusted decomposed displacements can be less than the line-of-sight measurements. The results indicate that use of line-of-sight measurements alone should be avoided and to always use decomposed displacements in SBAS analysis.

9.3. *Hawaiʻi Island ALOS-1 PALSAR-1 SBAS*

The Hawaiʻi Island ALOS-1 PALSAR-1 SBAS dataset only included 13 images between 2006 and 2011. However, the SBAS results contained residual phase ramps. Results of randomly selected points demonstrated that there were consistent patterns in each grouping. These results are indicative of the effects of residual phase ramps. Efforts to use the available ALOS-1 PALSAR-1 data was conducted because the data is the only L-band series available. Given that L-band wavelengths have greater penetration through vegetated areas, use of the data would have been favorable but because of the presence of residual phase ramps, the dataset could not be used for analysis.

9.4. *Island of Maui Sentinel-1 SBAS*

SBAS analysis for the areas along Route 360 was unsuccessful because only descending data could be obtained. Due to vegetation, the descending heading yielded very low SBAS point density. The C-band (5.6 cm) Sentinel-1 wavelengths were likely scattered by the heavily vegetated areas. The influence of vegetation resulted in low coherence in SBAS processing. SBAS points with low coherence were removed by the SBAS algorithm resulting in low point density.

10. SUMMARY, CONCLUSIONS AND SUGGESTIONS FOR FUTURE WORK

The research objective was to use SAR imagery to conduct interferometry for two locations: Hawaii Route 19 between mileposts 10 and 30; and Hawaii Route 360 between mileposts 0 and 35. These locations are heavily vegetated and have significant topographic variation which present challenges for the application of InSAR. Most notably, vegetation limits the type of SAR data that can be used. X-band radar is incapable of penetrating vegetation. C-band radar allows limited penetration but can experience signal loss due. L-band data allows for greatest penetration; however, L-band datasets for the Hawaiian Islands are extremely limited.

Efforts were made to conduct interferometry with as many datasets as possible. Due to significant costs associated with some commercial datasets, complications associated with radar wavelength size and vegetation, and limited availability of some public datasets, interferometry analyses were limited to the use of Sentinel-1 and ALOS-1 PALSAR-1 datasets. Of the two, only Sentinel-1 analysis proved successful in providing measurements precise enough for change detection in the study locations.

Of the methods of analysis for remote sensing interferometry, the method most applicable to achieve the project goals was determined to be SBAS. The SBAS method is currently the industry standard for conducting remote sensing analysis in natural terrain for ground surface change detection. The SBAS method requires, at a minimum, 20 to 30 SAR images for successful processing. Datasets that contain more than 100 images acquired from a consistent frame and path allow for results that are precise enough to detect ground surface changes. The only publicly available SAR dataset with enough images for precise SBAS processing is from Sentinel-1.

The Oʻahu case study provided proof of concept for SBAS investigative efforts for the Hawaiʻi Island and Island of Maui study areas. The descending and ascending Sentinel-1 dataset captured measurable ground surface movements for a slope in Pālolo Valley. Seventeen inclinometer readings from publicly available monitoring reports were used to compare with SBAS results. 2-dimensional decomposition was performed for SBAS points in proximity to inclinometers. Of the 17, 12 of the SBAS analysis successfully captured movement in the area. Movements that are best captured by SBAS are relatively gradual with average velocities of less than 25 mm per year. Relatively rapid movements were not accurately captured by the SBAS method. Additionally, the case study demonstrated that d_{East} displacements could be adjusted to estimate displacements for movements in a different direction. After adjusting the SBAS measurements, the trends for many of the comparisons aligned well.

SBAS analysis of two SAR datasets was processed using the SARscape SBAS algorithm for the study area on Hawai‘i Island:

- Ascending and descending Sentinel-1 data;
- Descending ALOS-1 PALSAR-1 data.

With the Sentinel-1 data, only the descending dataset captured SBAS points throughout the project corridor. Ascending SBAS analysis resulted in significantly less points in the area.

ALOS-1 PALSAR-1 analysis yielded SBAS points throughout the project corridor; however, residual phase ramps were detected in the dataset. Due to the limitations of ALOS-1 PALSAR-1 analysis results, only the Sentinel-1 dataset was used to locate areas of ground surface change in the Hawai‘i Island study area.

For areas where there was overlap of descending and ascending SBAS points, 2D decomposition was performed. The d_v, d_{East}, and adjusted displacements were reviewed to determine the likely magnitude of displacements for Areas F and G. The d_v, d_{East}, and adjusted curves indicate that displacements in the areas are likely less than displacements indicated by line-of-sight measurements. This demonstrates that use of SBAS results with only line-of-sight measurements from one satellite heading should be avoided.

Only descending data could be obtained from Sentinel-1 SBAS analysis for the Maui study location. Attempts to conduct analysis with ascending Sentinel-1 data and ALOS-1 PALSAR-1 data were not successful because of shadow effects caused by the Haleakalā shield volcano, and because of insufficient ALOS images, respectively.

The Sentinel-1 descending SBAS results yielded few points due to the area being heavily vegetated.

The results presented in this report are representative of the current capability to conduct SBAS interferometry at the locations requested for analysis by HDOT. The upcoming NISAR mission will allow public access of medium resolution L-band data that will be collected every 6 days. The NISAR datasets will have greater penetration through vegetation and signal return and should allow for higher point density in the study areas. It is recommended that further InSAR analysis be conducted at the Hawaiʻi Island and Maui study areas after NISAR datasets become available. At the time of writing for this report, NASA had chosen the Alaska Satellite Facility DAAC to host the NISAR mission data (JPL 2022).

REFERENCES

Ayman Abdel-Hamid, Olena Dubovyk, Klaus Greve,The potential of sentinel-1 InSAR coherence for grasslands monitoring in Eastern Cape, South Africa, International Journal of Applied Earth Observation and Geoinformation, Volume 98,2021, 102306, ISSN 1569-8432,https://doi.org/10.1016/j.jag.2021.102306.

ASF DAAC 2021, contains modified Copernicus Sentinel data 2015, processed by ESA.

Berardino, P.; Fornaro, G.; Lanari, R.; Sansosti, E. A new algorithm for surface deformation monitoring based on small baseline differential SAR interferograms. IEEE Trans. Geosci. Remote Sens. 2002, 40, 2375–2383.

C&C of Honolulu (2021), Oahu Elevation Contours 40ft, based on the USGS 1:24,000 Digital Elevation Models (DEM), Office of Planning and Sustainable Development, State of Hawaii, Geospatial Data Portal, Accessed online on 12/10/2021, URL: https://geoportal.hawaii.gov/datasets/HiStateGIS::oahu-elevation-contours-40ft/explore?location=21.483419%2C-157.963650%2C11.00

C&C of Honolulu (2021), Hawaii Elevation Contours 100ft, based on the USGS 1:24,000 Digital Elevation Models (DEM), Office of Planning and Sustainable Development, State of Hawaii, Geospatial Data Portal, Accessed online on 12/10/2021, URL: https://geoportal.hawaii.gov/datasets/HiStateGIS::hawaii-elevation-contours-100ft/explore?location=19.586444%2C-155.424500%2C11.00

C&C of Honolulu (2021), Maui Elevation Contours 100ft, based on the USGS 1:24,000 Digital Elevation Models (DEM), Office of Planning and Sustainable Development, State of Hawaii, Geospatial Data Portal, Accessed online on 12/10/2021, URL: https://geoportal.hawaii.gov/datasets/HiStateGIS::maui-elevation-contours-100ft-1/explore?location=20.802084%2C-156.334250%2C11.00

C&C of Honolulu (2021), Geological Units for the State of Hawaii. Source: USGS 2007. Office of Planning and Sustainable Development, State of Hawaii, Geospatial Data Portal, Accessed online on 12/10/2021, URL: https://geoportal.hawaii.gov/datasets/HiStateGIS::geological-units/explore?location=21.512960%2C-157.697648%2C10.78

C&C of Honolulu 2022. Kuahea Street Area Stabilization Project, Department of Design and Construction, accessed on 7/2/2022, URL: https://www.honolulu.gov/cms-ddc-menu/site-ddc-sitearticles/38609-kuahea-street-area-repairs.html

Cigna, F.; Tapete, D. Sentinel-1 Big Data Processing with P-SBAS InSAR in the Geohazards Exploitation Platform: An Experiment on Coastal Land Subsidence and Landslides in Italy. Remote Sens. 2021, 13, 885. https://doi.org/10.3390/rs13050885

Copernicus Sentinel data for the Island of Oahu (descending) [2014-2021]. Retrieved from ASF DAAC on March 18, 2022, processed by ESA

Copernicus Sentinel data for the Island of Oahu (Ascending) [2014-2021]. Retrieved from ASF DAAC on March 13, 2022, processed by ESA

Copernicus Sentinel data for the Island of Hawaii (descending) [2014-2021]. Retrieved from ASF DAAC on April 03, 2022, processed by ESA

Copernicus Sentinel data for the Island of Hawaii (Ascending) [2014-2021]. Retrieved from ASF DAAC on April 03, 2022, processed by ESA

Copernicus Sentinel data for the Island of Maui (descending) [2014-2021]. Retrieved from ASF DAAC on March 27, 2022, processed by ESA

Copernicus Sentinel data for the Island of Maui (Ascending) [2018-2021]. Retrieved from ASF DAAC on April 5, 2022, processed by ESA

Copernicus Sentinel-1 orbital files [2014-2021]. Retrieved from Copernicus Open Access Hub on February 20, 2022

Dataset: © JAXA/METI ALOS PALSAR Hawaii Island (Descending)L1.0 [2006-2011]. Accessed through ASF DAAC 11 March 29, 2022

Department of Transportation (2019), Pali Highway Open 24/7 in Both Directions Beginning Dec. 21, 2019, Department of Transportation Highways. Retrieved from web on October 6, 2020 URL:http://hidot.hawaii.gov/highways/pali-highway-open-24-7-in-both-directions-beginning-dec-21-2019/

Ellen, S.D., Liu, L.A.S.M., Fleming, R.W., Reid, M.E., and Johnsson, M.J., Relation of slow-moving landslides to earth materials and other factors in valleys of the Honolulu District of Oahu, Hawaii: U.S. Geological Survey Open-File Report 95-218, Online at https://pubs.er.usgs.gov/publication/ofr95218.

Esri. "Topographic" [basemap]. Scale Not Given. "World Topographic Map". 2014. http://www.arcgis.com/home/item.html?id=30e5fe3149c34df1ba922e6f5bbf808f. (December 20, 2021).

Feng Q, Xu H, Wu Z, You Y, Liu W, Ge S. Improved Goldstein Interferogram Filter Based on Local Fringe Frequency Estimation. Sensors (Basel). 2016 Nov 23;16(11):1976. doi: 10.3390/s16111976. PMID: 27886081; PMCID: PMC5134634.

Fuhrmann, T.; Garthwaite, M.C. Resolving Three-Dimensional Surface Motion with InSAR: Constraints from Multi-Geometry Data Fusion. *Remote Sens.* **2019**, *11*, 241. https://doi.org/10.3390/rs11030241

Geolabs. 2021. Monitoring Progress Report No. 33, Phase III - Additional Instrumentation Monitoring, Kuahea Street Area Movement; CIP Project No. 97504, Contract No. 60578, Amendment No. 18; Palolo, Oahu, Hawaii. Prepared for City & County of Honolulu Department of Design & Construction. Obtained from the City & County of Honolulu Municipal Reference Center.

Giambelluca, T.W., Q. Chen, A.G. Frazier, J.P. Price, Y.-L. Chen, P.-S. Chu, J.K. Eischeid, and D.M. Delparte, 2013: Online Rainfall Atlas of Hawai‘i. *Bull. Amer. Meteor. Soc.* 94, 313-316, doi: 10.1175/BAMS-D-11-00228.1

Google Earth Pro, Version 7.3.4.8573 (2018), *Latitude 21°18'5.48"N, Longitude -157°47'13.92"W*, [desktop software], accessed on 05/29/2022

Google Earth Pro, Version 7.3.4.8573 (2013), *Latitude 21°18'5.48"N, Longitude -157°47'13.92"W*, [desktop software], accessed on 05/29/2022

Google Earth Pro, Version 7.3.4.8573 (2004), *Latitude 21°18'5.48"N, Longitude -157°47'13.92"W*, [desktop software], accessed on 05/29/2022

Google Earth Street View (2019), Version 7.3.4.8573, *Latitude 20°46'54.63"N, Longitude -156°00'26.33"W*, [online], accessed on 07/03/2022 URL: https://www.google.com/maps/@20.781876,-156.0077222,3a,75y,91.99h,84.36t/data=!3m6!1e1!3m4!1sjuCAJanGndizwHmVJlsAgA!2e0!7i16384!8i8192

Google Earth Street View (2019), Version 7.3.4.8573, *Latitude 20°46'35.23"N, Longitude -156°00'04.36"W*, [online], accessed on 07/03/2022 URL: https://www.google.com/maps/@20.7765007,-156.0012847,3a,75y,94.24h,85.48t/data=!3m10!1e1!3m8!1s4aT2vZDN2OW3Cp5PDaJlAg!2e0!6shttps:%2F%2Fstreetviewpixels-pa.googleapis.com%2Fv1%2Fthumbnail%3Fpanoid%3D4aT2vZDN2OW3Cp5PDaJlAg%26cb_client%3Dmaps_sv.tactile.gps%26w%3D203%26h%3D100%26yaw%3D61.917023%26pitch%3D0%26thumbfov%3D100!7i16384!8i8192!9m2!1b1!2i39

Jet Propulsion Laboratory 2022, NISAR NASA-ISRO SAR MISSION, Mission Concept, California Institute of Technology, accessed online on 07/09/2022. URL: https://nisar.jpl.nasa.gov/mission/mission-concept/

Manzo, M.; Ricciardi, G.P.; Casu, F.; Ventura, G.; Zeni, G.; Borgström, S.; Berardino, P.; Del Gaudio, C.; Lanari, R. Surface deformation analysis in the Ischia Island (Italy) based on spaceborne radar interferometry. J. Volcanol. Geotherm. Res. 2006, 151, 399–416, doi:10.1016/j.jvolgeores.2005.09.010.

Massonnet and Feigl 1998, Massonnet, D. and Feigl, K. L. Radar interferometry and its application to changes in the earth’s surface. Review of geophysics, 36(4):441-500.

Meyer, Franz. “Spaceborne Synthetic Aperture Radar – Principles, Data Access, and Basic Processing Techniques.” SAR Handbook: Comprehensive Methodologies for Forest Monitoring and Biomass Estimation. Eds. Flores, A., Herndon, K., Thapa, R., Cherrington, E. NASA. 2019. DOI: 10.25966/ez4f-mg98

Meyer, F. AlaskaX: *SAR-401 - Synthetic Aperture Radar: Hazards* [MOOC]. EdX. https://www.edx.org/course/sar-hazards

Meyer, F.(2021) AlaskaX: The Concept of Short Baseline Subset (SBAS) InSAR [MOOC Lecture]. Franz J Meyer, University of Alaska Fairbanks, *SAR-401 - Synthetic Aperture Radar: Hazards*. EdX. https://www.edx.org/course/sar-hazards

National Oceanic and Atmospheric Administration (NOAA) 2022, The Atmospheric Window, US Department of Commerce, National Weather Service. Retrieved from Web on 07/11/2022, URL: https://www.weather.gov/jetstream/absorb

Peck, R. 1959, December. Report on Causes and Remedial Measures, Waiomao Slide, Honolulu. 33p.

SARMAP 2021, SBAS Tutorial, Version 5.6. Retrieved through personal correspondence with Andrew Fiore of L3HARRIS GEOSPATIAL

Sherrod, D.R., Sinton, J.M., Watkins, S.E., and Brunt, K.M., 2021, Geologic map of the State of Hawai‘i: U.S. Geological Survey Scientific Investigations Map 3143, pamphlet 72 p., 5 sheets, scales 1:100,000 and 1:250,000, https://doi.org/10.3133/sim3143

Web Soils Survey 2019, Natural Resources Conservation Service, United States Department of Agriculture. Web Soil Survey. Accessed on 07/24/2022 . URL: http://websoilsurvey.sc.egov.usda.gov/.

Tong, X. and Schmidt, D. (2016). Active movement of the cascade landslide complex in Washington from a coherence-based InSAR time series method. Remote Sensing of Environment, 186:405–415.

UC Berkeley 2022. January 22-23 2021: Short Course on “New Technologies for Geotechnical Infrastructure Sensing and Monitoring” [MOOC]. Berkeley University of California, Geosystems Engineering. https://geotechnical.berkeley.edu/news/january-22-23-2021-short-course-new-technologies-geotechnical-infrastructure-sensing-and

United States Department of Agriculture Soil Conservation Service [in cooperation with The University of Hawaii Agricultural Experiment Station]. 1972. Soil Survey of Islands of Kauai, Oahu, Maui, Molokai, and Lanai, State of Hawaii. Washington, DC: U.S. Government Printing Office.

United States Geological Survey 2015. USGS 10-m Digital Elevation Model (DEM): Hawaii: Oahu Provided by Esri Honolulu.

United States Geological Survey 2018. USGS EROS Archive – Digital Elevation – Shuttle Radar Topography Mission (STRM) 1 Arc-Second Global, Provided Earth Resources Observation and Science (EROS) Center

United States Geological Survey 2017. *Topographic Map of the Honolulu Quadrangle* Hawaii – Honolulu County, 7.5-minute Series, scale 1:24,000, U.S. Department of the Interior, accessed on 5/28/2022, URL: https://ngmdb.usgs.gov/topoview/viewer/#15/21.3060/-157.7854

United States Geological Survey 2017. *Topographic Map of the Pāpaʻaloa Quadrangle*, Hawaii– Hawaii County, 7.5-minute Series, scale 1:24,000, U.S. Department of the Interior, accessed on 5/28/2022, URL: https://ngmdb.usgs.gov/ht-bin/tv_browse.pl?id=06a003d6f925d9ecd16d50d0501f62e8

United States Geological Survey 2017. *Topographic Map of the Nāhiku Quadrangle* – Maui County, 7.5-minute Series, scale 1:24,000, U.S. Department of the Interior, accessed on 5/28/2022, URL: https://ngmdb.usgs.gov/ht-bin/tv_browse.pl?id=d8d24008f3115bf85176e9653c1a98de